Frequency Tunable Light Source of Continous Quadrature Entanglement

Christian Schori

11-02-02

Contents

Preface

This thesis is presented for the Faculty of Science at the University of Aarhus as part of the requirements for the Ph.D.-degree in physics.

The work presented in this thesis has been carried out in the Quantum Optics Group of Prof. Eugene Polzik at the Institute of Physics and Astronomy, Aarhus University. When joining the group in February 1998 the author participated along with Jens Lykke Sørenen in the spin squeezing experiment which formed the core of Jan Hald's Ph.D.-work (paper 6,7 shown below). This experiment was an ideal, although very challenging, introduction to the field of quantum optics and experimental work in general. Many tricks and trades where passed on by Jan and Jens to whom the author is truly indebted. In parallel with the spin squeezing experiments the author together with Jens started building up an all fiber-optic quantum cryptography experiment. This work reached fruition at the end of 2000 thanks to a devoted effort by Peter Møller Nielsen to implement software control (paper 5). The cryptography experiment was funded by the "Thomas B. Thriges fond" over a 3 year period and involved close collaboration with Ivan Damgaard and Louis Salvail from the computer science department.

In 1999 the author started construction of a tunable source of quadrature squeezed and entangled light. This work was carried out in close collaboration with Jens Lykke Sørensen who boosted the project with his many years of practical experience as a "phase space squeezer". During the construction phase the author also enjoyed interacting with Olivier Arzicet (ENS, Paris) who joined the project for 6 months. The source, an optical parametric amplifier or OPA, was applied to demonstrate for the first time *frequency nondegenerate* continuous variable entanglement (paper 1). Further the source tunability was exploited to excite an electric dipole transition in atomic cesium contained in a room temperature glass cell. This opened the possibility to study in detail the noise properties of a continuous variable light-atom interface which is an important, although very preliminary, step towards future application in the field of quantum information (paper 2,3,4). The experimental techniques involved in preparing and reading out the cesium atomic spin state have been developed by Brian Julsgaard without whom this exciting experiment would not have been possible. It has been a pleasure discussing physics and real life with Brian and by the way...9192631770 cycles is a very large margin.

During the years in the Quantum Optics laboratory I have enjoyed discussions with its many inhabitants including the old generation : Lasse Leick, Jens Peter Christensen, Mikkel Andersen, Jacob Skovborg Andersen, Alexander Kozhekin, and the current generation : Anton Verchovski, Plamen Petrov, Jens Kristian Mikkelsen, Jacob Sherson, Daniel Kosec, and Wolfgang Tittel.

Finally I would like to thank my thesis adviser Eugene Polzik for his support, patience and many creative ideas.

Clearly the team-work described above justifies the use of terms like "..*we* have constructed..." or "..*we* have measured.." throughout the thesis. However, any errors or wrong interpretations found in the text are the sole responsibility of the author.

Christian Schori
September 2002.

Publications and presentations

The work presented in this thesis has resulted in the following publications :

1. C.Schori, J.L.Sorensen, and E.S.Polzik, *Narrow band frequency tunable source of continuous quadrature entanglement,* to appear in Phys. Rev. A (quant-ph/0205015). [3-6]
2. C. Schori, B. Julsgaard, J. L. Sørensen, and E. S. Polzik, *Recording Quantum Properties of Light in a Long-Lived Atomic Spin State: Towards Quantum Memory,* Phys. Rev. Lett. 89, 057903 (2002). [7]
3. J. L. Sørensen, B. Julsgaard, C. Schori, and E. S. Polzik, *Quantum limits encountered in atomc spin measurements*, submitted
4. E.S Polzik, B. Julsgaard, C. Schori, and J. L. Sørensen, *Quantum communication and memory with entangled atomic ensembles,* to appear in "Atomic Physics 2002", ICAP, ed. Pritchard *et al*, World Scientific
5. P.M. Nielsen, C. Schori, J.L. Sørensen, L. Salvail, I. Damgård, and E.S.Polzik, *Experimental quantum key distribution with proven security against realistic attacks,* J.Mod.Opt. 48 (13): 1921-1942 (2001) [8]

The numbers in square brackets refer to the chapters in this thesis which include the results presented in the publication. The author has also participated in experiments not presented in this thesis. This work has resulted in the publications

6. J. Hald, J. L. Sørensen, C. Schori, and E. S. Polzik, *Spin squeezed atoms: A macroscopic entangled ensemble created by light,* Phys. Rev. Lett. 83 (7): 1319-1322 (1999)
7. J. Hald, J. L. Sørensen, C. Schori, and E. S. Polzik, *Entanglement transfer from light to atoms,* J.Mod.Opt. 47 (14-15): 2599-2614 (2000)

The author has presented the work in this thesis at the following meetings

- *QELS 2002* (*Quantum Electronics and Laser Science conference*), Long beach, California (USA), May 2002
- *Euresco conference : Quantum information*, San Feliu de Guixols, Spain, March 2002
- *European Commision QIPC Workshop*, Torino, Italy, October 2001
- *QUICK Conference*, Cargese, Corsica (France), April 2001
- *International Workshop on the Physics of Quantum Information*, Helsinki, Finland, September 1998

Chapter 1

Introduction

The work presented in this thesis is an experimental investigation of quantum noise properties in two optical systems (Chapter 3-6,8) and in an atom-optical interface (Chapter 7).

To set the stage Chapter 2 introduces/reviews the phase space picture of two conjugate, i.e. noncommuting, observables with continuous spectra. The emphasis is on the quadrature observables (position and momentum) of the harmonic oscillator which are the *only* noise observables which we measure and report throughout Chapters 3-7. As with the measurement of any physical quantity we must express our noise measurement on some scale. The unit of this scale was "discovered" by E. Schrödinger in 1926[1] only half a year after giving birth to the wave function formulation of modern quantum theory. This paper demonstrates that a Poissonian superposition of oscillator eigenstates describes a wavepacket with constant spatial width. Today this state is known as a *coherent state* and the constant (scaled) width in both quadratures is the unit of noise (often referred to as the *standard quantum limit* or SQL) against which we compare all our experimental results. If Schrödinger had Fourier transformed his oscillator wavepacket he would probably have stumbled over the uncertainty principle discovered by W. Heisenberg half a year later[2]. Heisenberg limited his discussion to a free particle, but a few month later his ideas were extended to a particle in external fields by E. H. Kennard[3]. This work clearly states the possibility to *squeeze* the harmonic oscillator, i.e. prepare an initial position more precisely than the width of Schrödingers coherent wavepacket. Experimentalist had to await the laser to (i) manipulate optical modes (harmonic oscillators) at the SQL, and (ii) get high intensity to implement nonlinear optics which is essential for any deterministic squeezing scheme[1]. An excellent review of the initial theoretical proposals for preparing squeezed states of light can be found in Ref.[4], while a one page summary of the first experimental squeezing results is found in Ref.[5]. The first experimental squeezing trace (17 % below SQL) was reported with nondegenerate fourwave mixing using the $\chi^{(3)}$-nonlinearity from quasi-resonant interaction with an atomic sodium beam[6]. The best squeezing is however observed with spontanous parametric downconversion ($\chi^{(2)}$-nonlinearity) inside a resonant cavity structure called an optical parametric amplifier or OPA[7]. An elementary discussion of the physical principle behind squeezing inside the OPA is also included in Chapter 2.

Chapter 3 offers a formal derivation of the OPA squeezing spectrum while Chapter 4 describes the construction and test of a frequency tunable OPA. Chapter 5 extends the theory to the nondegenerate OPA or NOPA. This system allows to prepare an approximate EPR state ([8]) as originally proposed by M. Reid[9]. The experimental generation of this state and its characterization in terms of recent entanglement criteria ([10]) is the subject of Chapter 6.

In Chapter 7 we exploit the tunability of our OPA to engineer the quantum noise on a dispersive probe locked to the cesium D2 line. After propagation through a cloud of room temperature atomic

---

[1] Any classical distribution of oscillating charges and currents only produces 'classical' light, i.e. prepares the optical modes in coherent states corresponding to Schrödinger wavepackets.

cesium we measure the quadrature noise on the probe. Using the OPA to modulate the probe noise we isolate an additional "backaction" noise from the atomic sample. This contribution is accounted for by a simple nondemolition type interaction which acts as a "beamsplitter" mixing atomic and probe observables. The results in this chapter should be viewed as an investigation of this mixing which is only a preliminary step towards the goal of realizing an atom-light interface for continuous quantum variables[11].

Chapter 8 describes the construction and test of a fiber-optic quantum cryptography link. This work is complementary to the rest of the thesis since here we implement single photons with discrete observables and instead of reducing quantum projection noise (the essence of squeezing) we exploit it to distribute a secure key. It is interesting to note that while quantum noise reduction has not yet found commercial application, the very nature of quantum noise (as formulated in Heisenberg's uncertainty principle for conjugate observables) has led to construction of commercial products within a decade (quantum cryptography link, random number generator, single photon detector, and soon "photon guns"). But if quantum noise is the basic resource than one can surely extend the single photon key distribution to continuous variables. This extension is discussed and it is shown that continuous variable quantum cryptography may be a superior alternative for long distance key distribution. Finally, Chapter 9 contains a brief summary of the thesis.

In some respect the recent achievement of BEC in dilute alkali gases[12] parallels the advent of the laser and a new field of nonlinear *atom optics* is emerging[13]. For cold atoms the nonlinear atom-atom interaction provides free, tunable nonlinearity (via Feshbach resonances) and experiments have already demonstrated atomic four-wave mixing ([14],[15]) and atom number squeezing in optical lattices[16],[17]. The strong sub-Poissonian lattice occupation in the Mott insulator phase ([17]) has been proposed for Heisenberg-limited atom interferometers ([18]) and as a starting point for neutral atom quantum logic[19]. The important point here is the interesting parallel between *pure* quantum optics and *atom* quantum optics which will surely bring up new ideas and schemes to generate and implement quantum noise reduction and quantum state transfer between atoms and light.

Chapter 2

Squeezing and Phase Space

A cornerstone in quantum mechanics is the prediction that a pair of conjugate observables A, B , that is observables represented by noncommuting operators, can not simultaneously be measured with arbitrary precision. Instead the product between the uncertainty[1] in each observable is bounded by a lower limit as first discovered by Heisenberg[2]

$$\delta A \delta B \geq \frac{1}{2}|\langle[\hat{A},\hat{B}]\rangle| \tag{2.1}$$

The inequality sign is traceable to the Schwartz inequality and on the right hand side we have discarded the expectation value of the anticommutator[20]. From these observations its clear that to obtain the equality sign in Eq.(2.1) we must construct a quantum state $|\psi\rangle$ satisfying (i) $\hat{A}|\psi\rangle$ parallel with $\hat{B}|\psi\rangle$, and (ii) $\langle\psi|\hat{A}\hat{B}+\hat{B}\hat{A}|\psi\rangle = 0$. This state, called a minimum uncertainty state (MUS), in reality represents a whole class of states with all possible values of the sum[2] $\delta A + \delta B$. The lowest possible value for this sum is obtained for the MUS which has its noise equally distributed between the conjugate observables, i.e. $\delta A = \delta B$. We shall refer to this state as a coherent state. Any manipulation, either unitary Hamiltonian evolution or measurement induced quantum state reduction, which will bring the noise in one conjugate observable below the noise level in the coherent state is generally referred to as squeezing. We now examine a range of physical systems were squeezing is realized.

2.1 Free particle and the Wigner distribution

Consider a free particle in one dimension with mass m, and position q plus momentum p as conjugate observables, i.e. $[\hat{q},\hat{p}] = i\hbar$. We choose to work with scaled dimensionless observables $x = (\hbar/m\omega)^{-1/2}q$ and $y = (\hbar m\omega)^{-1/2}p$ where we have introduced the oscillator frequency ω anticipating later harmonic trapping of the particle. The coherent MUS for this system is a Gaussian wavepacket with equal width in both position and momentum space. The free particle Hamiltonian $\hat{H} = \hat{p}^2/2m = \hbar\omega\hat{y}^2/2$ will only induce a phaseshift in the momentum distribution, but increase the width of the Gaussian position distribution. From these well known observations we normally conclude that free evolution will take us out of the MUS. In fact this is not correct. To understand why we make a brief detour and introduce the important notion of phase space and Wigner quasi-probability distribution[21]

$$W(x,y) = \frac{1}{\pi}\int_{-\infty}^{\infty} ds e^{-i2ys}\langle\psi|\, x-s\rangle\langle x+s\,|\psi\rangle \tag{2.2}$$

---

[1] The uncertainty, variance or noise of an observable A is defined in the usual way : $\delta A^2 = \langle\hat{A}^2\rangle - \langle\hat{A}^2\rangle$.

[2] This statement makes sence if A and B have the same dimension. Alternatively we often construct A and B such that they are both dimensionless.

The usefulness of this distribution becomes apparent when integrating out the momentum observable y. Applying the definition of the delta function $\delta(s)$ leaves us with the probability distribution for the conjugate observable $P(x) = |\langle x|\,\psi\rangle|^2$. The same argument can be applied with x and y interchanged. Thus the Wigner function gives a qualitative tool to simultaneously visualize the noise in conjugate observables as well as a quantitative tool to calculate any moment of the phase space observables. Eq.(2.2) looks quite complicated but there is a way to dramatically simplify it. Set $x = y = 0$ and introduce the parity operator $\hat{\Pi}_0 = \int ds\,|-s\rangle\langle s|$ which takes the wave function $\psi(s) = \langle s|\,\psi\rangle$ into $\psi(-s) = \langle -s|\,\psi\rangle$. The Wigner function at the origo of phase space is simply the expectation value of this parity operator. For an arbitrary point (x, y) in phase space we introduce the displaced parity operator as

$$\hat{\Pi}(x,y) = \hat{D}(x,y)\hat{\Pi}_0\hat{D}^{-1}(x,y) \quad (2.3)$$

$$\hat{D}(x,y) = \hat{D}^{-1}(-x,-y) = e^{-ix\hat{y}+iy\hat{x}} \quad (2.4)$$

With $y = 0$ in Eq.(2.4) we have $\hat{D}(x,0)\,|s\rangle = |x+s\rangle$ and therefore $\hat{\Pi}(x,0) = \int ds\,|x-s\rangle\langle x+s|$ which is the parity operator about the point $(x, 0)$ in phase space. It takes the wave function $\psi(x+s) = \langle x+s|\,\psi\rangle$ into $\psi(x-s) = \langle x-s|\,\psi\rangle$. Comparing these observations with Eq.(2.2) we see that the Wigner function at any point along the x-axis is simply the expectation value of the parity about this point. This is true for all points in phase space[22]

$$W(x,y) = \frac{1}{\pi}\langle\psi|\,\hat{\Pi}(x,y)\,|\psi\rangle \quad (2.5)$$

To further develop Eq.(2.5) as a basic tool we introduce the (non Hermitian) step operator $\hat{a} = 2^{-1/2}(\hat{x} + i\hat{y})$ along with the complex amplitude $\alpha = 2^{-1/2}(x + iy)$. Then we can replace $(x, \hat{x}, y, \hat{y})$ with $(\alpha, \alpha^*, \hat{a}, \hat{a}^\dagger)$ in Eq.(2.3-2.5) with the result

$$\hat{\Pi}(\alpha) = \hat{D}(\alpha)\hat{\Pi}_0\hat{D}^{-1}(\alpha),\ \ \hat{D}(\alpha) = \hat{D}^{-1}(-\alpha) = e^{\alpha\hat{a}^\dagger-\alpha^*\hat{a}} \quad (2.6)$$

$$W(\alpha) = \frac{1}{\pi}\langle\psi|\,\hat{\Pi}(\alpha)\,|\psi\rangle \quad (2.7)$$

We now return to wavepacket spreading of the free particle. The coherent MUS of a free particle is identical with the groundstate $|0\rangle$ of the same particle in a harmonic trap. The Wigner function for this state follows most directly from Eq.(2.7)

$$W^{(in)}(\alpha) = \frac{1}{\pi}\langle 0|\,\hat{D}(\alpha)\hat{\Pi}_0\hat{D}(-\alpha)\,|0\rangle = \frac{1}{\pi}\langle 0|\,\hat{D}(2\alpha)\,|0\rangle = \frac{1}{\pi}e^{-2|\alpha|^2} = \frac{1}{\pi}e^{-(x^2+y^2)} \quad (2.8)$$

where we use the obvious observations that operators $\hat{x}$ and $\hat{y}$ (and therefore also $\hat{a}$ and $\hat{a}^\dagger$) change sign under parity while the harmonic oscillator groundstate is a positive eigenstate of parity. The phase space contour is plotted in Fig.2.1 which displays the equal noise in x and y. The area limited by the $W^{(in)}$-contour corresponds to the smallest noise product $\delta x\delta y$ allowed by the commutator $[\hat{x}, \hat{y}] = i$. The free particle time evolution $\hat{U}(t) = \exp(-i\hat{H}t/\hbar)$ changes the position and momentum operators like $\hat{x}(t) = \hat{x}(0) + \hat{y}(0)\omega t$ and $\hat{y}(t) = \hat{y}(0)$. The corresponding evolution of the displacement operator $\hat{U}^\dagger(t)\hat{D}(x,y)\hat{U}(t) = \hat{D}(x - y\omega t, y)$ transforms the Wigner distribution as

$$W^{(out)}(x,y) = \frac{1}{\pi}\langle 0|\,\hat{\Pi}_0(x - y\omega t, y)\,|0\rangle = W^{(in)}(x - y\omega t, y) \quad (2.9)$$

This canonical transformation corresponds to shearing the phase space distribution as shown in Fig.2.1. Since the noise area is invariant during this shear we stay in the class of MUS which means that the particle has evolved into a squeezed vacuum state[3]. To verify the squeezing one can trap the

---

[3] We use the term "squeezed vacuum state" when the initial coherent MUS is the groundstate of the harmornic oscillator.

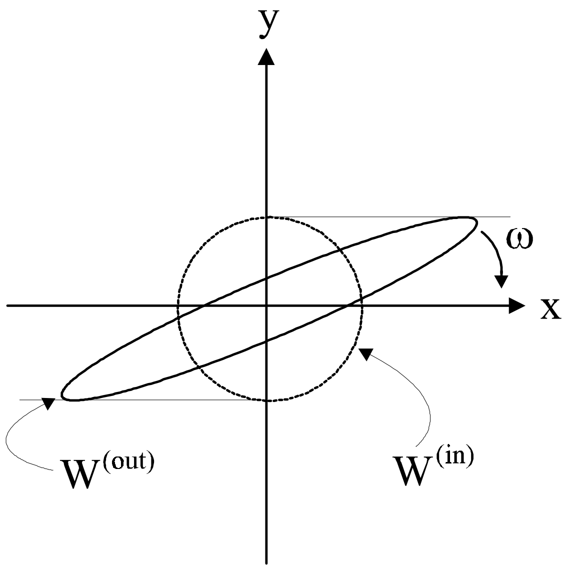

Figure 2.1: Contours of Wigner distributions in phase space. $W^{(in)}$ is the isotropic vacuum fluctuations. Free wavepacked expansion corresponds to a shearing of phasespace resulting in $W^{(out)}$. If the wavepacket is trapped in a harmonic oscillator (with frequency ω) the squeezing can be rotated into the momentum observable.

particle in a harmonic trap. The Hamiltonian $\hat{H} = \hbar\omega\hat{a}^\dagger\hat{a}$ of the trap will induce the time evolution $\hat{a}(t) = \hat{a}(0)e^{-i\omega t}$ which changes the displacement operator into $\hat{U}^\dagger(t)\hat{D}(\alpha)\hat{U}(t) = \hat{D}(\alpha e^{i\omega t})$. The change in Wigner function $W^{(out)}(\alpha) = W^{(in)}(\alpha e^{i\omega t})$ is just a clockwise rotation of the phase space distribution with angular frequency ω as indicated by the arrow in Fig.2.1. The trap will thus rotate the squeezing into the observable momentum distribution.

The above squeezing scheme has been realized experimentally by trapping $\sim$ 1000 cesium atoms in a harmonic 1D dipole trap and cooling each atom to the groundstate ($n = 0$) defining the initial coherent MUS[23]. The trap was turned off to allow free wavepacket expansion and then again turned on to rotate the squeezing into the momentum distribution which could be observed by ballistic expansion and CCD-imaging. The observed noise reduction was 6 dB (a factor of 4) compared to the initial coherent state.

2.2 RF parametric amplification

Consider now a charged particle in a radio frequency (RF) Paul trap as shown in Fig.2.2a. We are interested in harmonic motion along the trap z-axis and again take the coherent MUS to be the vibrational groundstate. The (scaled) ion position $z(t)$ in the unperturbed trap is represented by the operator

$$\hat{z}(t) = 2^{-1/2}(\hat{a}(t) + \hat{a}^\dagger(t)) = \hat{x}(0)\cos(\omega t) + \hat{y}(0)\sin(\omega t) \qquad (2.10)$$

In this notation we refer to the observables x, y as the *quadrature* components of the ion motion. Any displacement of the ion from the its equilibrium position induces a charge $q(t) = \alpha_i z(t)$ on the trap endcap electrodes, where the constant α_i depends on the ion charge and the trap geometry. Therefore the system is approximately equivalent to a simple series LCR circuit resonant at the Paul trap frequency $\omega = (LC)^{-1/2}$[24]. Imagine now that we parametrically drive this circuit by modulating the capacitance at twice the trap frequency as shown in Fig.2.2a. If the relative amplitude of the

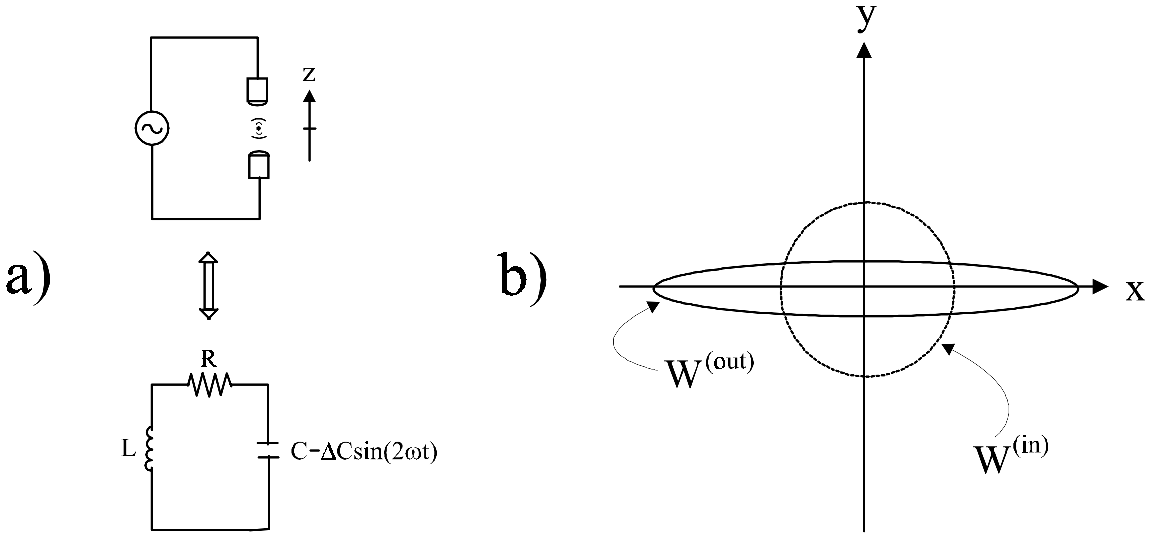

Figure 2.2: a) A 1D ion trap (ring electrode not shown) and its approximate equivalent LCR curcuit. By parametrically driving the resonance frequency (modulation $k = \Delta C/C$) the quadrature observables x/y of the ion motion along the trap z-axis are amplified/attenuated. b) The corresponding Wigner function in phase space is *squeezed*.

modulation $k = \Delta C/C$ is small the circuit equation takes the form

$$\frac{d^2q}{dt^2} + 2\gamma\frac{dq}{dt} + \omega^2(1 + k\sin(2\omega t))q = 0 \tag{2.11}$$

where $2\gamma = R/L$ is the full width at half maximum (FWHM) of the resonance. We expect the parametric drive to excite the quadrature components of the induced charge, i.e. the quadratures of the ion motion. Substituting Eq.(2.10) into Eq.(2.11) but now with time-dependent quadratures we find the (classical) solution

$$z(t) = q(t)/\alpha_i = x(t)\cos(\omega t) + y(t)\sin(\omega t) \tag{2.12}$$

$$x(t) = x(0)e^{(k\omega/2-2\gamma)t}, \;\; y(t) = y(0)e^{-(k\omega/2+2\gamma)t} \tag{2.13}$$

To analyze this solution we first neglect the finite width of the circuit, i.e. we set $\gamma = 0$. Then its clear that the parametric drive acts as a phase sensitive amplifier exciting the x-quadrature while attenuating the y-quadrature. With zero decay it is permissible to transform the result in Eq.(2.13) into an operator equation

$$\hat{x}(t) = \hat{x}(0)e^{r}, \;\; \hat{y}(t) = \hat{y}(0)e^{-r} \tag{2.14}$$

where we have defined the squeezing parameter $r = k\omega t/2$. Then the process acts on the coherent groundstate to redistribute the noise between the two quadrature observables. To see this we apply the transformation in Eq.(2.14) to the displacement operator and obtain the transformed Wigner distribution

$$W^{(out)}(x,y) = \frac{1}{\pi}\langle 0|\,\hat{D}(xe^{-r}, ye^{r})\hat{\Pi}_0(x,y)\hat{D}^{-1}(xe^{-r}, ye^{r})\,|0\rangle = W^{(in)}(xe^{-r}, ye^{r}) \tag{2.15}$$

Again this is a canonical transformation in phase space which preserves the MUS noise area while squeezing the noise out of the y-quadrature and into the x-quadrature. This squeezed vacuum state is shown in Fig.2.2b. Now it is clear from Eq.(2.13) that the decay of the oscillator is a phase-insensitve process which will most likely ruin the squeezed state. But to treat it correctly we must remember that any decay acts to introduce fluctuations into the system. In the next chapter we give a correct quantum treatment of the damped, parametrically driven oscillator. There is one more interesting observation from Eq.(2.13). When the parametric drive balances the decay we reach the threshold for stable parametric oscillations : $k_{th} = 4\gamma/\omega = 2/Q$ (where $Q = \omega/2\gamma$ is the oscillator quality factor).

As is clear from the above discussion the parametric drive is a small modulation of the resonance frequency. For the Paul trap one could achieve this by modulating the voltage between the endcap- and ring-electrode[24]. Alternatively one can irradiate the ion with two Raman beams which differ in frequency by 2ω. This creates an optical dipole force modulated at the difference frequency and thus acting as a parametric drive. This excitation scheme has been applied to a $^9\text{Be}^+$ ion cooled to the oscillator groundstate with the resulting quadrature noise reduction of a factor 40 ± 10[25]. The use of 2ω sideband Raman excitation of the groundstate ion reveals that the squeezed vacuum state is composed of even number states. We now extend the discussion of the RF-oscillator into the optical domain where the work presented in this thesis has been conducted.

2.3 Optical parametric amplification

Working with an RF- or microwave oscillator in the ground state is hard. This is evident when we calculate the equivalent temperature $\hbar\omega/k_B$ (4.8 mK at $\omega/2\pi = 1$ GHz) and remember that any decay to environment will couple in fluctuations and excite the oscillator to a level $n = (\exp(\hbar\omega/k_B T) - 1)^{-1}$ where T is the temperature of a thermal reservoir. Thus an ion in the Paul trap must be well isolated and laser cooled to the groundstate and a microwave resonator must be cooled to less than one Kelvin[4]. The obvious shortcut here is to work at optical frequencies. An optical cavity will isolate a mode of the electromagnetic field in the harmonic oscillator groundstate. For this system we define the quadratures in terms of the (scaled) cavity field operator

$$\hat{E}(t) = 2^{-1/2}(\hat{a}(t) + \hat{a}^\dagger(t)) = \hat{x}(0)\cos(\omega t) + \hat{y}(0)\sin(\omega t) \tag{2.16}$$

in complete analogy with Eq.(2.10). How can we squeeze the groundstate of this mode? By a parametric perturbation of the cavity resonance, but wiggling a solid mirror at an optical frequency is impossible. Instead we place a crystal inside the cavity. The crystal refractive index changes the cavity resonance and thus any modulation of the refractive index acts as a parametric drive. The fast index modulation is achieved with three wave-mixing between the cavity field E_ω and a pump field at twice the resonance frequency $E_{2\omega}$ (in this case the process we describe is parametric downconversion). The mixing strength is controlled by the crystal $\chi^{(2)}$-nonlinearity and we write the polarization p_ω, displacement d_ω and refractive index n_ω in the standard form

$$\begin{aligned} p_\omega &= \chi^{(1)}_\omega E_\omega + d_{nl} E_\omega E_{2\omega}, \;\; d_\omega = \epsilon_0 E_\omega + p_\omega = (\epsilon_\omega + d_{nl}E_{2\omega})E_\omega = n^2_\omega E_\omega && (2.17) \\ \Delta n_\omega &\approx \frac{d_{nl}E_{2\omega}}{2n_\omega}, \;\; k = \frac{\Delta\epsilon_\omega}{\epsilon_\omega} = \frac{d_{nl}E_{2\omega}}{\epsilon_\omega} && (2.18) \end{aligned}$$

where d_{nl} is the effective nonlinear coefficient for three wave mixing[26] and $n_\omega = (\epsilon_\omega)^{1/2}$ is the crystal bulk refractive index. Eq.(2.18) shows the variation of the cavity optical length at frequency 2ω and the parametric coupling strength proportional to the pump amplitude and nonlinear coefficient. In experiments d_{nl} is determined indirectly by the process of second harmonic generation (SHG). The nonlinear polarization $p_{2\omega} = d_{nl}E^2_\omega$ drives a second harmonic field and one measures the nonlinearity as $E_{NL} = P_{2\omega}/P^2_\omega$ where P_ω ($P_{2\omega}$) is the power of the fundamental (second harmonic). By comparison its clear that $d_{nl} \sim (E_{NL})^{1/2}$ which combined with Eq.(2.18) and the threshold $k_{th} = 2/Q$ shows that the threshold for optical parametric oscillation should go as $P^{th}_{2\omega} \sim 1/(E_{NL}Q^2)$. A more careful calculation (appendix A) confirms this result.

---

[4] Residual blackbody radiation is removed from the resonator by "vacuum cleaning" : a resonant Rydberg atom is sent through the cavity to absorb any thermal photon.

The system of optical resonator + nonlinear crystal + parametric pump is called an optical parametric amplifier (OPA) below threshold. Above threshold we refer to it as an optical parametric oscillator (OPO). By comparison with the resonant circuit model we expect the OPA to squeeze the vacuum state of the cavity field, i.e. redistribute the noise between the field quadratures as shown in Fig.2.2b. Furthermore the quantum nature of the parametric coupling is downconversion of one pump photon into two cavity photons. This will excite only even number states as expected for the squeezed vacuum state. The first experiment demonstrating the squeezing from the OPA was run at 1.06 μm with a $LiNbO_3$ crystal and achieved a noise reduction beyond 3 dB (factor of 2)[7].

2.4 Non-Gaussian Wigner distributions

The Ph.D.-work presented in this thesis (Chapters 3-7) uses the OPA described above with potassium niobate ($KNbO_3$) as nonlinear crystal. Even though the OPA approach has proven to be the superior way to implement squeezing in the laboratory, it has also demonstrated some limitations in manipulating phase space. The coherent dynamic rate available with todays nonlinear crystals is small compared to competing dissipative rates. This allows for a linearized description which limits phase space actions to the kind of Gaussian redistribution shown in Fig.2.2b, perhaps with an additional classical displacement of the oscillator. To achieve non-Gaussian distributions one can either project them out by conditional measurements or deterministically construct them in the strong coupling regime where the coherent dynamic rate beats dissipation.

The work in Ref.[27] in based on the idea of conditional projection onto a non-Gaussian distribution. In this case an ensemble of singe photon Fock-states $|1\rangle$ was prepared from photon pairs created in parametric downconversion (OPA but without cavity). Using pulsed homodyne tomography and taking into account detection efficiency the Wigner function was reconstructed with a nonclassical negative value around origo in phasespace. Ideally the single photon Fock state has the symmetric distribution (see Fig.2.3a)

$$W(a) = \langle 1| \hat{\Pi}(\alpha) |1\rangle = -\langle 1| \hat{D}(2\alpha) |1\rangle = -e^{-2|\alpha|^2} \langle 1| e^{2\alpha \hat{a}^\dagger} e^{-2\alpha^\star \hat{a}} |1\rangle = e^{-2|\alpha|^2}(4|\alpha|^2 - 1) \qquad (2.19)$$

In contrast a *deterministic* single photon Fock state is prepared inside a microwave cavity in Ref.[28]. This experiment is limited to probing the parity of the field which however directly demonstrates a negative Wigner function at the origo of phasespace. In Ref.[25] the motional state of a trapped beryllium ion is coherently prepared in an arbitrary Fock state $|n\rangle$. Performing measurements of displaced populations the Wigner distribution for $|1\rangle$ is reconstructed using tailored algorithms[29].

Another interesting class of quantum states are coherent superpositions of macroscopic distinct realizations of a particular system, also known as "Schrödinger cat states"[30]. In the case the physical system is a harmonic oscillator the macroscopic distinct states are realized by the coherent excitations $|\pm\beta\rangle$ with vanishing overlap $|\langle -\beta|\,\beta\rangle|^2 = \exp(-4|\beta|^2) << 1$. The Wigner distribution for the state $|\psi\rangle = |\beta\rangle + |-\beta\rangle$ is

$$W(\alpha) = \langle\psi| \hat{\Pi}(\alpha) |\psi\rangle = e^{-2|\alpha-\beta|^2} + e^{-2|\alpha+\beta|^2} + 2e^{-2|\alpha|^2} \cos[\beta\, \mathrm{Im}(\alpha)] \qquad (2.20)$$

Here we assume β real and use the coherent state properties : $\hat{\Pi}_0 |\beta\rangle = |-\beta\rangle$; $\hat{D}^\dagger(\alpha) |\beta\rangle = |\beta - \alpha\rangle$; and $\langle\alpha|\,\beta\rangle = \exp[-1/2(|\alpha|^2 + |\beta|^2) + \alpha\beta^\star]$. The first two terms in the cat state are Gaussian peaks at $\pm\beta$. If we truncate the Wigner function here we have an incoherent mixture $\hat{\rho} = 1/2(|\beta\rangle\langle\beta| + |-\beta\rangle\langle-\beta|)$. The final term in the cat state gives rise to interference structure and negative values in phase space as shown in Fig.2.3b. Mesoscopic versions of the cat state have been prepared in a microwave cavity[31], and for the motional state of a trapped beryllium ion[32]. The study of the cat state in a microwave cavity demonstrates the increased decay (towards an incoherent mixture) as the separation 2β in phase space is increased[31]. We now leave these exotic states and return to the more familiar Gaussian noise statistics generated inside the OPA.

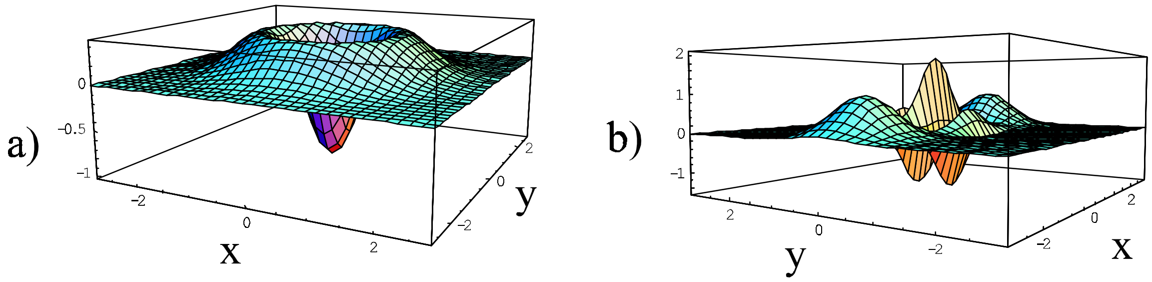

Figure 2.3: a) Wigner distribution for the 1 photon Fock state. b) Wigner distribution for a "Schrödinger cat"-state with $\beta = 2$. Note that both distributions have negative values in phase space (the distributions are not normalized).

Chapter 3

The Optical Parametric Amplifier

In Chapter 2 we introduced the picture of a parametric amplifier as a second harmonic "wiggling" of a resonant circuit (mechanical, electrical, optical,..). In this thesis we concentrate on the optical parametric amplifier (OPA) where the "wiggling" of the resonant field (annihilation operator $\hat{a}$) is caused by parametric downconversion from a classical pump mode β (real number) by way of the $\chi^{(2)}$-interaction coupling strength g

$$\hat{V} = \frac{i\hbar g}{2}(\beta \hat{a}^{\dagger 2} - \beta \hat{a}^2) \tag{3.1}$$

The Heisenberg operator solution for this nonlinear coupling is often written as a Bogoliubov transformation

$$\hat{a}^{(out)} = \mu \hat{a}^{(in)} + \nu \hat{a}^{\dagger (in)} \tag{3.2}$$

Here $\mu = \sinh(r)$, $\nu = \cosh(r)$, and $r = g\beta t$. The phase sensitive amplification of the OPA is evident when calculating the noise[1] in the conjugate quadrature observables $\hat{x} = \hat{a} + \hat{a}^\dagger$, and $\hat{y} = (\hat{a} - \hat{a}^\dagger)/i$

$$\begin{aligned} \hat{x}^{(out)} &= (\mu + \nu)\hat{x}^{(in)} \Rightarrow \langle \hat{x}^{(out)}, \hat{x}^{(out)} \rangle = (\mu + \nu)^2 \langle \hat{x}^{(in)}, \hat{x}^{(in)} \rangle && (3.3) \\ \hat{y}^{(out)} &= (\mu - \nu)\hat{x}^{(in)} \Rightarrow \langle \hat{y}^{(out)}, \hat{y}^{(out)} \rangle = (\mu - \nu)^2 \langle \hat{y}^{(in)}, \hat{y}^{(in)} \rangle && (3.4) \end{aligned}$$

This is all single mode results. Clearly we need a broadband analysis predicting the fluctuations with frequency ω from a leaky cavity with amplitude decay rate γ. The point is that the Bogoliubov transformation and quadrature spectra are unchanged in form if we adopt the following generalization[33]

$$\mu = \frac{1 + \epsilon^2 + \Omega^2}{(1 - i\Omega)^2 - \epsilon^2}, \quad \nu = \frac{2\epsilon}{(1 - i\Omega)^2 - \epsilon^2} \tag{3.5}$$

Here $\Omega = \omega/\gamma$, $\epsilon = \beta/\beta_{th}$, and $\beta_{th} = \gamma/g$ is the pump threshold for sustained oscillation. In the following section we use a somewhat elaborate analysis to "re-derive" the spectrum in Eq.(3.3) and (3.4), albeit expressed via the spectra $s(\omega) = \langle \hat{a}^\dagger, \hat{a} \rangle = |\nu|^2$ and $c(\omega) = \langle \hat{a}, \hat{a} \rangle = \mu\nu^\star$. Thus the reader familiar with squeezing spectra and their detection can in principle skip the rest of this Chapter an go directly to the experimental presentation in Chapter 4.

3.1 Theory

The basic components of the OPA and homodyne detection setup are shown for reference in Fig.3.1. We shall derive the observable homodyne spectrum following the line of reasoning in [34]. First the

---

[1] For two operators $\hat{A}$ and $\hat{B}$ we define : $\langle \hat{A}, \hat{B} \rangle = \langle \hat{A}\hat{B} \rangle - \langle \hat{A} \rangle \langle \hat{B} \rangle$. The same relation is used with classical variables A and B where brackets now mean time- or ensemble averages.

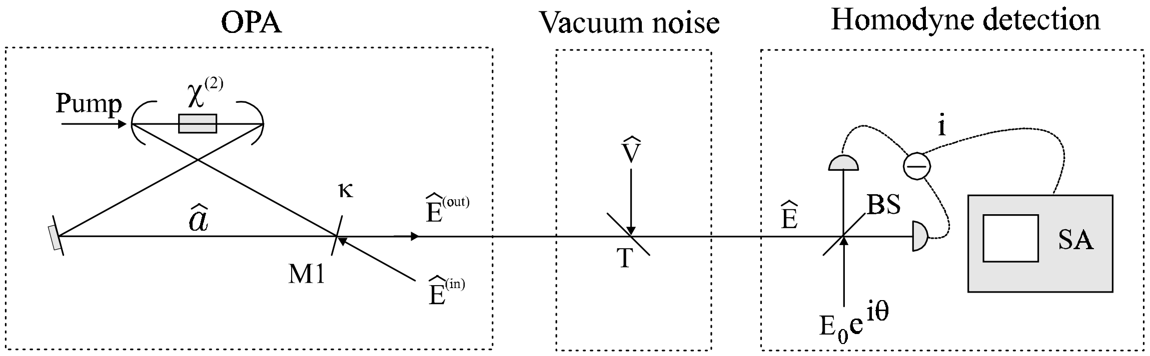

Figure 3.1: Scheme used to derive the OPA squeezing spectrum observed in balanced homodyne detection. The added vacuum noise represents imperfections in the experimental apparatus. The local oscillator phase θ defines the quadrature recorded by the electronic spectrum analyzer (SA).

OPA intracavity correlation spectrum is defined and calculated from the system master equation using the drift- and diffusion matrix from the equivalent linearized Fokker Planck equation. Next boundary conditions on the OPA output coupler (M1) are used to project cavity fluctuations onto the external field $\hat{E}^{(out)}$. To account for propagation loss, imperfect homodyne mode overlap and detector efficiency we mix the external field with a vacuum field $\hat{V}$ on an auxiliary beamsplitter with transmission T. The correlation spectrum of the field $\hat{E}$ after the beamsplitter is then linked to the measurement from the balanced homodyne detector. This approach is readily generalized to treat the more complicated problem of the nondegenerate OPA discussed in Chapter 5. In fact any quantum (optical) noise problem where the dynamics can be approximated by a linear drift term (classical) and a constant diffusion (quantum) can be solved by the scheme we are going to describe.

The operating principle of the OPA, namely three wave mixing in the form of parametric down-conversion, is modelled by the parametric interaction term

$$\hat{V} = i\hbar g(\hat{b}\hat{a}^{\dagger 2} - \hat{b}^{\dagger}\hat{a}^{2})/2 \tag{3.6}$$

The mode annihilation operators $\hat{a}$ ($\hat{b}$) for the fundamental (pump) obey the usual boson commutation relations and g is proportional to the effective nonlinear coefficient d_{nl} of the crystal[26]. We assume phasematching $\omega_b = 2\omega_a$ and work in the interaction picture relative to the frequency ω_a. The full dynamics of the parametric interaction give rise to a set of nonlinear coupled equations which are hard to solve. We linearize the problem by substituting a constant classical pump excitation $\langle\hat{b}\rangle = \beta$. The master equation for the OPA includes the amplitude decay at rate γ to a zero temperature or vacuum reservoir

$$\frac{\partial}{\partial t}\hat{\rho} = \frac{1}{i\hbar}[\hat{V}, \hat{\rho}] + \gamma(2\hat{a}\hat{\rho}\hat{a}^{\dagger} - \hat{a}^{\dagger}\hat{a}\hat{\rho} - \hat{\rho}\hat{a}^{\dagger}\hat{a}) \tag{3.7}$$

From this equation we want to extract second order moments defined as intracavity correlation spectra $s(\omega)$ and $c(\omega)$

$$s(\omega) = 2\gamma\mathcal{F}\{\langle : \hat{a}^{\dagger}(0), \hat{a}(\tau) :\rangle\}, \quad c(\omega) = 2\gamma\mathcal{F}\,\{\langle : \hat{a}(0), \hat{a}(\tau) :\rangle\} \tag{3.8}$$

The symbols (::) indicate time and normal ordering of operators and $\mathcal{F}$ is the Fourier transform with respect to τ. We next describe the calculation of these correlations. The Glauber-Sudarshan P-distribution can be used to make a coherent state expansion of the density operator

$$\hat{\rho} = \int d^2\alpha P(\alpha)\,|\alpha\rangle\,\langle\alpha| \tag{3.9}$$

This expansion combined with the operator rules

$$\hat{a}\hat{\rho} \Leftrightarrow \alpha P(\alpha), \;\; \hat{a}^{\dagger}\hat{\rho} \Leftrightarrow (-\partial/\partial\alpha + \alpha^{*})P(\alpha), \;\; \hat{\rho}\hat{a} \Leftrightarrow (-\partial/\partial\alpha^{*} + \alpha)P(\alpha), \;\; \hat{\rho}\hat{a}^{\dagger} \Leftrightarrow \alpha^{\star}P(\alpha) \tag{3.10}$$

is used to transform the master equation into an equivalent Fokker-Planck equation

$$\frac{\partial}{\partial t}P(\mathbf{x}) = \sum_{i,j}\left[\frac{\partial}{\partial x_i}\mathbf{A}_{ij}x_j + \frac{1}{2}\frac{\partial^2}{\partial x_i \partial x_j}\mathbf{D}_{ij}\right]P(\mathbf{x}), \tag{3.11}$$

where we introduce the vector $\mathbf{x} = (\alpha, \alpha^*)$ and the drift- and diffusion matrix

$$\mathbf{A} = \begin{bmatrix} \gamma & -g\beta \\ -g\beta^* & \gamma \end{bmatrix}, \quad \mathbf{D} = \begin{bmatrix} g\beta & 0 \\ 0 & g\beta^* \end{bmatrix} \tag{3.12}$$

It is well known that the Glauber-Sudarshan P-distribution is singular for fields displaying quantum behavior like squeezing. We see this problem here in the fact that the diffusion matrix is non-positive definite and the corresponding Fokker-Planck equation ill-defined. For problems of this type the Fokker-Planck equation is defined for the *positive* P-distribution where α^* is replaced by $\alpha^\dagger$ which must be considered an independent complex variable[35]. Continuing with this replacement we rewrite the Fokker-Planck equation in terms of an equivalent set of (classical) stochastic differential equations

$$\dot{\mathbf{x}} = -\mathbf{A}\mathbf{x} + \mathbf{B}\boldsymbol{\eta} \tag{3.13}$$

where $\mathbf{B}\mathbf{B}^{\mathbf{T}} = \mathbf{D}$ and the noise vector $\boldsymbol{\eta}$ has zero mean and the correlation $\langle \eta_i(t), \eta_j(t') \rangle = \delta_{ij}\delta(t - t')$[35]. All *normally ordered* operator correlations can now be evaluated by the substitution

$$\hat{a} \Leftrightarrow \alpha, \;\; \hat{a}^\dagger \Leftrightarrow \alpha^\dagger \tag{3.14}$$

We do not actually solve the stochastic equations (as done in Ref.[34]) but perform a simple matrix inversion to find the symmetric noise matrix

$$\mathbf{N}(\omega) \equiv \mathcal{F}\left\{\left\langle \mathbf{x}(0), \mathbf{x}^{\mathbf{T}}(\tau)\right\rangle\right\} = (\mathbf{A} - i\omega\mathbf{I})^{-1}\mathbf{D}(\mathbf{A}^{\mathbf{T}} + i\omega\mathbf{I})^{-1} \tag{3.15}$$

Here $\mathbf{I}$ is the identity matrix and the proof of this relation between the second order correlations and the drift- and diffusion matrix is given in appendix B. By direct comparison between Eq.(3.15) and Eq.(3.8) we find

$$s(\omega) = 4\epsilon^2/(M_+M_-), \;\; c(\omega) = 2\epsilon(1 + \Omega^2 + \epsilon^2)/(M_+M_-) \tag{3.16}$$

where $M_\pm = \left[(1 \pm \epsilon)^2 + \Omega^2\right]$ and we have defined the scaled fluctuation frequency $\Omega = \omega/\gamma$ and threshold parameter $\epsilon = g\beta/\gamma = \beta/\beta_{th}$. This completes the calculation of the intracavity correlation spectra. Next we look at the output field $\hat{E}^{(out)}$ of Fig.3.1 which is defined through the boundary conditions on the coupling mirror M1[36]

$$\hat{E}^{(out)}(t) + \hat{E}^{(in)}(t) = (2\kappa)^{1/2}\hat{a}(t) \tag{3.17}$$

Here κ is the amplitude decay rate of the cavity field through M1. The output field is mixed with the vacuum mode $\hat{V}$ on the beamsplitter BS

$$\hat{E} = T^{1/2}\hat{E}^{(out)} + (1 - T)^{1/2}\hat{V} \tag{3.18}$$

where T is the beamsplitter transmission. Next the definition of the cavity correlation spectra (3.8) is extended to the external field $\hat{E}$

$$S(\omega) = \mathcal{F}\{\langle : \hat{E}^\dagger(0), \hat{E}(\tau) : \rangle\}, \;\; C(\omega) = \mathcal{F}\{\langle : \hat{E}(0), \hat{E}(\tau) : \rangle\} \tag{3.19}$$

Eq.(3.17) and Eq.(3.18) combined with a vacuum input field $\hat{E}^{(in)}$ allow us to link the external correlation spectra to the cavity

$$S(\omega) = \bar{\eta}s(\omega), \;\; C(\omega) = \bar{\eta}c(\omega) \tag{3.20}$$

The generalized escape efficiency $\bar{\eta}$ is the probability for a cavity photon to generate a photoelectron in the homodyne detector. It is the product of the cavity escape efficiency $\eta = \kappa/\gamma$ and the beamsplitter transmission T, i.e. $\bar{\eta} = \eta T$. The external quadrature observable is $\hat{Q}_\theta(t) = \hat{E}e^{-i\theta} + \hat{E}^\dagger e^{i\theta}$ and its *normally ordered* fluctuation spectrum $\Phi_Q(\omega, \theta)$ shows the well known sinusoidal dependence on the quadrature phase θ

$$\Phi_Q(\omega,\theta) \equiv \mathcal{F}\{\langle : \hat{Q}_\theta(0), \hat{Q}_\theta(\tau) : \rangle\} = 2\bar{\eta}[s(\omega) + c(\omega)\cos(2\theta)] \tag{3.21}$$

Note that the negative value of Φ_Q for certain phases is a standard signature from a nonclassical field. In experiments we analyze the fluctuation level in a narrow frequency interval of the quadrature signal using homodyne detection. The signal $\hat{E}$ and phase coherent local oscillator $\langle \hat{E}^{(lo)} \rangle = E_0 e^{i\theta}$ are spatially overlapped on a 50/50 beamsplitter and the resulting detector currents $i_{1,2}(t)$ are subtracted to give the signal current $i(t)$ which probes the quadrature $\hat{Q}_\theta(t)$. The spectral density of fluctuations in this signal current, i.e. $\Phi_i(\omega,\theta) = \mathcal{F}\{\langle i(0), i(\tau)\rangle\}$, directly reflect the quadrature fluctuations $\Phi_Q(\omega,\theta)$ (see Appendix B)

$$\Phi_i(\omega,\theta) = 1 + \Phi_Q(\omega,\theta) \tag{3.22}$$

Here "1" defines the standard quantum limit (SQL) for uncorrelated vacuum fluctuations (the isotropic fuzz-ball in phase space) which is modified by the phase-dependent amplification inside the OPA. In all our experiments we use an electronic spectrum analyzer (SA in Fig.3.1) to record a time trace of the spectral integral $\Phi_i \Delta\omega$.Each point on this trace is obtained by mixing down the spectral fluctuations around ω, filtering them through the SA resolution bandwidth $\Delta\omega$ (RBW), and finally squaring the result. The output number still has a finite distribution which can be narrowed by further filtering through the video bandwidth (VBW)[37]. The SQL is obtained by blocking the OPA output ($\Phi_Q(\omega,\theta) = 0$ for vacuum). In this case the SA trace is the local oscillator shotnoise (in the RBW) and this trace is normalized to 1, i.e. it defines the SQL.

With unit efficiency $\bar{\eta} = 1$ it is easy to verify the normalized noise product $\Phi_i(\omega, 0)\Phi(\omega, \pi/2) = 1$ which confirms that the OPA in the ideal case generates a squeezed MUS. In real experiments we have to content with nonunit escape efficiency and the OPA state is no longer a MUS albeit still squeezed. This degradation has a simple pictorial interpretation in terms of folding Wigner distributions. The process of mixing in vacuum noise on a beamsplitter can be seen as folding the phase-sensitive OPA distribution with the phase-insensitive vacuum distribution. On the experimental level we say that the squeezed MUS is detectable because photon pairs from the OPA generate correlated photoelectrons which suppress the shotnoise contribution. Loosing a single photon in a pair degrades this part of the current correlation and thus the squeezing.

Close to threshold (again with $\bar{\eta} = 1$) the fluctuations and hence energy in the slowly varying components of the antisqueezed quadrature diverge ($\Phi_Q(0,0) \rightarrow \infty$). This is clearly unphysical and can be traced back to the semiclassical model where the pump mode is constant (infinite energy reservoir). The remedy then is to include pump depletion in the P-distribution, which amounts to the replacement $\beta \rightarrow (2E_p - g\alpha^2)/2\gamma_p$ and $\beta^* \rightarrow (2E_p - g\alpha^{\dagger 2})/2\gamma_p$ in the drift- and diffusion matrix[35]. Here E_p and γ_p are the pump excitation and decay rate. With this substitution it is still possible to find an exact potential solution to the Fokker-Planck equation with which any normally ordered moment can be calculated. As a result the predicted antisqueezing is finite when passing the threshold. The P distribution is only applicable when calculating instantaneous moments like the quadrature squeezing in the total cavity field. For obtaining correlation functions and their spectra we must translate the Fokker Planck equation to coupled stochastic equations as described above. But with pump depletion these equations are nonlinear and no solution exists. Today this is of little concern to the experimentalist since available nonlinear materials only give poor ratios $n_0^{-1/2} = \beta_{th}^{-1} = (g/\gamma)$ between the nonlinear- and dissipative rates (n_0 is the threshold photon number for the pump). The result obtained in this section is the zero order term for a perturbation expansion of the fundamental- and pump quadratures in n_0^{-1}[38]. In fact all squeezing experiments to date are well approximated by this zero order expansion which is equivalent to a linearized analysis which *always* predicts Gaussian quadrature distributions centered around a classical mean value[37]. More exotic phase space distributions like Schrödinger cat states, Fock states, etc. are observed in the strong coupling regime (where single quanta coherent dynamics beats dissipation) or via conditional detection (see Chapter 2).

Chapter 4

The OPA Construction and Squeezed Light Production

A quick survey through the early squeezed light feature editions (see [39]) immediately reveals that the OPA at that time (1987) was the optimal device to redistribute vacuum fluctuations[7]. This is also true today, 15 years later. In 1992 Polzik et. al.[40] demonstrated 6 dB quadrature noise reduction at 856 nm with $KNbO_3$. This result has been matched by the group of J. Mlynek who observed 6.2 dB amplitude noise reduction on a 0.2 mW wave at 1064 nm using a semi-monolithic MgO:$LiNbO_3$ OPA pumped by a frequency doubled Nd:YAG laser at 532 nm[41]. The best vacuum squeezing observed to date was reported by the group of H.-A. Bachor who used a compact monolithic MgO:$LiNbO_3$ OPA to produce 7 dB of vacuum squeezing again at 1064 nm. While the semi- or monolithic OPA operates at a fixed wavelength the construction in Ref.[40] is aimed at frequency tunability to allow spectroscopy on atomic dipole transitions. As described below we also base our OPA construction on this tunability principle.

All results in this thesis are obtained with an optical parametric oscillator (OPO) below threshold or OPA. But we should not forget that the OPO above threshold is a versatile tool for spectroscopic application now available with single device cw tuning ranging from 550 nm to 2830 nm[42]. Furthermore the quadrature squeezing naturally persists above the OPO threshold and new quantum phenomena emerge such as intensity noise correlation in the nondegenerate regime (see introduction in Chapter 6).

This Chapter has the following structure. In section 4.1 we motivate and explain the design and construction of our OPA cavity. The following section 4.2 demonstrates the operation of our second harmonic doubling cavity where we produce the pump for the OPA. Next we turn to the experimental setup and results in section 4.3, and finally summarize in section 4.4.

4.1 Cavity construction principles

The guiding principles for the construction of the OPA cavity (see Fig.4.1a) is the application of this device as a narrowband tunable source of (i) frequency nondegenerate quadrature entanglement as a tool in quantum information processing (Chapter 6), and (ii) polarization squeezed light for "back-action noise" studies in the interaction with spin polarized atomic cesium (Chapter 7).

4.1.1 Tunability

Pumping the OPA with a doubled Ti:Sapph (see section 4.2) we achieve a broad tuning range for the fundamental in the near infrared (750-950nm). Since the degree of squeezing is limited by the escape efficiency $\eta = \kappa/\gamma$ it is important to reduce any residual decay $\gamma - \kappa$ such as reflection- and bulk loss

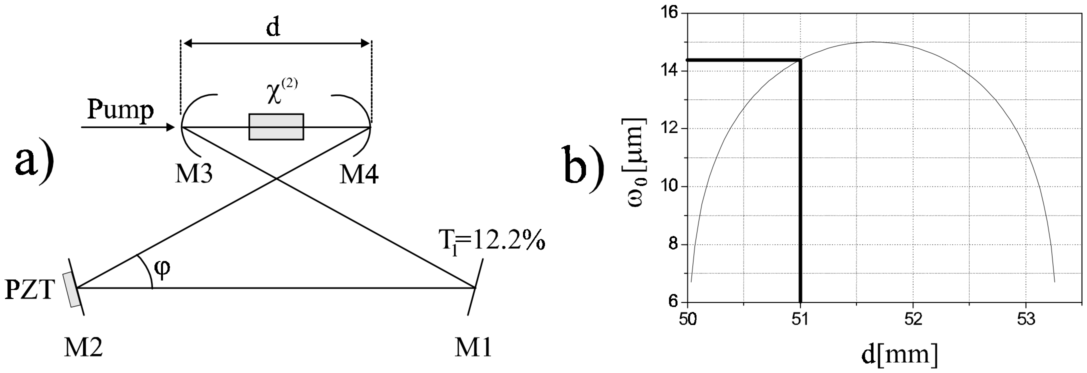

Figure 4.1: a) OPA cavity design. M1 is the input coupler (T=12.2% @860nm) while M2-M4 are high reflectors (T<200 ppm @860nm). The $\chi^{(2)}$ nonlinear crystal is a-cut KNbO$_3$. b) OPA cavity stability curve. M3 and M4 have ROC=50 mm and thus the empty cavity (no crystal) is stable above d=50 mm. We operate the empty cavity with d=51 mm. This number is increased by 5.7 mm to compensate the insertion of the 10 mm KNbO$_3$ crystal.

in the nonlinear crystal and residual scattering and absorption on cavity mirrors. Therefore the cavity mirrors M2-M4 are well polished substrates coated for high reflection in the cavity geometry (T<200 ppm, Research Electro Optics). There is a natural trade-off between the bandwidth and quality of the coating which in our case reduces the tuning range of the OPA to wavelengths centered around 780 nm and 860nm which are covered by the HR coating. Outside this region the escape efficiency decreases and the OPA mirrorset should be replaced. Inside the region we find the D2 dipole transition of atomic cesium (852 nm) and of atomic Rubidium (780nm) thus motivating the selected coating. These alkali elements are interesting candidates for interacting with nonclassical light since they can be laser cooled and trapped to give cold, dense targets[43]. At room temperature paraffin coated alkali vapour cells are promising candidates due to long coherence time for the spin-polarised groundstate and high vapour density[44],[45].

4.1.2 Bandwidth

The OPA bandwidth 2γ is set by the ratio between the cavity free spectral range Δ and the cavity quality factor Q. We want this bandwidth large compared to any resonance structure probed (white noise approximation) and large compared to the width of the low frequency technical noise from the Ti:Sapph laser. This can be achieved by increasing $\Delta = c/l$, i.e. decreasing the optical length l of the cavity. For the folded ring geometry (see Fig.4.1a) small l means large opening angle φ and undesirable astigmatism in the cavity mode. But the real limit on l is set by our goal (i) to demonstrate the quadrature entanglement between signal and idler mode shifted $\pm\,\Delta$ with respect to the degenerate cavity mode resonance (see Chapter 6). When observing the signal/idler quadrature we must supply a resonant local oscillator by splitting off part of the Ti:Sapph output and shifting it $\pm\Delta$ with acousto optical modulators (AOM). Since the AOM diffraction efficiency goes down at higher modulation frequency this limits Δ and therefore l. We now work with $l = 81$ cm, $\Delta = 370$ MHz and $\varphi = 8.8^\circ$ as a reasonable compromise. The OPA bandwidth is also increased by increasing the transmission T_1 of the output coupler M1 thus lowering the quality of the cavity. This approach is balanced by the corresponding increase in the OPA threshold power which scales as Q^{-2} (see Appendix A) and thus sets an upper limit[1] on T_1 due to blue light induced losses (see subsection 4.1.5). We work with $T_1 = 0.122$, $Q \approx 50$ and a bandwidth $2\gamma/2\pi \approx 7$ MHz (the quality/bandwidth will decrease/increase when we take into account the measured values of residual loss described below).

4.1.3 Cavity geometry

In Appendix A we "derive" the ABCD propagation law for the complex parameter $q(z)$ describing the curvature and beam waist of the Gaussian TEM$_{00}$ mode. The matrix $\mathbf{M}$ describing a single round-trip in the empty OPA cavity (no crystal) takes the form

$$\mathbf{M} = \mathbf{M}_{d/2}\mathbf{M}_R\mathbf{M}_{l-d}\mathbf{M}_R\mathbf{M}_{d/2} \tag{4.1}$$

Here d is the separation between the curved mirrors M3,M4 with radius of curvature R. $l-d$ is the long distance between M3 and M4 via the plane mirrors M1 and M2. The form of the individual matrices $\mathbf{M}_j$ is given in Eq.(A.29). For a stable cavity mode the waist and curvature must repeat after a single round-trip. Using the propagation law Eq.(A.28) this condition reads

$$q(\bar{z}) = \frac{Aq(\bar{z}) + B}{Cq(\bar{z}) + D} \tag{4.2}$$

where A,B,C and D are the matrix elements of $\mathbf{M}$ and $\bar{z}$ is the center between the curved mirrors since this was the origin of the round-trip matrix. Since the cavity mode should be focused to the minimum waist size ω_0 at this position we take $q(\bar{z})^{-1} = \lambda/\pi\omega_0^2$ (Eq.(A.21) with $R(\bar{z}) = \infty$). Next we solve Eq.(4.2) for $q(\bar{z})^{-1}$ and find the closed expression[26]

$$\omega_0 = \left(\frac{\lambda}{\pi}\right)^{1/2} \frac{B^{1/2}}{[1-A^2]^{1/4}} \tag{4.3}$$

The stability region of the cavity follows from the condition $|A| < 1$. This condition is satisfied when $R < d < R + R^2/l$ and only for this mirror separation can the cavity support a stable mode. Inserting the parameters $l = 81$ cm, $R = 5$ cm and $\lambda = 860$ nm we obtain the cavity stability curve $\omega_0(d)$ shown in Fig.4.1b. In Appendix A the optimal focused waist ω_0 for nonlinear conversion is calculated for a fixed crystal length l_c with the result $\bar{u}_c = l_c/z_0 = 5.68$. Taking $l_c = 10$ mm, $\lambda = 860$ nm and $n = 2.3$ (refractive index of KNbO$_3$) we find $\omega_0 = 14.5$ μm. We work with mirror separation $d = 51$ mm and waist close to the optimal (compare stability curve). At this point one might object that there was no reference to the crystal in the ABCD calculation. The propagation through the crystal is described by the matrix product $\mathbf{M}_n\mathbf{M}_{l_c}\mathbf{M}_{n^{-1}} = \mathbf{M}_{l_c n^{-1}}$ which simply reduces the effective crystal length from l_c to $l_c n^{-1}$. We can exactly compensate this effect by increasing the mirror separation by the amount $\delta d = l_c - l_c n^{-1} = l_c(n-1)/n$ in which case the waist ω_0 is left unchanged and the ABCD calculation applies. For $l_c = 10$ mm and $n = 2.3$ the distance between M3 and M4 should be increased by $\delta d \approx 5.7$ mm when inserting the nonlinear crystal into the empty cavity.

4.1.4 Nonlinear crystal

In second harmonic generation (SHG) part of the fundamental power P_α is converted into the second harmonic power P_β. We use the efficiency of SHG to establish experimentally the crystal quality through the (single pass) nonlinearity parameter $E_{nl} = P_\beta/P_\alpha^2$. The connection to the Hamiltonian coupling is $g \propto E_{nl}^{1/2}$ as shown in detail in Appendix A. Even the highest nonlinearity available on the market will not take us out of the low coupling regime $g/\gamma << 1$ but the OPA threshold pump power P_β^{th} scales as E_{nl}^{-1} and with high nonlinearity we obtain the same scaled pump parameter

---

[1] The lower limit on T_1 is set by the inequality $\kappa >> \gamma - \kappa$, i.e. the output coupling rate should be much larger than the residual decay rate.

$\epsilon = (P_\beta/P_\beta^{th})^{1/2}$ with lower pump power P_β. From a practical point of view this is useful. More important, low pump power reduces the blue light induced loss in $KNbO_3$ (see subsection 4.1.5). In addition to high nonlinearity the crystal bulk loss should be low for both the fundamental and pump. The reflection loss from the crystal surface is reduced by a dual-band AR-coating centered at 860/430 nm. Another relevant issue is the type of downconversion. Type II downconversion requires both polarization modes of the cavity to be resonant. This makes tuning a nontrivial task compared to type I with only a single resonant polarization mode. Guided by the stated criteria we work with a 10x3x3 mm a-cut Potassium niobate ($KNbO_3$) type I crystal. This crystal has noncritical 90° temperature phasematching over a tuning range from 840 nm to 960 nm corresponding to a phasematching temperature ranging from -25°C to 200°C[46]. Thus wavelength tuning the OPA is reduced to the simple task of tuning the crystal temperature. Unfortunately the structure of $KNbO_3$ and the presence of defects increases the infrared absorption in the crystal region where blue pump light is present. This process termed BLIIRA (Blue Light Induced Infrared Absorption) was studied in detail for $KNbO_3$ (430/860 nm) in Ref.[47]. The power dependent BLIIRA loss term $L_b(P_\beta)$ adds to the passive cavity loss L_c and reduces the escape efficiency

$$\eta = \frac{\kappa}{\gamma} = 1 - \frac{(\gamma - \kappa)}{\gamma} = 1 - \frac{L_c + L_b(P_\beta)}{T_1 + L_c + L_b(P_\beta)} = 1 - \frac{\epsilon\,[L_c + L_b(P_\beta)]}{(4E_{nl}P_\beta)^{1/2}} \tag{4.4}$$

In the last equality we used $\epsilon = (P_\beta/P_\beta^{th})^{1/2}$ and Eq.(A.7). We could try to reduce the detrimental effect of the BLIIRA decay channel by making it small compared to the output channel, i.e. increasing T_1. But this action increases the threshold pump power P_β^{th} and to fix the level of squeezing we have to increase the pump power P_β accordingly to keep the pump parameter ϵ constant. The higher pump power translates into higher BLIIRA and depending on the scaling of $L_b(P_\beta)$ the escape efficiency (for fixed ϵ) can in worst case decrease. To investigate the behavior $\eta(P_\beta)$ we use the last equality of Eq.(4.4). Here the output channel transmission T_1 for a given power P_β is automatically regulated to keep the pump parameter ϵ fixed. We now describe the measurement of $L_b(P_\beta)$ and E_{nl} from which we can calculate $\eta(P_\beta)$.

4.1.5 BLIIRA, nonlinearity, and escape efficiency

In Appendix A we discuss experimental schemes to determine the OPA cavity loss. While scanning the cavity length (piezo mirror M2) we monitor a probe beam reflected from the input coupler M1 and observe the dip in reflected power on resonance. Normalizing the reflected power on resonance $P_r(0)$ to the power reflected off resonance $P_r(\infty)$ we can calculate the loss Eq.(A.14)

$$L_c + L_b = T_1 \frac{1 - r}{1 + r} \tag{4.5}$$

Here $r = (P_r(0)/P_r(\infty))^{1/2}$ and the coupler transmission is $T_1 = 0.122$. Without pump light we measure the passive losses $L_c = (0.7 \pm 0.1)\%$. Making sure the crystal temperature is tuned off phasematching we now repeat the measurement with different pump powers P_β and obtain the BLIIRA scaling $L_b(P_\beta)$ plotted in Fig.4.2a. The wavelength selection for these measurements is motivated by (i) the Cesium D1 dipole transition at 852 nm and (ii) reduced BLIIRA and room temperature phasematching of $KNbO_3$ at 860 nm. On a day to day basis we use a different approach to measure light induced losses. A probe beam is injected through the high reflector M2 and the power $P_t(L_b)$ transmitted trough the coupler M1 is monitored for different BLIIRA levels L_b. Defining the ratio $r = P_t(0)/P_t(L_b)$ we calculate the light induced loss Eq.(A.16)

$$L_b = (T_1 + L_c)(r^{1/2} - 1) \tag{4.6}$$

A measurement series monitoring the transmitted probe at 860 nm is added to Fig.4.2a thus demonstrating agreement between the reflection and transmission scheme. The observed level of

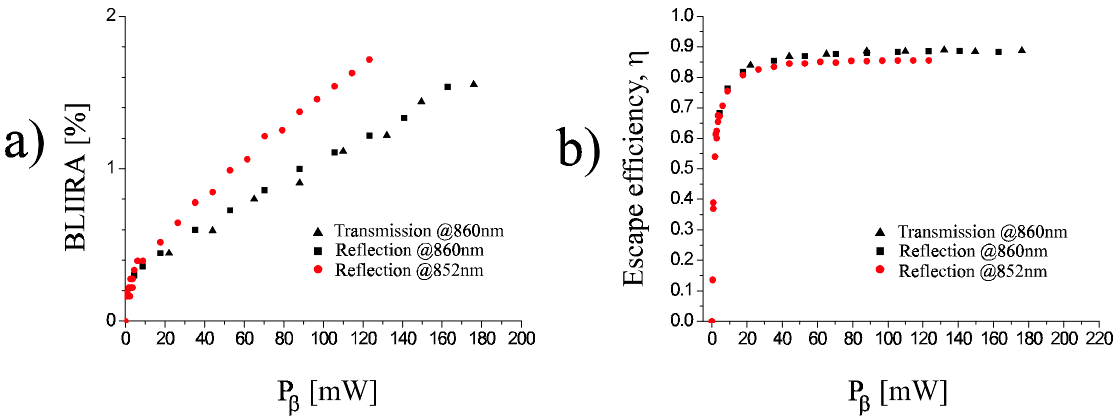

Figure 4.2: a) BLIIRA as a function of the pump power inside the OPA cavity. We observe BLIIRA either as a increased reflection dip or a reduced cavity transmission. b) OPA cavity escape efficiency aginst the pump power level. Data points are calculated from Eq.(4.4) with fixed pump parameter $\epsilon = 0.6$, $L_c = 0.7\%$, $E_{nl} = 0.015$ W^{-1}. BLIIRA data $L_b(P_\beta)$ are taken from (a).

BLIIRA and the wavelength dependence is in good qualitative agreement with previous studies of this effect in a-cut KNbO$_3$ [47]. In this work the authors used a high finesse cavity with $T_1 << L_c + L_b$ thus increasing the sensitivity in the reflection and transmission monitoring. We are going to convert the datapoints $L_b(P_\beta)$ into a plot of the power-dependent escape efficiency $\eta(P_\beta)$ using Eq.(4.4). For this purpose we first measure the singlepass nonlinearity E_{nl} via cavity enhanced SHG. The fundamental (860 nm) beam with power P_α is transmitted through the coupler M1. The power in the OPA cavity P_c is enhanced by the buildup factor Eq.(A.17)

$$\frac{P_c}{P_\alpha} = \frac{4T_1}{(T_1 + L_c + L_b)^2} \tag{4.7}$$

This expression is correct when we are off phasematching. We now tune the crystal temperature to the peak of the phasematching curve by optimizing the blue power $P_\beta = E_{nl} P_c^2$ in SHG. This nonlinear conversion corresponds to an additional loss $E_{nl} P_c$ for the cavity field which adds to the denominator of Eq.(4.7). Eliminating reference to the cavity field the buildup factor takes the form

$$\frac{P_\beta^{1/2} E_{nl}^{-1/2}}{P_\alpha} = \frac{4T_1}{(T_1 + L_c + (P_\beta E_{nl})^{1/2})^2} \tag{4.8}$$

where we set $L_b = 0$ since the typical blue power levels are on the μW-scale. From a careful measurement of P_α and P_β we solve Eq.(4.8) for the unknown nonlinearity. This procedure is repeated to optimize E_{nl} while changing the cavity waist ω_0, crystal position, angle and temperature. For the results presented in this chapter we are working with $E_{nl} = (0.015 \pm 0.002)$ W^{-1}. We now return to Eq.(4.4) and calculate the power dependent escape efficiency $\eta(P_\beta)$ from the BLIIRA data in Fig.4.2a. For the fixed pump parameter $\epsilon = 0.6$ we get the escape curve shown in Fig.4.2b[2]. From this curve we see that the escape efficiency is improved by only a few percent over the pump region 60-160 mW. Based on this observation we can in principle work with pump levels around 60-80 mW. But as described below we produce more than 200 mW blue pump light in SHG and typically end up working with pump levels around 150 mW. Taking $\epsilon = 0.6$ and $P_\beta = 150$ mW the threshold is $P_\beta^{th} = 417$ mW.

---

[2] For fixed ϵ this curve is defined for $P_\beta > P_\beta^{\min} = (\epsilon L_c)^2 / 4E_{nl}$

With $L_b \approx 1.2\%$ this threshold corresponds to a coupler transmission $T_1 = 0.14$ which is close to our choice $T_1 = 0.122$.

We have measured the transmission of the pump coupling mirror M3 to be 0.9 and the reflection off the crystal surface to be 0.02[3]. The same numbers are measured for the external SHG-cavity where we produce the pump. Adding the propagation efficiency 0.9 from the SHG cavity to the OPA cavity we find that the pump power $P_\beta = 150$ mW inside the OPA cavity corresponds to roughly 215 mW inside the SHG cavity. We include here a brief description of the external SHG cavity used to generate the pump for the OPA.

4.2 External cavity enhanced SHG

The geometry of the SHG cavity is a copy of the OPA folded ring shown in Fig.4.1a. The cavity length is $l = 70$ cm and the waist ω_0 is increased to 16 μm which to some extent reduces the effect thermal lensing in the 10x3x3 mm $KNbO_3$ crystal[48]. The enhancement of the nonlinear conversion is optimized for an impedance matched cavity[49]. Impedance matching is achieved when there is complete destructive interference between the directly reflected field from the coupler M1 and the cavity leakage field. According to Eq.(A.13) this happens on resonance when the coupler transmission equals the residual cavity loss, i.e. when $T_1 = L + E_{nl}P_c$ where we have defined the sum $L = L_c + L_b$. For the impedance matched cavity the buildup factor then takes the very simple form

$$\frac{P_c}{P_\alpha} = \frac{4T_1}{(T_1 + L + E_{nl}P_c)^2} = \frac{1}{T_1} \tag{4.9}$$

From this relation we can rewrite the power dependent conversion loss $E_{nl}P_c$ in the form $E_{nl}P_\alpha/T_1$ which clearly displays the dependence on the coupler transmission. Substituting this last expression into the matching condition we obtain the second order equation $T_1 = L + E_{nl}P_\alpha/T_1$. The solution returns the impedance matched coupler transmission T_1 in terms of the cavity loss L (including BLIIRA[4]), the nonlinearity E_{nl} and the fundamental input power P_α

$$T_1 = L/2 + \left[(L/2)^2 + E_{nl}P_\alpha\right]^{1/2} \tag{4.10}$$

Using the standard experimental techniques described in the previous section we measure the SHG-cavity parameters : passive loss $L_c = 0.009 \pm 0.001$, nonlinearity $E_{nl} = 0.011\ \mathrm{W}^{-1}$ and estimated BLIIRA $L_b(200\ \mathrm{mW}) = 0.010$ (860 nm). Substituting these parameters into Eq.(4.10) we plot in Fig.4.3a the optimal coupler transmission T_1 against the input power P_α. With 400-600 mW from the Ti:Sapph laser the coupler transmission should be $8 - 9$ percent. We work with $T_1 = 0.078$ in the experiment. For the impedance matched cavity the conversion efficiency follows directly from Eq.(4.9,4.10)

$$\eta = \frac{P_\beta}{P_\alpha} = \frac{E_{nl}P_c^2}{P_\alpha} = \frac{E_{nl}P_\alpha}{T_1^2} = \frac{E_{nl}P_\alpha}{\left[L/2 + [(L/2)^2 + E_{nl}P_\alpha]^{1/2}\right]^2} \tag{4.11}$$

where P_β is the second harmonic power. This maximal conversion efficiency at 860 nm is shown for reference in Fig.4.3b (dotted curve). Also on this graph we plot the (experimentally relevant) conversion efficiency for fixed transmission $T_1 = 0.078$ (solid curve). We observe that fundamental powers P_α relatively far from the the impedance matched value (400 mW) are converted with efficiencies close to the maximal. Experimental data obtained from doubling 860 nm are added as dots to Fig.4.3b. The data clearly suggest that there is room for improvement. On a day to day basis we operate with $P_\alpha \sim 500$ mW and $\eta \sim 0.55$ and thus produce $P_\beta \sim 275$ mW inside the SHG cavity. According to

---

[3] The Fresnel reflection with $n = 2.3$ and AOI=0 degrees is $R = 0.047$. But the crystal AR-coating is dualband and this explains the reduced reflecion at 430 nm.

[4] We neglect the BLIIRA depence on input power and coupler transmission and just substitute the BLIIRA level measured at the work point of the SHG cavity ($\sim$ 200 mW).

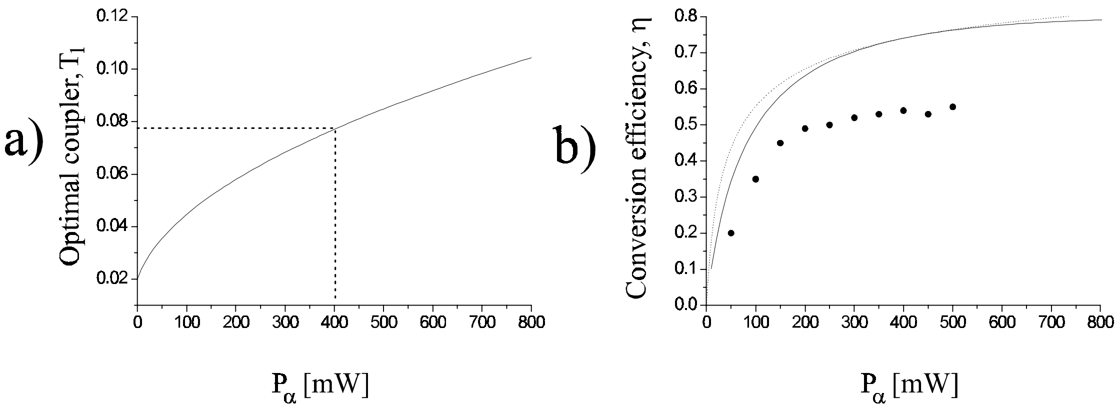

Figure 4.3: a) Optimal input coupler transmission T_1 for different pump powers. The curve is calculated from Eq.(4.10) using $L_c = 0.9\%$, $L_b \simeq 1\%$, and $E_{nl} = 1.1\%/W$. b) SHG conversion efficiency as a function of pump power. The dotted curve shows the impedance matched cavity, while the solid curve is the theoretical limit of our SHG cavity ($T_1 = 7.8\%$ plus parameters from (a)). Solid points are experimental conversion efficiencies.

the discussion at the end of the previous section this is an acceptable level for pumping the OPA. We now return to the experimental characterization of the OPA and the squeezing experiment.

4.3 Production of Squeezed light

First we demonstrate classical phase-sensitive amplification in the OPA and determine the pump parameter ϵ (subsection 4.3.1). This is followed by a discussion of the squeezing setup in subsection 4.3.2. Finally, we describe the experimental steps in squeezed light production and compare the obtained results with theory (subsection 4.3.3).

4.3.1 Parametric amplification

The vacuum fluctuations of the optical field, i.e. the fluctuations in the harmonic oscillator groundstate, are isotropically distributed in the phase space spanned by a conjugate pair of quadrature observables. As discussed in detail in Chapter 2 the deterministic squeezing of these variables requires phase-sensitive dynamics. If further the phase space area is preserved (canonical evolution) then we produce the anisotropic phase space distribution with fluctuations below the SQL for a given axis. The OPA with its phase-sensitive amplification should produce an anisotropic fluctuation spectrum in a homodyne measurement as shown in Chapter 3. Thus it is important to establish the phase-sensitive operation of the OPA. We do this in the classical regime by injecting a strong coherent probe beam through the highreflector M2 and monitor its transmission through the coupler M1 (see Fig.4.1a). This setup is identical to that used in the BLIIRA transmission measurement described in subsection 4.1.5 but this time we tune the crystal temperature to the peak of the phasematching curve. The normalized transmission of the probe $V(\epsilon, \varphi)$ is a function of the OPA pump parameter $\epsilon = (P_\beta / P_\beta^{th})^{1/2}$ and the relative phase φ between the probe and pump field. The exact dependence can be obtained from the Heisenberg OPA-equations with operators replaced by classical average values. The details

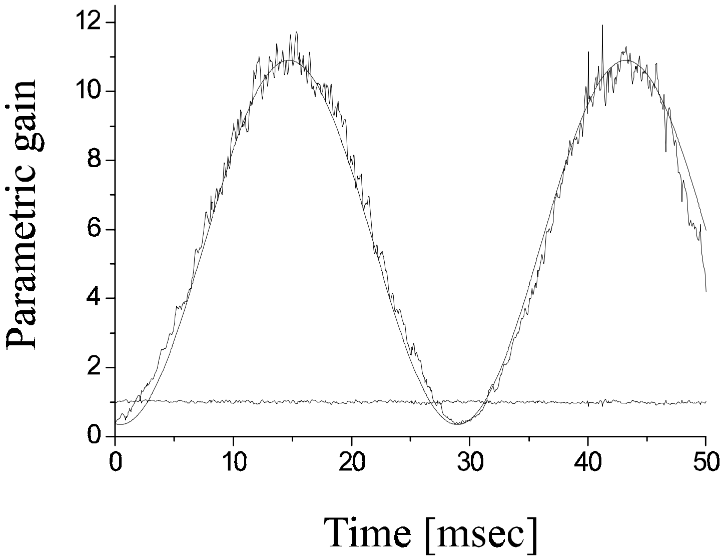

Figure 4.4: Classical phasesensitive amplification. The observed signal is the OPA transmission of a classical probe field. The time trace corresponds to a linear modulation of the probe phase relative to the pump phase. The flat trace (normalized to 1) is obtained with the pump blocked, while the phasesensitive signal is monitored with a 200 mW pump. From the sinusoidal fit (4.12) we extract the pump parameter $\epsilon = 0.7$ which defines the operating point when analyzing squeezing traces.

of this calculation can be found in Appendix A and here we only reproduce the result in Eq.(A.11)

$$V(\epsilon, \varphi) = \frac{P_1}{P_2} = \frac{4T_1T_2}{(T_1 + L_c + L_b)^2} \left[\frac{1}{|1+\epsilon|^2} \cos^2(\varphi) + \frac{1}{|1-\epsilon|^2} \sin^2(\varphi) \right] \tag{4.12}$$

In Fig.4.4 we plot a single trace of the observed probe transmission normalized to $V(\epsilon = 0)$. During the time interval displayed on the x-axis we perform a linear displacement of an external probe piezo mirror and hence of the phase φ. The parametric gain observed is a clear demonstration of the phase-sensitive operation of the OPA. The solid curve in Fig.4.4 is a least square fit using the expression in Eq.(4.12). From this fit we extract the pump parameter $\epsilon = 0.70$. The pump power in this particular gain measurement is $P_\beta = 200$ mW which combined with ϵ gives the threshold power $P_\beta^{th} = 408$ mW. From Eq.(A.7) the combination of P_β^{th} with $T_1 = 0.122$, $L_c = 0.007$ and $L_b(200 \text{ mW}) \simeq 0.016$ gives $E_{nl} = 0.013$ W^{-1}. This number compares well with the nonlinearity measured by cavity enhanced SHG with the same geometry.

4.3.2 Squeezing setup

A schematic outline of the setup is shown for reference in Fig.4.5. We run the experiment with a homebuild Ti:Sapphire laser[5] pumped by a 10 W Verdi system. Most of the Ti:Al_2O_3 output at frequency ω_a is directed to the SHG cavity while a small fraction is split off (M8) to produce the resonant and phase-coherent local oscillator LO (M7) and the probe beam (M6) and locking beam (M5) for the OPA. Detector D1 monitors the SHG cavity leakage field through M13. The phase of this field changes sign when scanning the cavity length across resonance (piezo mirror M11). In addition

---

[5] This laser is copy of the commercial MBR110 from Microlase (now Coherent)

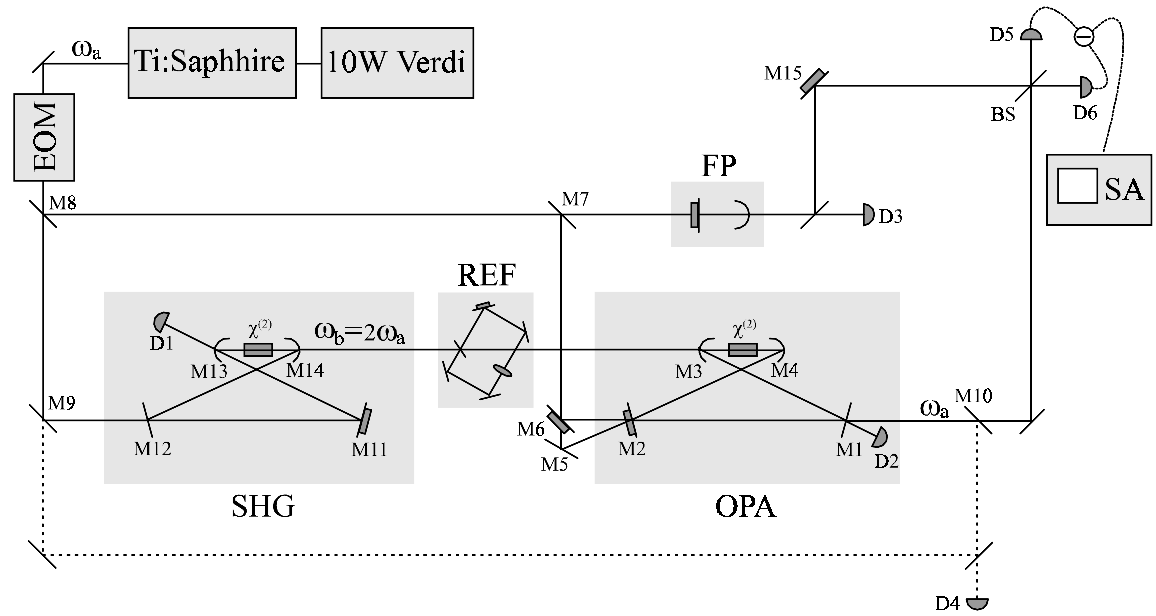

Figure 4.5: Setup for squeezing experiments. See text for detais.

the field amplitude changes linearly with small cavity detuning thus providing an error signal. The sign of the detuning is however lost in direct detection since we beat the leakage field with itself. The solution then is to beat the leakage field with a reference field which has a constant phase across resonance. We use as phase-reference the first order FM sidebands at ±19 MHz (EOM) as proposed in Ref.[50]. Homodyning the 19 MHz beatnote with a local oscillator we generate the DC error-signal allowing us to lock the external doubling cavity to the laser line ω_a. The spatial mode of the second harmonic pump field ($\omega_b = 2\omega_a$) propagating from M14 to M3 is shaped to optimize the nonlinearity in the OPA cavity. This "shaping" is completed by matching the spatial profile of the the second harmonic from *both* the SHG- and OPA cavity to the same blue reference cavity (REF). The second harmonic from the OPA side is generated by re-routing the SHG pump, i.e. removing M9 and inserting M10. Now the reflected field from the input coupler M1 probes the cavity resonance and the cavity length is locked to ω_a by feeding back the demodulated error-signal (D2) to the piezo mirror M2. This doubling configuration of the OPA is also used to measure (i) the nonlinearity E_{nl} of the OPA crystal by observing the second harmonic behind M3, and (ii) the intracavity losses $L_c + L_b$ by monitoring the DC reflection dip on resonance. With the SHG pump back in place (M9 in and M10 out) we now inject into the OPA a locking beam (M5) counter-propagating the squeezed field. The transmission of the locking beam is monitored by D2 and the derived error signal stabilizes the cavity length to ω_a. In this configuration the classical probe field (M6) is co-propagating with the squeezed field allowing us to (i) derive the propagation loss T_P between the OPA and homodyne detector, (ii) measure the parametric gain, and (iii) measure the visibility ξ of the interference fringe between the LO- and squeezed mode overlap on the homodyne 50/50 beamsplitter (BS). The spatial mode of the local oscillator is cleaned by a Fabry Perot resonator (FP) which is locked on the side of the TEM_{00} transmission fringe (D3). In this way we obtain intensity control and stability (0.1%) but the real gain is the improved visibility ξ. The homodyne fluctuation spectrum monitored by the electronic spectrum analyzer (SA) derives from fourth order amplitude correlations of the fields (see Appendix B). Therefore ξ enters as a square in the effective escape efficiency $\bar{\eta}$ and near unit visibility is essential. Returning to point (ii) we monitor the parametric amplification (D4 with M10 inserted) while scanning the probe phase (PZT M6). The parametric gain is optimized by tuning the crystal temperature and from a trace like

Fig.4.4 we derive the pump parameter ϵ. This procedure selects the working point for squeezed light production, i.e. optimal crystal temperature for given OPA pump power. Next the probe is blocked, M10 removed, and the LO cleaning cavity (FP) locked. In this configuration we scan the LO phase θ (PZT M15) and record the squeezing spectrum $\Phi_i(\omega, \theta)$ (SA). This spectrum is normalized to the phase-independent shotnoise level recorded with the OPA output blocked. We have already discussed several factors that limit the observed squeezing such as the escape efficiency η, propagation loss T_p and homodyne visibility ξ. Another important limiting factor is the finite quantum efficiency α of the homodyne detectors (D5,D6). The fourth order squeezing correlation scales like α^2 while the second order shotnoise is linear in α. The contributing factor in $\bar{\eta}$ is the ratio $\alpha^2/\alpha = \alpha$. We work with specially designed Silicon PIN photodiodes from Hamamatsu Photonics manufactured with AR coated surface and specs promising $\alpha = 0.995$. Unfortunately these diodes are rather old (1994-95) and based on reflection measurements which show that the AR coating has deteriorated we estimate $\alpha = 0.98$. We now display squeezing data recorded along the lines described in this section and compare them with theory.

4.3.3 Squeezing experiment

Guided by the discussion of BLIIRA and its effect on the OPA escape efficiency shown in Fig.4.2b we pump the OPA with 180 mW. Correcting for the 0.9 transmission through the curved mirror M3 and 0.02 reflection loss from the KNbO$_3$ surface we have $P_\beta = 159$ mW inside the OPA cavity. The spatial modematching to the blue reference cavity (REF) is approximately 0.95 (0.97) from the SHG (OPA) side and the effective pump power interacting with the OPA mode is further reduced by 0.92. Modematching from the OPA side is combined with (i) optimization and measurement of the nonlinearity $E_{nl} = 0.015$ W^{-1} (ii) measurement of intracavity losses $L_c = 0.007$ and $L_b = 0.015$ from the resonance reflection dip. The BLIIRA level is confirmed from the reduced probe transmission with the OPA pump present and crystal temperature detuned from phasematching. With phasematching conditions restored the pump parameter $\epsilon = 0.62$ is derived from probe parametric gain $(1-\epsilon)^{-2} = 6.8$. This gain corresponds to $P_\beta^{th} = 385$ mW. An independent threshold estimate follows from (A.7) : $P_{th} = \pi^2 Q^{-2} E_{nl}^{-1} = 346$ mW where we used the cavity quality factor $Q = 2\pi/(T_1 + L_c + L_b) = 43.6$. From the free spectral range $\Delta = 370$ MHz we calculate the OPA bandwidth $\gamma = \Delta/2Q = 4.2$ MHz (HWHM). To observe noticeable quadrature squeezing we must analyze frequency components ω within this bandwidth, i.e. we should sample the homodyne current at intervals ω^{-1} longer than the cavity lifetime γ^{-1}. At frequencies below 700 kHz we can not reliably establish the LO shot noise level even after 30 dB cancellation of excess technical noise in the balanced homodyne detector[6]. Based on these arguments we tune the peak response of the detector circuit to $\omega/2\pi = 1.15$ MHz. The RF-spectrum analyzer (SA) is set to monitor a resolution band $\Delta\omega = 30$ kHz (RBW) around this frequency. With these settings and 5 mW LO power we block the OPA output and record trace (a) shown in Fig.4.6. With a shotnoise limited LO we expect trace (a) to go down 3 dB if we block either one of the balanced squeezing detectors. Instead we find it increasing by 4 dB indicating 7 dB of technical noise on top of shotnoise. The 30 dB balancing reduces this technical noise level to 0.5 % relative to shot noise. To further establish trace (a) as the correct shot noise level we measure it again on a linear scale and confirm that it varies linearly with LO power. We now block both the OPA and LO and observe that trace (a) drops by 11.76 dB to the detector electronic noise-floor. Thus the ratio of electronic noise to shotnoise is $z = 0.07$. With both OPA and LO unblocked we record trace (b) which has been normalized to the standard quantum limit (SQL), i.e. the shot noise level from trace (a). The data shown in Fig.4.6 are corrected for the detector electronic noise. If the signal B (linear scale) represents the "raw" or laboratory form of trace (b) then the corrected trace shown in Fig.4.6, call it b (logarithmic scale), is related to B and z as

$$b = 10 \log \left[B(z+1) - z \right] \tag{4.13}$$

---

[6] We produce an amplitude modulation sideband at ω by passing the LO through an acousto optic modulator. This sideband is suppressed by 30 dB when the homodyne detectors D5 and D6 are balanced.

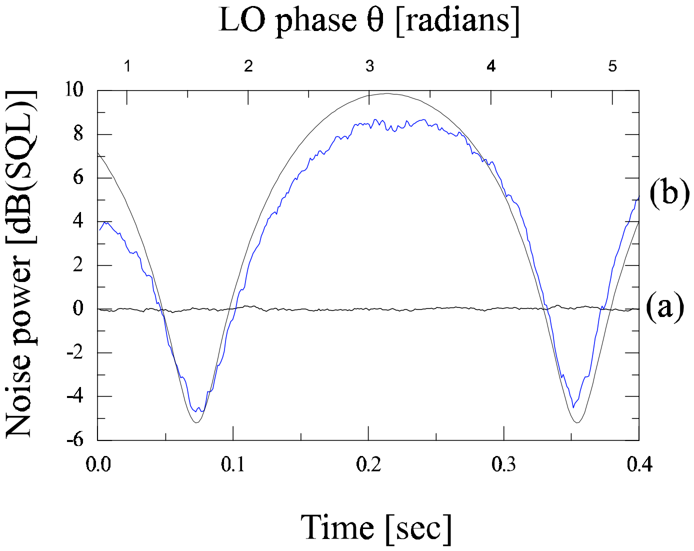

Figure 4.6: Squeezed vacuum. The noise power in the homodyne detection signal is measured during a scan of the LO phase θ. Aquisition parameters are @860nm, ω = 1.15 MHz, RBW=30 kHz, and VBW=30 Hz. With the OPA blocked we observe phaseinsensitve vacuum fluctuations shown in trace (a). This normalized trace defines the SQL. Unblocking the OPA we record trace (b) demonstrating the phasesensitive redistribution of noise in the squeezed vacuum state. The solid curve is a fixed paramter fit to theory (4.14).

During the 0.4 second sampling we drive the PZT-mirror (M15) with a linear voltage ramp. The corresponding change in local oscillator phase θ demonstrates the phase-sensitive fluctuations and for certain directions in phase space the noise reduction beyond the SQL verifies the squeezed nature of the OPA-state. The solid curve in Fig.4.6 is a logaritmic plot of the normalized spectrum Eq.(3.22)

$$\Phi_i(\omega,\theta) = 1 + \Phi_Q(\omega,\theta) = 1 + 2\bar{\eta}\left[s(\omega) + c(\omega)\cos(2\theta)\right] \tag{4.14}$$

All parameters in this plot are fixed by independent measurements and collected for reference in the following table :

$\epsilon = (P_\beta/P_\beta^{th})^{1/2}$	OPA pump parameter	0.62
$\Omega = \omega/\gamma$	Reduced RF frequency	0.27
$\eta = \kappa/\gamma$	OPA escape efficiency	0.847
T_p	Propagation efficiency	0.98
ξ	Homodyne visibility	$(0.965)^2$
α	Detector quantum efficiency	0.98
$\bar{\eta} = \eta T_p \xi^2 \alpha$	effective escape efficiency	0.76±0.02

Theory predicts that we should see -5.2±0.3 dB of squeezing with these parameters. By averaging several traces like Fig.4.6 the corresponding experimental squeezing is found to be -4.5±0.1 dB. It is worth noting that the small video bandwidth (VBW=30 Hz) in this measurement is likely to cause an artificial correlation among datapoints which could explain why the experimental trace does not "reach" the theoretical curve at the extreme points. But the measured vacuum noise reduction is acceptable for the experimental observation of frequency nondegenerate quadrature correlations produced inside the OPA. This is the subject of Chapters 5 and 6.

4.4 Summary

In this Chapter we describe in detail the design and operation of our OPA cavity. The choice of cavity dimension ($FSR = \Delta = 370$ MHz), coupler transmission ($T_1 = 12.2\%$), and nonlinear crystal ($KNbO_3$) is largely based on (i) the NOPA experiment (Chapter 5,6) where we need relatively small FSR, and (ii) the atomic backaction experiments (Chapter 7) for which we need tunability and relatively large bandwidth. As observed in previous squeezing experiments a major limitation with $KNbO_3$ is the blue light induced infrared absorption L_B(BLIIRA) which reduces the cavity escape efficiency η, and the pump parameter ϵ for a fixed pump power P_β. We measure $L_B(P_\beta)$ and calculate $\eta(P_\beta)$ for fixed ϵ. The result shown in Fig.4.2b reveals that we only gain marginally by using a pump power above 100 mW. This pump is produced in a external doubling cavity (similar to the OPA cavity) which is typically operated with 500 mW fundamental power, giving out 275 mW at the second harmonic.

We have used our setup to observe 4.5±0.1 dB vacuum squeezing which is comparable to the theoretical level when including the effective escape efficiency $\bar{\eta} = 0.76$, the finite (scaled) observation frequency $\Omega = 0.27$, and pump parameter $\epsilon = 0.62$.

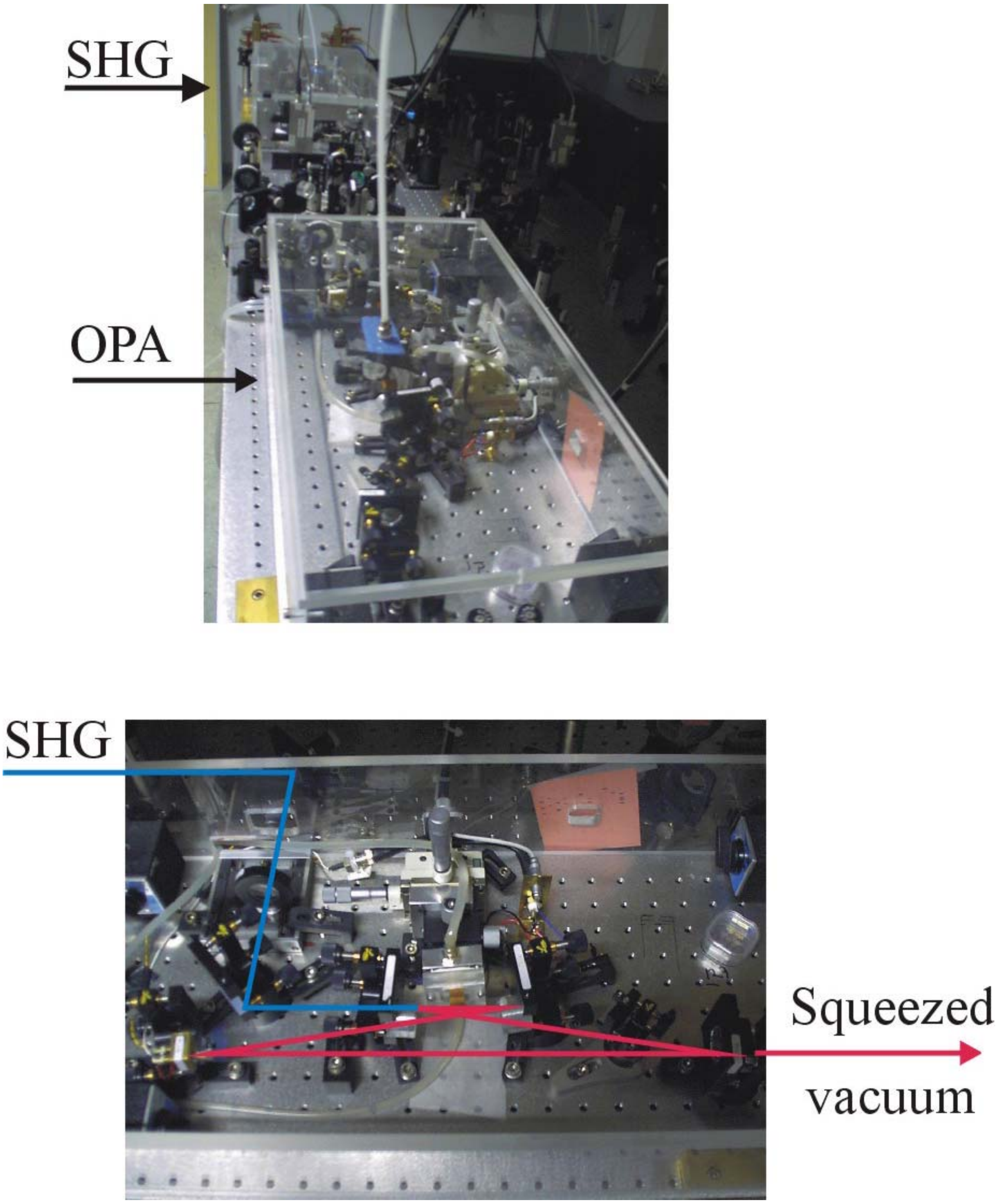

Figure 4.7: Pictures from the laboratory. Top : SHG- and OPA cavity (compare Fig.4.5). Buttom : close-up of the OPA cavity (compare Fig.4.1). False color code: blue=430nm and red=860nm.

Chapter 5

The Nondegenerate Optical Parametric Amplifier

5.1 Two mode squeezing and the Wigner distribution

In this section we introduce the concept of two mode squeezing. The idea is to establish a simple phase space picture by which we can predict the main features of two coupled harmonic oscillators of frequencies ω_1 and ω_2. The dynamic evolution of this system is described in an interaction picture with respect to ω_1 and ω_2 such that the phase space distribution only changes due to the coupling. The observables which completely describe this system are the dimensionless position (momentum) of each oscillator x_j (y_j) satisfying the canonical commutation relations $[\hat{x}_i, \hat{y}_j] = i\delta_{ij}$ and $[\hat{x}_i, \hat{x}_j] = [\hat{y}_i, \hat{y}_j] = 0$ with $j = 1, 2$. For each oscillator we also define the non-hermitian step operator $\hat{a}_j = 2^{-1/2}(\hat{x}_j + i\hat{y}_j)$. The coupling is through the simultaneous excitation/de-excitation of each oscillator by energy exchange with a classical mode with constant excitation β

$$\hat{V} = i\hbar g(\beta \hat{a}_1^\dagger \hat{a}_2^\dagger - \beta^* \hat{a}_1 \hat{a}_2) \tag{5.1}$$

The Heisenberg equation for $\hat{a}_j$ combined with the constancy of the equal time commutator $[\hat{a}_i(t), \hat{a}_j^\dagger(t)] = \delta_{ij}$ lead to the Bogoliubov transformation (compare to Chapter 3)

$$\hat{a}_j^{(out)} = \mu \hat{a}_j^{(in)} + \nu \hat{a}_k^{(in)\dagger} \tag{5.2}$$

Here $\mu = \sinh(r)$ and $\nu = \cosh(r)$ with $r = g\beta t$ and $j \neq k$. The corresponding position and momentum for each oscillator are coupled like

$$\begin{aligned} \hat{x}_j^{(out)} &= \mu \hat{x}_j^{(in)} + \nu \hat{x}_k^{(in)} && (5.3) \\ \hat{y}_j^{(out)} &= \mu \hat{y}_j^{(in)} - \nu \hat{y}_k^{(in)} && (5.4) \end{aligned}$$

Introducing the normal coordinates $\hat{x}_\pm = 2^{-1/2}(\hat{x}_1 \pm \hat{x}_2)$ and $\hat{y}_\pm = 2^{-1/2}(\hat{y}_1 \pm \hat{y}_2)$ these equations separate into

$$\begin{aligned} \hat{x}_\pm^{(out)} &= (\mu \pm \nu)\hat{x}_\pm^{(in)} = e^{\pm r}\hat{x}_\pm^{(in)} \Rightarrow \langle \hat{x}_\pm^{(out)}, \hat{x}_\pm^{(out)} \rangle = (\mu \pm \nu)^2 \langle \hat{x}_\pm^{(in)}, \hat{x}_\pm^{(in)} \rangle && (5.5) \\ \hat{y}_\pm^{(out)} &= (\mu \mp \nu)\hat{y}_\pm^{(in)} = e^{\mp r}\hat{y}_\pm^{(in)} \Rightarrow \langle \hat{y}_\pm^{(out)}, \hat{y}_\pm^{(out)} \rangle = (\mu \mp \nu)^2 \langle \hat{y}_\pm^{(in)}, \hat{y}_\pm^{(in)} \rangle && (5.6) \end{aligned}$$

Here we recognize the familiar phase sensitive amplification/de-amplification but now the squeezing is in the normal coordinates $\hat{x}_-$ and $\hat{y}_+$ which justify the term two mode squeezing. This is our main result. The experimental broadband generalization follows again from the replacement scheme in

Eq.(3.5) and the reader familiar with two-mode squeezing can in principle jump to the experimental discussion in Chapter 6.

The Wigner distribution is very useful to picture the correlations between the coupled modes. We assume that both oscillators are initially uncoupled and in the groundstate $|0\rangle_1 |0\rangle_2 = |0\rangle_+ |0\rangle_- \equiv |0\rangle$. The Wigner distribution for this vacuum state is the symmetric Gaussian state introduced in Chapter 2 (see Fig.5.1a)

$$\begin{aligned} W^{(in)}(x_-, y_-, x_+, y_+) &= \langle 0|\, \hat{\Pi}(x_-, y_-)\hat{\Pi}(x_+, y_+)\, |0\rangle = W^{(in)}(x_-, y_-)W^{(in)}(x_+, y_+) && (5.7) \\ W^{(in)}(x, y) &= \frac{1}{\pi} e^{-(x^2+y^2)} && (5.8) \end{aligned}$$

The displacement operator $\hat{D}(x_\mp, y_\mp)$ changes according to Eq.(5.5),(5.6) into $\hat{U}^\dagger \hat{D}(x_\mp, y_\mp)\hat{U} = \hat{D}(e^{\pm r}x_\mp, e^{\mp r}y_\mp)$ where $\hat{U} = \exp(-i\hat{V}t/\hbar)$ is the time evolution operator in the interaction picture. The displaced parity operator therefore takes the new form $\hat{U}^\dagger(t)\hat{\Pi}(x_\mp, y_\mp)\hat{U}(t) = \hat{\Pi}(e^{\pm r}x_\mp, e^{\mp r}y_\mp)$ and the Wigner distribution for the coupled oscillators becomes

$$W^{(out)}(x_-, y_-, x_+, y_+) = \langle 0|\, \hat{\Pi}(e^r x_-, e^{-r}y_-)\hat{\Pi}(e^{-r}x_+, e^r y_+)\, |0\rangle = W^{(in)}(e^r x_-, e^{-r}y_-)W^{(in)}(e^{-r}x_+, e^r y_+) \tag{5.9}$$

Because of the separation in normal coordinates we can easily plot the phase space distribution as shown in Fig.5.1b. This simple picture displays the essential correlation between the two coupled oscillators. It is instructive to rewrite Eq.5.9 in the form

$$W^{(out)}(x_-, y_-, x_+, y_+) = W^{(in)}(e^r x_-, e^r y_+)W^{(in)}(e^{-r}x_+, e^{-r}y_-) \tag{5.10}$$

This suggest to "split up" phase space as shown in Fig.5.1c, which again clearly demonstrates the strong correlation in terms of the narrow peak in x_- and y_+. Note that this plot is not a true phase space plot since operators describing orthogonal axes commute, i.e. $[\hat{x}_\mp, \hat{y}_\pm] = 0$. But it does show the large spread along x_+ and y_- and accordingly the excitation of each individual oscillator must be very high. It is therefore natural to ask about the quadrature distribution of a single oscillator $W(x_1, y_1)$ which we find by integrating $W^{(out)}$ over the unobserved quadratures x_2 and y_2. Since we keep x_1 and y_1 fixed we might as well integrate out x_- and y_+ which leads to the following result

$$W^{(th)}(x_1, y_1) = \int d\eta_1 d\eta_2 W^{(in)}(e^r\eta_1, e^r\eta_2)W^{(in)}(e^{-r}(2^{1/2}x_1 - \eta_1), e^{-r}(2^{1/2}y_1 - \eta_2)) \tag{5.11}$$

Thus the quadrature distribution for a single oscillator is obtained by folding the narrow and broad peak shown in Fig.5.1c. The result which is dominated by the broad peak is exactly the Wigner distribution of the thermal state

$$W^{(th)}(x_j, y_j) = \frac{1}{\pi\cosh(2r)} e^{-(x_j^2+y_j^2)/\cosh(2r)} \tag{5.12}$$

Here $\cosh(2r) = 1 + 2\bar{n}$ where $\bar{n} = \sinh^2(r)$ is the mean number of pair excitations created during the interaction time.

The discussion so far has stressed the role of the normal coordinates $x_\pm$ and $y_\pm$. In fact there is a simple symmetry in the coupling $\hat{V}$: the substitution $\hat{a}_1 \to \hat{a}_1 e^{-i\varphi}$ and $\hat{a}_2 \to \hat{a}_2 e^{i\varphi}$ with an arbitrary phase φ leaves $\hat{V}$ invariant and naturally leads to the definition of a generalized quadrature observable $q_j(\varphi)$ for each oscillator

$$\hat{q}_j(\varphi) = 2^{-1/2}(\hat{a}_j e^{-i\varphi} + \hat{a}_j^\dagger e^{i\varphi}) = \hat{x}_j \cos(\varphi) + \hat{y}_j \sin(\varphi) \tag{5.13}$$

All calculations, results and graphs for $x_\pm$ and $y_\pm$ can be repeated with the replacement

$$\begin{aligned} \hat{x}_1 &\to \hat{q}_1(\varphi), \quad \hat{x}_2 \to \hat{q}_2(-\varphi), \quad \hat{y}_1 \to \hat{q}_1(\varphi + \pi/2), \quad \hat{y}_2 \to \hat{q}_2(-\varphi + \pi/2) && (5.14) \\ \hat{x}_\pm &\to \hat{q}_\pm(\varphi) = \hat{q}_1(\varphi) \pm \hat{q}_2(-\varphi), \quad \hat{y}_\pm \to \hat{q}_\pm(\varphi + \pi/2) = \hat{q}_1(\varphi + \pi/2) \pm \hat{q}_2(-\varphi + \pi/2) && (5.15) \end{aligned}$$

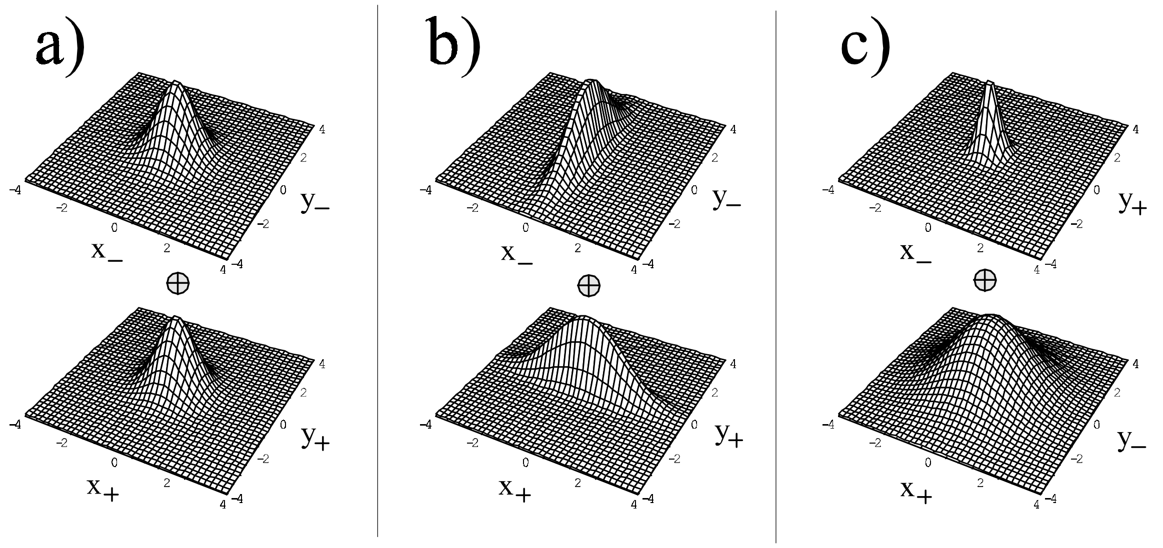

Figure 5.1: a) Gaussian Wigner distribution for two uncorrelated oscillators in the groundstate. b) Correlated excitation of the two oscillators reduce the quantum fluctuations in joint observables x_- and y_+. c) Same as (b) but with axes interchanged. The (unphysical) limit of this plot corresponds to EPR co-eigenstate of x_- and y_+ as discussed in Chapter 6.

It is therefore apparent that the fluctuation of an arbitrary quadrature observable $q_1(\varphi)$ of one oscillator is strongly correlated with the fluctuation of $q_2(-\varphi)$ for the other oscillator. More generally the above substitution scheme tells us that the noise measured in the observable $q_1(\varphi_1) - q_2(\varphi_2)$ should *only* depend on the phase sum $\theta = \varphi_1 + \varphi_2$. In this section we have discussed the coupling between arbitrary oscillators. The nondegenerate OPA or NOPA realizes this coupling between two modes of the electromagnetic field and in the following section we derive the observable fluctuation spectrum from this system.

5.2 Two mode squeezing in the NOPA

The NOPA plus homodyne detection setup is shown for reference in Fig.5.2. The integer $j = 1, 2$ denotes two frequency nondegenerate modes selected by (i) energy conservation $\omega_1 + \omega_2 = \omega_b$ and (ii) the cavity resonance condition $\omega_{1,2} = \omega_b/2 \pm m\Delta$. Here ω_b is the pump frequency, m is an integer and $\Delta = c/l$ is the free spectral range of the NOPA cavity with optical length l. The degenerate operation $m = 0$ has been discussed in the last two chapters. Here we focus on the nondegenerate operation $m \neq 0$ where m is limited only by the condition that $\omega_{1,2}$ satisfy the relative broadband phasematching condition $n_1\omega_1 + n_2\omega_2 = n_b\omega_b$. The modestructure for $m = 0, 1$ is also displayed in Fig.5.2 (see inset). We now follow closely the notation and systematic approach introduced in chapter 3 and adapted from [34]. First the NOPA intracavity spectrum is defined and calculated using the drift- and diffusion matrix of the linearized Fokker-Planck equation. Then boundary conditions on the NOPA coupling mirror M1 are used to project the cavity fluctuations onto the external field $\hat{E}_j^{(out)}$. Any external propagation loss including homodyne- and quantum efficiency is described by the transmission T_j which determines the amount of the vacuum state $\hat{V}_j$ introduced by an auxiliary beamsplitter. The quadratures of the final field $\hat{E}_j$ are recorded by separate balanced homodyne

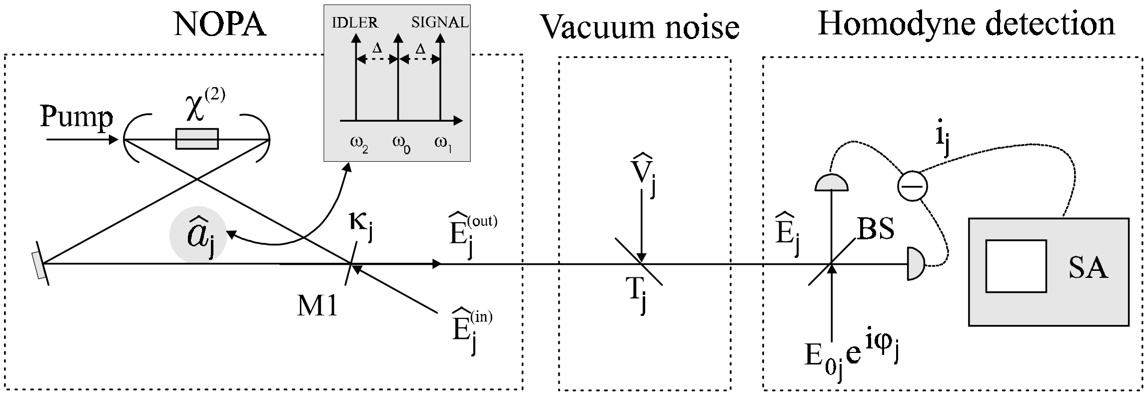

Figure 5.2: Setup and notation used to derive the NOPA spectrum. Signal and idler field ($j = 1, 2$) are separated in frequency by two longitudinal cavity modes $2\Delta = 740$ MHz (see inset). Not shown is the filter cavity used to *spatially* separate the signal and idler (see Chapter 6).

detectors[1].

The signal mode ω_1 and idler mode ω_2 are coupled by three-wave mixing, i.e. spontanous parametric downconversion from the pump mode ω_b

$$\hat{V} = i\hbar g(\hat{b}\hat{a}_1^\dagger\hat{a}_2^\dagger - \hat{b}^\dagger\hat{a}_1\hat{a}_2) \tag{5.16}$$

Here we are working in an interaction picture with respect to both ω_1 and ω_2. As described in Chapter 3 the coupling strength g is proportional to the effective nonlinear constant d_{nl} of the crystal[26]. By replacing the pump mode annihilation operator $\hat{b}$ by the a constant classical excitation β (see Eq.(5.1)) we linearize the coupled equations for the signal and idler modes. The master equation for the NOPA is described by the coherent coupling in Eq.(5.16) plus signal and idler amplitude decay to (independent) vacuum reservoirs at rates $\gamma_{1,2}$

$$\frac{\partial}{\partial t}\hat{\rho} = \frac{1}{i\hbar}[\hat{V}, \hat{\rho}] + \sum_j \gamma_j(2\hat{a}_j\hat{\rho}\hat{a}_j^\dagger - \hat{a}_j^\dagger\hat{a}_j\hat{\rho} - \hat{\rho}\hat{a}_j^\dagger\hat{a}_j) \tag{5.17}$$

We are going to use this equation to compute the second order spectra defined as

$$s_{ij}(\omega) = 2(\gamma_i\gamma_j)^{1/2}\mathcal{F}\{\langle : \hat{a}_i^\dagger(0), \hat{a}_j(\tau) :\rangle\}, \;\; c_{ij}(\omega) = 2(\gamma_i\gamma_j)^{1/2}\mathcal{F}\{\langle : \hat{a}_i(0), \hat{a}_j(\tau) :\rangle\} \tag{5.18}$$

Again the symbols (::) indicate time- and normal ordering of operators and $\mathcal{F}$ denotes the Fourier transform with respect to τ. The normally ordered spectra are evaluated through the P-distribution used in the coherent state expansion of the density operator (see Eq.(3.9)). The operator rules in Eq.(3.10) are unchanged but we have to put an index on the coherent amplitude, i.e. $\alpha \to \alpha_j$, to account for the two modes of the NOPA. Substituting the coherent state expansion and the operator rules into Eq.(5.17) we transform the NOPA master equation into the equivalent Fokker-Planck equation

$$\frac{\partial}{\partial t}P(\mathbf{x}) = \sum_{i,j}\left[\frac{\partial}{\partial x_i}\mathbf{A}_{ij}x_j + \frac{1}{2}\frac{\partial^2}{\partial x_i \partial x_j}\mathbf{D}_{ij}\right]P(\mathbf{x}) \tag{5.19}$$

---

[1] The spatial separation of the signal and idler as well as the frequency shifting of the LO by ±Δ from degeneracy is described in the next chapter.

where we have introduced the vector $\mathbf{x} = (\alpha_1, \alpha_2^\star, \alpha_2, \alpha_1^\star)$ and the drift- and diffusion matrix

$$\mathbf{A} = \begin{bmatrix} \gamma_1 & -g\beta & 0 & 0 \\ -g\beta & \gamma_2 & 0 & 0 \\ 0 & 0 & \gamma_2 & -g\beta \\ 0 & 0 & -g\beta & \gamma_1 \end{bmatrix}, \quad \mathbf{D} = \begin{bmatrix} 0 & 0 & g\beta & 0 \\ 0 & 0 & 0 & g\beta \\ g\beta & 0 & 0 & 0 \\ 0 & g\beta & 0 & 0 \end{bmatrix} \tag{5.20}$$

As discussed in Chapter 3 the Fokker-Planck equation for the Glauber-Sudarshan P-distribution is ill-defined for nonclassical states of the field, but we resolve this problem by going to the *positive* P-distribution. This change amounts to replacing $\alpha_1^\star$ ($\alpha_2^\star$) in the vector $\mathbf{x}$ with the independent complex variable $\alpha_1^\dagger$ ($\alpha_2^\dagger$). The Fokker-Planck equation is left unchanged and since $\mathbf{A}$ and $\mathbf{D}$ are constant, i.e. β is constant, we can replace Eq.(5.19) with the equivalent set of classical stochastic differential equations[35]

$$\dot{\mathbf{x}} = -\mathbf{A}\mathbf{x} + \mathbf{B}\boldsymbol{\eta} \tag{5.21}$$

Here $\mathbf{B}\mathbf{B}^\mathbf{T} = \mathbf{D}$ and the vector $\boldsymbol{\eta}$ has zero mean and correlation $\langle \eta_i(t), \eta_j(t') \rangle = \delta_{ij}\delta(t-t')$. As proven in Appendix B we can define a noisematrix $\mathbf{N}(\omega)$ which is simply related to the drift- and diffusion matrix of the Fokker-Planck equation according to

$$\mathbf{N}(\omega) = \mathcal{F}\left\{\langle \mathbf{x}(0), \mathbf{x}^\mathbf{T}(\tau)\rangle\right\} = (\mathbf{A} - i\omega\mathbf{I})^{-1}\mathbf{D}(\mathbf{A}^\mathbf{T} + i\omega\mathbf{I})^{-1} \tag{5.22}$$

Here $\mathbf{I}$ is the identity matrix and the classical correlation is directly related to the quantum analogue by the P-distribution substitution scheme

$$\hat{a}_j \Leftrightarrow \alpha_j, \quad \hat{a}_j^\dagger \Leftrightarrow \alpha_j^\dagger \tag{5.23}$$

Direct comparison between Eq.(5.22) and Eq.(5.18) identify $s_{ij}(\omega)$ and $c_{ij}(\omega)$ as the matrix elements of $\mathbf{N}(\omega)$ and the resulting intracavity spectra follow by the simple matrix inversion in Eq.(5.22). The result is

$$\begin{aligned} s_{12}(\omega) &= s_{21}(\omega) = c_{11}(\omega) = c_{22}(\omega) = 0 && (5.24) \\ s(\omega) &= s_{11}(\omega) = s_{22}(\omega) = 4\epsilon^2/M_+M_- && (5.25) \\ c(\omega) &= c_{12}(\omega) = c_{21}^\star(\omega) = 2\epsilon(1+\epsilon^2+\Omega^2-2i\Lambda_-\Omega)/M_+M_- && (5.26) \end{aligned}$$

where now $M_\pm = \left[(\Lambda_+ \pm E)^2 + \Omega^2\right]$ and we have introduced a number of scaled parameters : the reduced frequency $\Omega = \omega/(\gamma_1\gamma_2)^{1/2}$; the reduced pump $\epsilon = g\beta/(\gamma_1\gamma_2)^{1/2}$; the cavity decay asymmetry $\rho = (\gamma_1/\gamma_2)^{1/2}$; the NOPA effective pump $E = (\epsilon^2 + \Lambda_+^2 - 1)^{1/2}$ and the decay asymmetry functions $\Lambda_\pm = (\rho \pm \rho^{-1})/2$. Note that in the case of symmetric signal and idler decay ($\rho = \Lambda_+ = 1$ and $\Lambda_- = 0$) the spectra in Eq.(5.25,5.26) reduce to the spectra calculated in Chapter 3 (see Eq.(3.16)). But since $c_{11} = c_{22} = 0$ there is no phase dependence in the in the individual signal and idler spectra. Since experimental data are collected outside the NOPA cavity we introduce the boundary conditions on the cavity coupler M1 (Fig.5.1)

$$\hat{E}_j^{(out)}(t) + \hat{E}_j^{(in)}(t) = (2\kappa_j)^{1/2}\hat{a}_j(t) \tag{5.27}$$

Here κ_j is the amplitude decay rate of the signal/idler through the coupler M1. The output field $\hat{E}_j^{(out)}$ is mixed with the vacuum field $\hat{V}_j$ on the beamsplitter with transmission T_j

$$\hat{E}_j = (1-T_j)^{1/2}\hat{V}_j + T_j^{1/2}E_j^{(out)} \tag{5.28}$$

As in Chapter 3 we extend the definition of the intracavity spectra in Eq.(5.18) to the detected field $\hat{E}_j$

$$S_{ij}(\omega) = \mathcal{F}\{\langle : \hat{E}_i^\dagger(0), \hat{E}_j(\tau) : \rangle\}, \quad C_{ij}(\omega) = \mathcal{F}\{\langle : \hat{E}_i(0), \hat{E}_j(\tau) : \rangle\} \tag{5.29}$$

Next the combination of Eq.(5.29),(5.28),(5.27) and (5.18) allow us to express the external correlations in terms of cavity correlations

$$S_{ij}(\omega) = (\bar{\eta}_i\bar{\eta}_j)^{1/2} s_{ij}(\omega), \;\; C_{ij}(\omega) = (\bar{\eta}_i\bar{\eta}_j)^{1/2} c_{ij}(\omega) \tag{5.30}$$

Here we have again used the generalized escape efficiency $\bar{\eta}_j$ as the probability for a cavity signal- or idler photon to generate a photoelectron in the homodyne detector. It is the product of the cavity escape efficiency and beamsplitter transmission T_j for mode j, i.e. $\bar{\eta}_j = \eta_j T_j$. In the balanced homodyne detection setup the field $\hat{E}_j$ is overlapped with phase-coherent and resonant local oscillator field $\langle \hat{E}_j^{(lo)} \rangle = E_{j0} e^{i\varphi_j}$ and the resulting balanced detector current $i_j(t)$ is probing the field quadrature

$$\hat{Q}^{(j)}_{\varphi_j}(t) = \hat{E}_j(t) e^{-i\varphi_j} + \hat{E}_j(t) e^{i\varphi_j} \tag{5.31}$$

By this argument the combined current $i(t) = \cos(\psi) i_1(t) - \sin(\psi) i_2(t)$ is probing the combined field quadrature

$$\hat{Q}^{(-)}_{\theta,\psi}(t) = \cos(\psi)\hat{Q}^{(1)}_{\varphi_1}(t) - \sin(\psi)\hat{Q}^{(2)}_{\varphi_2}(t), \tag{5.32}$$

where we have defined $\theta = \varphi_1 + \varphi_2$ and the mixing angle ψ. The spectral density of photocurrent fluctuations $\Phi_i(\omega, \theta, \psi) = \mathcal{F}\{\langle i(0), i(\tau) \rangle\}$ is therefore linked to the spectral density of field fluctuations $\Phi_Q(\omega, \theta, \psi) = \mathcal{F}\{\langle : \hat{Q}^{(-)}_{\theta,\psi}(0), \hat{Q}^{(-)}_{\theta,\psi}(\tau) : \rangle\}$ by the simple result (Appendix B)

$$\Phi_i(\omega, \theta, \psi) = 1 + \Phi_Q(\omega, \theta, \psi) \tag{5.33}$$

Here "$1 = \cos^2(\psi) + \sin^2(\psi)$" defines the standard quantum limit (SQL) for uncorrelated vacuum fluctuations in the signal and idler mode. For specific mixing angles ψ and phase sums θ these fluctuations are correlated/anticorrelated by the OPA as expressed through the negative/positive value of the normally ordered spectrum Φ_Q . This spectrum is easily calculated using the quadrature definition Eq.(5.31) and the spectra in Eq.(5.30)[2]

$$\Phi_Q(\omega, \theta, \psi) = 2\eta \left[s(\omega)[\sigma \cos^2(\psi) + \sigma^{-1} \sin^2(\psi)] - c(\omega) \sin(2\psi) \cos(\theta) \right] \tag{5.34}$$

We have introduced the new combination of scaled parameters $\eta = (\bar{\eta}_1\bar{\eta}_2)^{1/2}$ and $\sigma = (\bar{\eta}_1/\bar{\eta}_2)^{1/2}$. When $\psi = 0$ ($\pi/2$) we observe the signal (idler) mode alone with phase-independent excess noise generated in the NOPA (thermal state). In the case of complete symmetry between the signal and idler ($\rho = \sigma = 1$) we recover the squeezing result in Eq.(3.21) when choosing the symmetric mixing angle $\psi = \pi/4$.

In a realistic experiment we will not have complete symmetry and it is therefore relevant to develop an optimized measurement strategy for this situation. We expect that asymmetry between signal and idler ($\rho, \sigma \neq 1$) can to some extend be compensated by measuring a corresponding "asymmetric" quadrature combination, i.e. $\psi \neq \pi/4$. The experimental approach is to minimize the electronic fluctuations $\Phi_i(\omega, \theta, \psi)$ by varying the relative gain, i.e. the mixing angle ψ, between the homodyne detectors. Theoretically we get the optimal value ψ_0 from the extremum in Eq.(5.34) with $\theta = 0$

$$\tan(2\psi_0) = \frac{c}{s\delta_-} \tag{5.35}$$

Using the derived parameters $\delta_\pm = (\sigma^{-1} \pm \sigma)/2$ we substitute this result back into Eq.(5.34) to obtain the closed expression

$$\Phi_Q(\omega, \theta, \psi_0) = 2\eta \left[s\delta_+ + \left[(s\delta_-)^2 + c^2 \right]^{1/2} \right] \tag{5.36}$$

To illustrate the importance of choosing the optimal quadrature combination we show in Fig.5.3a the spectrum $\Phi_Q(\omega, 0, \pi/4)$ for increasing asymmetry between the signal and idler. In this case the

---

[2] It turns out that we get rid of the complex part of $c(\omega)$ and henceforth we implicitly understand $c(\omega) = \mathrm{Re}\,[c(\omega)]$.

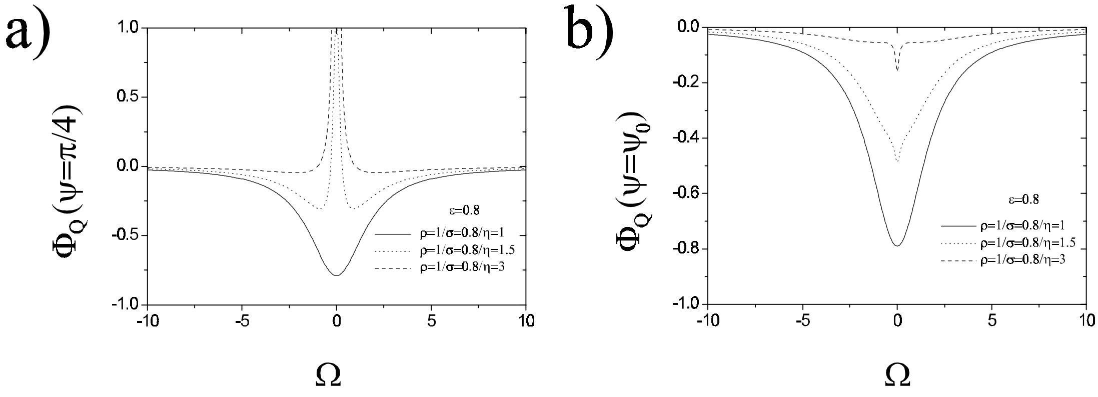

Figure 5.3: a) Spectrum of fluctuations when comparing equally weighed signal and idler quadratures ($\psi = \pi/4$). Increased cavity loss in the signal mode ($\rho = (\gamma_1/\gamma_2)^{1/2} > 1$) washes out correlations in this observable. b) Same as (a) but now with optimized mixing angle ($\psi = \psi_0$). The increased signal loss is compensated and correlations are partially restored.

total cavity decay rate for the signal γ_1 is increased while keeping all other parameters fixed. At low frequencies a noise spike appears and the correlations between signal and idler a virtually lost for $\rho = 3$. As ρ increases from 1 the parameter δ_- changes from zero to a positive value and the optimal mixing angle ψ_0 is shifted from the symmetric value $\pi/4$ towards 0. In this way the signal quadrature is given more weight to compensate the increased loss, see Eq.(5.32). In Fig.5.3b we display the optimized spectrum $\Phi_Q(\omega, 0, \psi_0)$ which shows how we recover the signal-idler correlations by choosing the optimal mixing angle ψ_0. Naturally the reduction in effective escape efficiency η as γ_1 grows will reduce the overall degree of correlations thus bringing the detected NOPA state closer to the vacuum for which $\Phi_Q = 0$.

To briefly summarize, we have calculated the experimentally observable photocurrent fluctuation spectrum resulting from the measurement of arbitrary quadrature combinations of the signal and idler emerging from the NOPA. The main result is the electronic spectrum Eq.(5.33) and its link to the optical spectrum Eq.(5.34). We also found that asymmetry between the signal and idler must be compensated by choosing an optimal mixing angle in the measured quadrature combination. In the next Chapter we use these results to compare the data from the NOPA experiment with theory.

Chapter 6

NOPA Experiment

6.1 Introduction

Historically the Wigner distribution shown in Fig.5.2b,c was first discussed in the now famous 1935 paper by Einstein, Podolsky and Rosen (EPR)[8]. The continuous spectrum of the position- and momentum observables of the two correlated particles considered in this paper are equivalent to the continuous quadrature spectrum of the NOPA[9]. In fact the state analyzed by Einstein et. al. is the limit of Fig.5.2c, i.e. $W(x_-, y_-, x_+, y_+) \rightarrow \delta(x_-)\delta(y_+)$. Since x_- and y_+ are very quiet (within the bandwidth of the NOPA) we can measure the conjugate pair x_1, y_1 of one oscillator and introduce conditional squeezing in *both* of the conjugate observables x_2, y_2 of the second oscillator. This is in apparent violation of the Heisenberg uncertainty principle and was used by EPR to argue that quantum mechanics is an incomplete theory. But clearly the uncertainty principle does not apply in the case of conditional variances as several experiments have since shown.

The first experiment in this series used type II downconversion in KTP to operate a polarization NOPA[51],[33]. This experiment realizes the Bogoliubov transformation in Eq.(5.3),(5.4) with index $j, k = 1, 2$ denoting two orthogonal polarized optical modes. Clearly these coupled EPR transformations can be separated into uncoupled squeezing transformations (Eq.(3.3),(3.4)) by a 45 degree polarization rotation. Indeed the reverse process (mixing two squeezed modes) was used in the next realization of the EPR state which was applied for continuous variable quantum teleportation[52]. In this experiment the two squeezed beams are distinguished not by their polarization, but by their spatial modes emerging from a single OPA pumped from two directions. Following this work other groups have employed the same technique with different modifications. In Ref.[53] the two initial squeezed modes where realized in a Kerr PM-fiber interferometer excited by a pulsed pump. Recently the group of H.-A. Bachor improved the original teleportation experiment using overlapped squeezed modes from two independent semi-monolithic OPA's[54]. Similarly the Caltech group have repeated the original teleportation experiment with improved fidelity[55]. The continuous variable EPR state has also been realized, for the first time, between the transverse spin components of two macroscopic spins each representing roughly 10^{12} cesium atoms in a glass cell[44]. As opposed to the deterministic generation in previous experiments this EPR state was prepared by nonlocal Bell-measurements of x_+ and y_- , i.e. a measurement induced "collapse" onto the generic Wigner state shown in Fig.5.2c.

In this Chapter we present experimental results demonstrating the EPR state between two optical modes (signal/idler) which, as opposed to previous experiments, are separated in frequency by twice the free spectral range of the OPA (740 MHz)[56]. The two modes are correlated by the same type I downconversion in $KNbO_3$ responsible for the quadrature squeezing observed in Chapter 4. Thus the experimental setup involves only minor extensions of the OPA design which are described in section 6.2. In section 6.3 we present the measured signal/idler correlation, i.e. we compare the noise in $x_\pm$ and $y_\pm$ against the noise from two independent vacuum modes. This comparison,

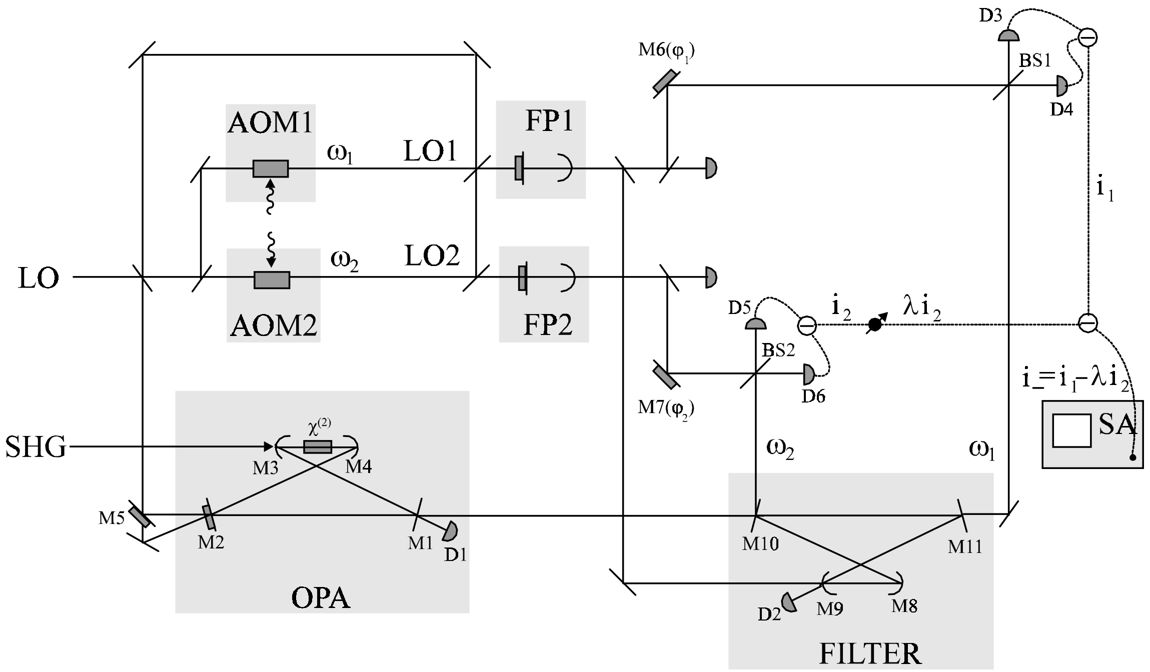

Figure 6.1: Outline of setup used in the NOPA experiment. See text for detailed explanation.

when formulated as an inseparability criterion[10], allow us to characterize our system against the previous work presented above. Inseparability or entanglement is also a key issue for applications in the emerging field of quantum information and for violating local realism, i.e. any Bell inequality formulated for a continuous variable system. We discuss these matters in a final section 6.4.

Quantum correlations have also been observed between the twin beams from a NOPA above threshold. In Ref.[57] the authors directly observe 8.5 dB noise reduction near 3 MHz in the intensity difference between the orthogonal polarized twin beams (3 mW each) from a KTP (type II) optical parametric oscillator (OPO). A semi-monolithic OPO was used in Ref.[58] to probe the $4S_{1/2}-5S_{1/2}$ transition of atomic potassium against a noise background reduced by 1.9 dB relative to the shot noise limit. In Ref.[59] twin beams with wavelength separation in the range 15-60 nm are spatially separated on a holographic diffraction grating. Below we also discuss the spatial separation of signal and idler mode using a moderate finesse filter cavity since no diffraction grating can resolve 740 MHz.

6.2 NOPA setup

The NOPA experimental configuration is shown for reference in Fig.6.1. We recycle essentially all components from the OPA setup. The central new element is the folded ring filter cavity constructed from to curved (ROC=5 cm) highreflecting mirrors (M8,M9) and two plane coupling mirrors (M10,M11) with transmission $T_f = 0.078$[1]. The cavity length is $l_f = 20$ cm with a corresponding free spectral range (FSR) $\Delta_f = c/l_f = 1.5$ GHz, quality factor $Q_f = \pi/T_f = 40$, and bandwidth $2\gamma_f = 37.5$ MHz (FWHM). The filter action of this cavity is identical to that of a mirror with high transmission (reflection) for the signal (idler) at frequency $\omega_1 = \omega_0 + \Delta$ ($\omega_2 = \omega_0 - \Delta$). Here ω_0 is the degenerate OPA frequency and $\Delta = 370$ MHz is the FSR of the OPA cavity (see Fig.5.2). In the experiment we lock the filter cavity length to the the frequency ω_1 of the local oscillator LO1 by injecting part of

---

[1] Subscript f is used to label properties of the filter cavity.

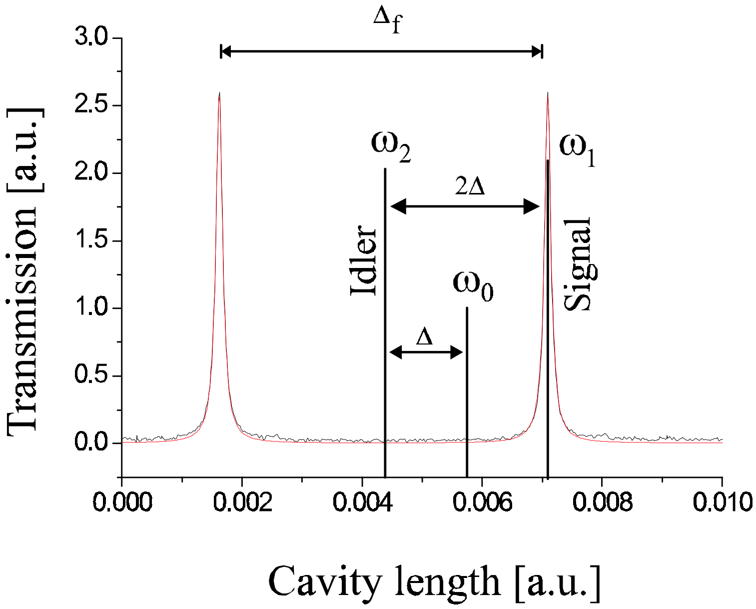

Figure 6.2: Filter cavity transmission versus cavity length. When the filter cavity is locked to LO1 the signal ω_1 is resonant ($T = 0.95$). Under these conditions the idler ω_2 is off resonance and reflected ($R = 0.98$). $\Delta_f = 1.5$ GHz is the FSR of the filter cavity; $\Delta = 370$ MHz is the FSR of the NOPA cavity. The fit is a standard Fabry-Perot transmission curve.

this field through M9. The error signal (D2) is again derived from the beatnote between the reflected carrier and FM sidebands[50] (see Chapter 4).

The LO1 frequency ω_1 is synthesized from the fundamental ω_0 by sending it through an acousto optic modulator (AOM1) in a double pass configuration. The total AOM1 frequency shift $2\delta = \omega_1 - \omega_0$ is set by a voltage controlled oscillator (VCO). The VCO is tuned to exactly half the FSR of the OPA, i.e $\delta = \Delta/2 = 185$ MHz. In the experiment this tuning is completed in two steps. First we center δ around 185 MHz by observing the VCO output directly on a spectrum analyzer. Secondly, we fine tune δ by monitoring the transmission of LO1 through the OPA. Since the OPA is locked to the fundamental ω_0 the transmission peak of LO1 appears at the signal resonance condition $\omega_1 = \omega_0 + \Delta$, i.e. $2\delta = \Delta$. The VCO oscillation frequency is stable at the level of 1 MHz over a period of several days.

When the symmetric filter cavity is locked to LO1 it operates as a high transmission narrowband filter ($2\gamma_f$) for the signal frequency ω_1. In Fig.6.2 we show the observed transmission while scanning the cavity length. Calibrated measurements show a finite transmission 0.95. The deviation from perfect signal transmission is caused by a combination of intracavity losses and a small asymmetry in the transmission of the plane couplers M10 and M11. In Fig.6.2 we mark the relative position of the signal and idler field ($\omega_{1,2} = \omega_0 \pm \Delta$). With the filter cavity locked the idler is detuned by $2\Delta = 740$ MHz and perfectly reflected ($1 - 10^{-3}$) thus separating it spatially from the signal. Again finite loss and asymmetry explain the deviation of the measured idler reflection 0.98 from unity. The degenerate mode ω_0 centered between the signal and idler is also reflected as is the case for higher order ($m > 1$) signal-idler pairs at frequencies $\omega_{1,2} = \omega_0 \pm m\Delta$ under the phasematching curve. The frequency selection between all reflected components is achieved in the homodyne mixing with the second local oscillator LO2. The frequency of LO2 is tuned to match the idler $\omega_2 = \omega_0 - \Delta$ by simply driving a second acousto optic modulator (AOM2) with the same VCO signal δ.

The local oscillator LO1 (LO2) is spatially cleaned and stabilized in FP1 (FP2) and overlapped with the signal (idler) on a 50/50 beamsplitter BS1 (BS2). The mixed modes are detected on a pair of high efficiency Silicon PIN diodes D3,D4 (D5, D6). The balanced signal current i_1 is combined with a scaled version of the idler current λi_2, i.e $i_- = i_1 - \lambda i_2$. In principle the scaling factor is $\lambda = \tan(\psi)$ where ψ is the mixing angle introduced in Eq.(5.32) but one should remember that λ is also used to balance the electronic gain between the signal and idler. The fluctuations in i_- which carry information about the correlation between the optical signal- and idler quadrature are analyzed with an RF spectrum analyzer (SA). We characterize the mode overlap on BS1 (BS2) by the fringe visibility ξ in the interference between LO1 (LO2) and a classical field in the signal (idler) mode. This classical field is derived from LO1 (LO2) and injected into the OPA via M5, and thus exactly overlapping and co-propagating the signal (idler) mode. At the same time we use the injected LO1 (LO2) to measure the propagation loss T_p between the OPA and homodyne detector for the signal (idler). In the next section we discuss the observed NOPA correlation spectrum.

6.3 NOPA Experiment

The NOPA experiment discussed in this section is carried out as a continuation of the squeezing experiment and the relevant OPA- and data acquisition parameters are identical to those presented in Chapter 4. As described above we investigate the lowest order ($m = 1$) frequency nondegenerate signal/idler pair $\omega_{1,2} = \omega_0 \pm m\Delta$. With the small separation $2\Delta = 740$ MHz the signal and idler mode have identical coupling rates ($\kappa_1 = \kappa_2$), decay rates ($\gamma_1 = \gamma_2$), and escape efficiencies ($\eta_1 = \eta_2$). They do however experience different propagation losses since they are spatially separated. The different contributions to the effective escape efficiency $\bar{\eta}_1$ ($\bar{\eta}_2$) for the signal (idler) are summarized in the following table along with the OPA pump level and scaled RF acquisition frequency.

Parameter		Signal	Idler
$\epsilon = (P_\beta/P_\beta^{th})^{1/2}$	OPA pump parameter	0.62	0.62
$\Omega = \omega/\gamma$	Reduced RF frequency	0.27	0.27
$\eta = \kappa/\gamma$	OPA escape efficiency	0.847	0.847
T_p	Propagation efficiency	0.91	0.96
ξ	Homodyne visibility	$(0.98)^2$	$(0.975)^2$
α	Detector quantum efficiency	0.98	0.98
$\bar{\eta} = \eta T_p \xi^2 \alpha$	effective escape efficiency	0.73±0.02	0.76±0.02

The SQL for the signal/idler quadrature difference signal is the shotnoise fluctuation in $i_- = i_1 - \lambda i_2$. We establish this noise level on the spectrum analyzer by blocking the NOPA output. The result is displayed as the normalized trace (a) in Fig.6.3. Inserting parameters into Eq.(5.35) we find a mixing angle $\psi_0 = 44.75°$ and thus $\lambda = \tan(\psi) = 0.99$. Since there is only a marginal difference between the signal and idler path they should be compared with equal weight. With the NOPA output blocked we now also block LO1 to obtain trace (b). This trace is roughly 3 dB below (a) corresponding to balanced signal and idler (by blocking LO2 instead of LO1 we obtain again a trace 3 dB below (a)). Next we unblock all beams except the signal and obtain trace (c) displaying the phase-insensitive excess noise in the idler thermal state (we obtain an identical trace when blocking only the idler). Finally we unblock all beams and scan the signal phase φ_1 (M6) while leaving the idler phase φ_2 (M7) drifting (φ_2 is stable over the 500 msec scan period). With these conditions we record trace (d) which is the experimental evidence of phase-sensitive correlations between signal and idler modes. For $\theta = 0, 2\pi..$ we measure an *arbitrary* realization of the quadrature combination $q_1(\varphi) - q_2(-\varphi)$ corresponding to a linear combination of x_- and y_+ which span the narrow peak in Fig.5.1c. For $\theta = \pi, 3\pi..$ we then measure the quadrature combination $q_1(\varphi) + q_2(-\varphi)$ which can be

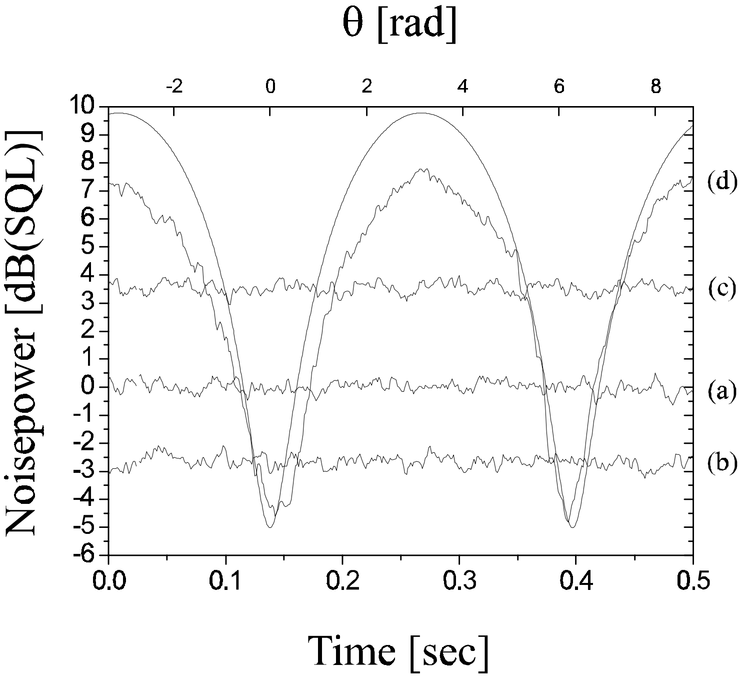

Figure 6.3: Quadrature noisepower in EPR state generated inside the NOPA. (a) Two mode SQL for uncorrelated signal and idler. (b) Single mode SQL for either signal or idler. (c) Excess thermal noise observed in the thermal state of either signal or idler. (d) Phasesensitive noise in the quadrature correlation between signal and idler. For $\theta = 0$ ($\theta = \pi$) we probe the narrow (broad) feature of the EPR Wigner distribution shown in Fig.5.1c. The solid curve is a (fixed paramter) logaritmic fit to theory. Aquisition paramters : $\omega = 1.15$ MHz, RBW=30 kHz, and VBW=30 Hz.

expressed as linear combination of the observables x_+ and y_- spanning the broad peak in Fig.5.1c. The solid curve shown in Fig.6.3 is a logaritmic plot according to theory (Eq.(5.33) and Eq.(5.34)) with $\psi_0 = 44.75°$ and all parameters fixed by the independent measurements listed in the above table.

All experimental traces have been corrected for electronic noise ($z = 0.07$ in Eq.(4.13)). We clearly see a gap between the observed and predicted antisqueezing. We believe this is partly due to a low videobandwidth (30 Hz) correlating datapoints, but this must be examined more carefully. We trust that the SQL and the observed noise reduction beyond this limit are correctly established. Next we turn to characterize our nonclassical source allowing for a comparison with related work.

6.3.1 Inseparability criterion and entanglement

The EPR state introduced Chapter 5 is characterized by a single number $r = g\beta t$ which defines the Gaussian variances $V(x_\pm)$ and $V(y_\pm)$. From several independent traces like (d) in Fig.6.3 we find the average *observed* variance $V(x_-) = V(y_+) = -3.8 \pm 0.1$ dB relative to the SQL. If we define the vacuum noise $V_0 = 1/2$ for any single oscillator quadrature observable we can write $V(x_-) = V(y_+) = 0.41(2)$. This number demonstrates that we can (at least in principle) measure the conjugate pair (x_1, y_1) and introduce *conditional squeezing* in *both* conjugate observables (x_2, y_2) in an apparent violation of Heisenberg's uncertainty relation $V(x_2 \mid x_1)V(y_2 \mid y_1) < V_0^2$. As already mentioned these conditional variances are not subject to any uncertainty relation. They simply characterize how well we have prepared a joint eigenstate of x_- and y_+. Recently it has been realized that in fact the sum $V = V(x_-) + V(x_+)$ is more suited to characterize the EPR state. V is twice the Gaussian variance of the narrow peak in Fig.5.1c and for perfectly correlated quadratures goes to zero. This is in contrast to the SQL for which $V = 2$ is the sum of the Gaussian noise from two uncorrelated oscillators shown in Fig.5.1a. The strength of the parameter V is the fact that for any two mode *separable* state

$$\rho^{(12)} = \sum_j p_j \rho_j^{(1)} \otimes \rho_j^{(2)}, \tag{6.1}$$

we always find $V \geq 2$ [10],[60]. Thus in our experiment the observation $V = 0.82(4) < 2$ allows us to conclude that we have generated an inseparable or *entangled* state which can not be reduced to the sum of products in Eq.(6.1). For comparison recent work by other groups demonstrated $V = 0.80(3)$[53] and $V = 0.88(4)$[54].

Finally, it is interesting to point out that for oscillators with Gaussian noise statistics it can shown that $V < 2$ is not only a sufficient but also *necessary* criterion for inseparability[10]. Thus any two mode state with $V \geq 2$ is separable, i.e. can be reduced to the form in Eq.(6.1). This provides a clear cut ($V = 2$) between the classical and quantum domain for continuous variables. A similar clear cut if found for bipartite systems with discrete dimensions 2x2 and 2x3 where a necessary and sufficient condition for separability is the positive partial transpose (PPT) property of the density matrix $\rho^{(12)}$[61]. For higher dimensions there exist states which are PPT but *not* separable and there is currently a lot of (theoretical) research going into discovering "clear cuts" for such states[61].

6.4 Summary and outlook

We give a description of the setup used to observe quadrature correlation or entanglement between signal and idler separated by twice the free spectral range in the NOPA cavity (740 MHz). A large part of the setup is recycled from the squeezing experiment (Chapter 4) while a central new element is the external filter cavity used to spatially separate signal and idler. From this source we are able to prepare for the first time a frequency nondegenerate EPR-state characterized by the nonlocal variance sum $V = V(x_-) + V(y_+) = 0.82(4)$ which is well below the inseparability point $V = 2$. Converting the OPA into a NOPA by simply adding a spatial filter cavity conserves properties of the squeezing source such as bandwidth and tunability (see Chapter 4). This is important for continuous variable "quantum memory" proposals which suggest to transfer the quadrature noise statistics from light to atoms either by way of coherent coupling in cavity QED[62], or by interspecies teleportation[63]. This issue is further discussed at the end of Chapter 7. Here we include a brief discussion on nonlocality and Bell's inequality for both discrete and continuous variables.

6.4.1 Nonlocality and Bell's inequality

We begin by writing down the spherically symmetric singlet state obtained when coupling two spin 1/2 angular momenta $\hat{\sigma}_1$ and $\hat{\sigma}_2$

$$|\psi\rangle_S = \frac{1}{\sqrt{2}}\left(|\uparrow\rangle_1 \otimes |\downarrow\rangle_2 - |\downarrow\rangle_1 \otimes |\uparrow\rangle_2\right) \tag{6.2}$$

This state, describing for example the helium groundstate electron configuration, was adapted by D. Bohm to discuss the EPR paradox for observables with discrete spectra, and later used by J. S. Bell to write down his celebrated inequalities[64]. We now follow closely the development in Ref.[65] and[66]. The basic experimental observable in any Bell experiment is the expectation value of the correlation operator $\hat{E}(\mathbf{a}, \mathbf{b}) = \mathbf{a} \cdot \hat{\boldsymbol{\sigma}}_1 \otimes \mathbf{b} \cdot \hat{\sigma}_2$. Here $\mathbf{a}$ and $\mathbf{b}$ are unit vectors which define the spin measurement direction on the Bloch sphere. We can now write down a (CHSH) Bell operator

$$\hat{\mathcal{B}} = \hat{E}(\mathbf{a}, \mathbf{b}) + \hat{E}(\mathbf{a}', \mathbf{b}) + \hat{E}(\mathbf{a}, \mathbf{b}') - \hat{E}(\mathbf{a}', \mathbf{b}') \tag{6.3}$$

Using basic spin 1/2 algebra it is easy to show that

$$\hat{\mathcal{B}}^2 = 4\hat{I} \otimes \hat{I} + 4\hat{E}(\mathbf{a} \times \mathbf{a}', \mathbf{b} \times \mathbf{b}'), \tag{6.4}$$

From this relation it follows that $\langle\hat{\mathcal{B}}^2\rangle \leq 4+4=8$ and thus quantum mechanics predicts the bound $|\langle\hat{\mathcal{B}}\rangle| \leq 2\sqrt{2}$. In contrast *any* local hidden variable theory predicts the bound $|\langle\hat{\mathcal{B}}\rangle| \leq 2$ which is the Bell-CHSH inequality[64]. Experiments have shown that while nature clearly violates the hidden variable bound, it nicely obeys the quantum mechanical prediction[67].

What about the original EPR state formulated for particles or fields with continuous spectra? Clearly, one would expect that the inseparability/entanglement which we experimentally demonstrate for the NOPA state can be used to violate local realism. Indeed this expectation is confirmed once we restrict ourself to dichotomic observations in each mode. One such dichotomic observable is the displaced parity operator $\hat{\Pi}(\alpha)$ whose expectation value for any state of the harmonic oscillator defines the value of the Wigner function at the (complex) point α in phase space[22] (see also Chapter 2 and 5). This observation was used in Ref.[65] to define the two mode correlation operator $\hat{E}(\alpha,\beta) = \hat{\Pi}_1(\alpha)\otimes\hat{\Pi}_2(\beta)$ for which the phase space displacement α (β) now play the role of spin direction **a** (**b**). Since $\langle\hat{E}(\alpha,\beta)\rangle = W(\alpha,\beta)$ is the two mode Wigner function the question of violating local realism with the NOPA state is reduced to the problem of finding four points in phase space such that $|\langle\hat{\mathcal{B}}\rangle| = W(\alpha,\beta)+W(\alpha',\beta)+W(\alpha,\beta')-W(\alpha',\beta') > 2$. As demonstrated in [65] this is possible for a range of squeezing parameters and phase space points.

The more recent work in Ref.[66] is based on a *perfect* analogy between continuous- and discrete variables. This is accomplished by introducing the concept of *parity spin* for a harmonic oscillators. This "pseudospin" measures parity of the oscillator state along the z-axis

$$\hat{s}_z = \sum_{n=0}^{\infty} |2n+1\rangle\langle 2n+1| - |2n\rangle\langle 2n| \tag{6.5}$$

The transverse spin components are defined by the "parity flip" operators $\hat{s}_\pm = \hat{s}_x \pm i\hat{s}_y$ which transform even oscillator states into odd ones and vice versa

$$\hat{s}_- = \sum_{n=0}^{\infty} |2n\rangle\langle 2n+1| = (\hat{s}_+)^\dagger \tag{6.6}$$

It is easy to show that the parity spin obeys the Pauli algebra and thus *all* Bell inequalities that have been derived for spin 1/2 systems can (at least in principle) be implemented with two harmonic oscillators, i.e. the NOPA modes. Now the obvious question is whether the NOPA state violates the CHSH bound. To answer this question it is useful to write down the NOPA state in a two mode Fock-basis $|n,n\rangle$ (see [35])

$$|NOPA\rangle = e^{-i\hat{V}t/\hbar}|0,0\rangle = e^{r(a_1^\dagger a_2^\dagger - a_1 a_2)}|0,0\rangle = (1-\lambda^2)^{1/2}\sum_{n=0}^{\infty}\lambda^n|n,n\rangle \tag{6.7}$$

Here $\lambda = \tanh(r)$ and $r = g\beta t$ is the squeezing parameter defined in the beginning of Chapter 5. The quantum correlations apparent in the synchronous excitation of the two oscillators are now tested against local hidden variable theories by maximizing the expectation $\langle NOPA|\hat{\mathcal{B}}|NOPA\rangle$. The result is[66]

$$\langle\hat{\mathcal{B}}\rangle_{\max} = 2\sqrt{1+\tanh(2r)} \tag{6.8}$$

Here we see that the NOPA state always violates the CHSH bound, i.e. local realism. More precisely, with any finite squeezing parameter $r > 0$ it is always possible to find directions for the parity spin which violate the Bell-CHSH inequality. But it is by no means obvious how one should implement a measurement of the parity spin although there are proposals for measuring arbitrary motional observables for a trapped ion[68]. In that respect the idea of displaced parity observations has a more direct physical interpretation through homodyning with weak coherent fields (displacement) and photon counting (parity). This scheme has in fact been implemented on a pulsed EPR source demonstrating the first violation of local realism for continuous variables[69].

The reader might at this point object that we are not really considering observables with continuous spectra like position and momentum, i.e. quadrature amplitudes. It worth pointing out that even with such observables, any statement about local realism is most likely going to be formulated for dichotomic reductions of continuous outcomes (for example the sign of the position measurement). For such dichotomic reductions J.S. Bell claims that any system with a positive definite Wigner function can be described by a local theory, while he explicitly constructs a system with negative Wigner function which violates a local description (p. 196 in Ref.[64]). The general acceptance/rejection of this claim is at present not known to the author.

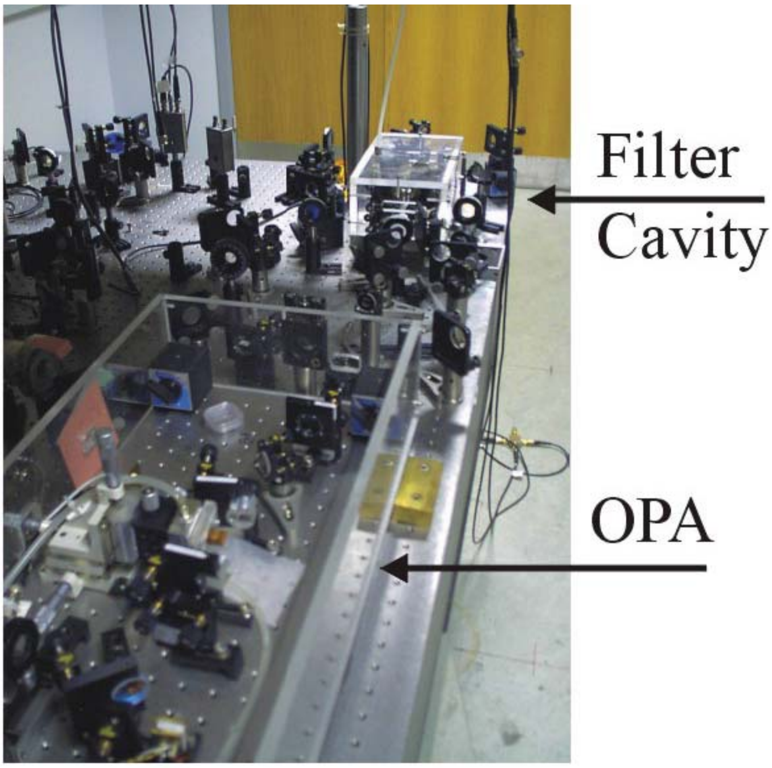

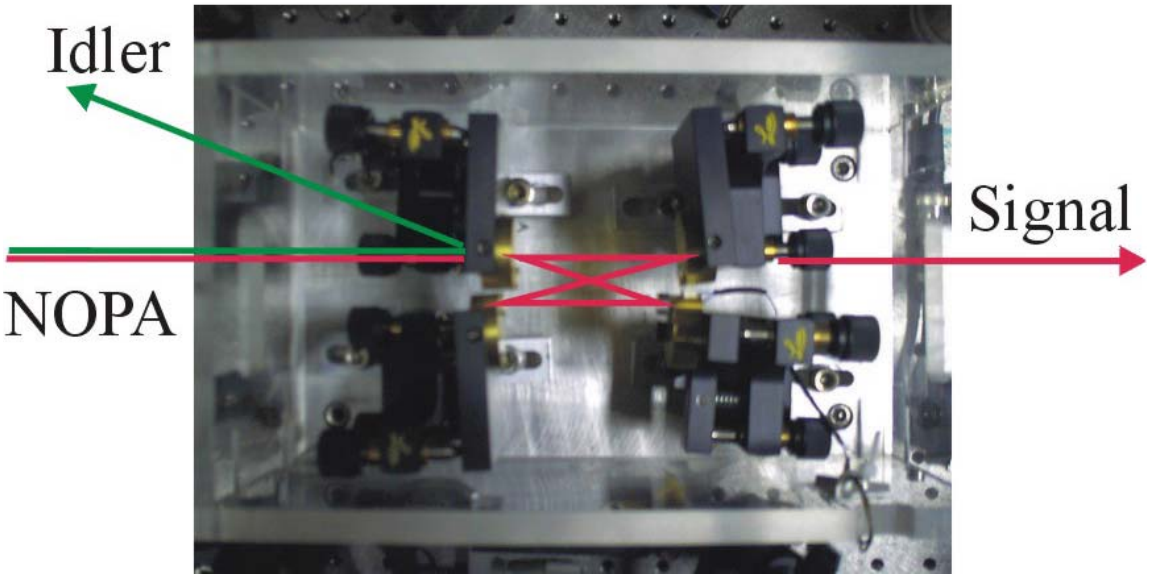

Figure 6.4: Pictures from the laboratory. Top : filter cavity following the OPA cavity (compare Fig.6.1). Buttom : close-up on filter cavity showing the spatial discrimination between signal and idler mode. The (false) coloring of signal and idler indicates their separation in frequency space by $2\Delta = 740$ MHz (compare Fig.6.2).

Chapter 7

Probing Atomic Backaction Noise with Squeezed Light

7.1 Introduction

We can divide quantum measurements into two classes : direct- and indirect measurement. The first type acts directly on the quantum object under investigation with a corresponding probabilistic projection in the measurement basis and destruction of the object. Examples include the direct photodetection of the photon number inside a cavity or the direct projection of a spin state onto spatial position by a Stern-Gerlach apparatus. The second type introduces a quantum probe which by unitary evolution gets entangled with the unknown object. The experimentalist, controlling the evolution, can now perform a direct measurement on the probe and extract information about some observable X_+ of the object. If carefully arranged, this procedure allows for a quantum non-demolition (QND) monitoring of X_+ with arbitrary precision, while leaving the experimentalist with a uniform distribution on the conjugate observable X_- as enforced by the Heisenberg uncertainty principle[70]. Consider the simplest nontrivial situation where the commutator $[\hat{X}_+, \hat{X}_-] = iC_x$ is just a c-number and the probe is described by a similar conjugate pair $[\hat{Y}_+, \hat{Y}_-] = iC_y$. For this object/probe system the unitary evolution $\hat{U} = \exp(-ia\hat{X}_+\hat{Y}_-)$ leaves the QND observable X_+ in the same state ($\hat{X}_+^{out} = \hat{X}_+^{in}$) if we insist that it is simultaneously an integral of the free motion. As we acquire X_+-information through the probe reading ($\hat{Y}_+^{out} = \hat{Y}_+^{in} + aC_y\hat{X}_+$) we become ignorant of X_- (uniform probability distribution) trough the *back action* coupling ($\hat{X}_-^{out} = \hat{X}_-^{in} + aC_x\hat{Y}_-$).

One obvious realization of the above ideas is in the coupling of two optical modes described by the quadratures $X_\pm$ and $Y_\pm$ ($C_x = C_y = 2$). It is straight forward to show that the unitary QND coupling is the sum of nondegenerate parametric amplification and mixing of the two modes. Indeed, the polarization NOPA combined with two waveplates for mixing has been used to demonstrate QND observation for this particular system[71],[72]. We have constructed a frequency NOPA (Chapters 5,6) but as yet we have no good candidate for a "beamsplitter"-element to mix the two optical modes separated by 740 MHz.

Another interesting unitary QND-coupling is realized by strong off resonant coupling between a single Rydberg atom crossing a microwave cavity which is in a superposition of 0 and 1 photon[73],[74]. We visualize the two level Rydberg atom (cavity photon superposition) on a Bloch sphere by the spin **J** (**S**) and take up/down along the z-axis to represent the upper/lower Rydberg level (1/0 photon in the cavity). The QND scheme is based on the dispersive atomic phaseshift induced by the presence of a single photon and recorded in a Ramsey interferometer[1]. The key element is a rotation of the

---

[1] Note that the QND experiment in ref. [74] relied on a *resonant* coupling to achieve the nessecary nonlinear phaseshift.

Rydberg probe around the z-axis *conditioned* on the state of the cavity. The probe rotation by an angle a takes the standard form $\hat{R}_z(a) = \exp(-ia\hat{J}_z)$ and if we condition this rotation on S_z we end up with a unitary evolution $\hat{U} = \exp(-ia\hat{S}_z\hat{J}_z)$. For $a = \pi$ this coupling allows for a QND monitoring of S_z, i.e. the cavity photon number.

In the above scheme $\hat{S}_z$ could in principle represent the difference between two orthogonal polarization states of a single cavity photon. In this case we can replace the Ramsey interferometer with a polarization interferometer and interchange the role of $\hat{J}_z$ and $\hat{S}_z$ as is clear from the symmetry of $\hat{U}$. This idea is introduced in ref.[75] where the authors also look at the feasibility of replacing the strong cavity coupling with the much weaker coupling between a free propagating optical field (many photons) and a large ensemble of atoms in the electronic groundstate. This system is much simpler to realize experimentally and it has recently been used to study several different aspects of the dispersive QND coupling. Common for these studies is the initial creation of two macroscopic or classical spin orientations along the x-axis. Defining $\langle \hat{J}_x \rangle = C_x$ and $\langle \hat{S}_x \rangle = C_y$ suggests that we think of $J_{y,z}$ and $S_{y,z}$ as two pairs of conjugate continuous quadrature observables. It is the coherent quantum noise in these variables we seek to redistribute by the QND coupling.

Towards this goal the collective spin of an atomic ensemble was squeezed by exploiting the possibility to QND-monitor J_z with precision beyond the standard quantum limit[76]. In another experiment the dispersive polarization probe S_x was send through two spatially separate atomic ensembles and subsequent measurement of S_y left the two ensembles in an entangled state with reduced noise in the joint EPR-variables $J_{z,1}+J_{z,2}$ and $J_{y,1}+J_{y,2}$[44]. This state is the material analog of the EPR quadrature correlations between the signal and idler modes from the NOPA (see Chapter 6). Recently we have combined the basic setup in Ref.[44] with our tunable source of nonclassical light[56](see Chapter 4). This has allowed us to investigate in detail the backaction noise inherent in the dispersive QND coupling. In this Chapter we present the results from this study which are also published in Ref.[45].

From a broader perspective the application of the OPA as a source of tunable nonclassical light for atomic spectroscopy was introduced in Ref.[77],[40]. In this work a squeezed probe (Cesium D2 line at 852 nm) was used to increase by 3 dB the signal to noise ratio of a shot noise limited absorption signal. The OPA source has also been applied in sub shotnoise polarization spectroscopy on the Cesium $6P_{3/2} \rightarrow 6D_{5/2}$ line (917 nm)[78],[79]. Finally, following a theoretical proposal[80], we have created a (weak) spin squeezed atomic ensemble by complete absorption of the OPA squeezed vacuum on the Cesium D2 line[43].

7.2 Theory

In this section we first introduce the Stokes vector $\hat{\mathbf{S}}$ describing the polarization state of an optical field (subsection7.2.1). Next we define the collective atomic spin $\hat{\mathbf{J}}$ and derive the dispersive QND-coupling $\hat{U} = \exp(-ia\hat{S}_z\hat{J}_z)$ (subsection7.2.2). Finally, in subsection7.2.3 we describe the polarization interferometer and calculate the probe spectrum $\Phi_{S_y}(\omega)$.

7.2.1 Stokes vector

We apply an angular momentum representation to the polarization state of the radiation field. Consider two orthogonal polarized modes x and y of the radiation field. The polarization state of a single photon propagating along the z-axis is a superposition of these modes. This simple two level system is equivalent to a point on the Bloch sphere of a spin 1/2 object and the action of a waveplate can be visualized as a rotation on this sphere. This idea is easy generalized : n photons in the same polarization state are represented by an angular momentum $\hat{\mathbf{S}}$ which is the sum of n spin 1/2 objects all pointing in the same direction. We call $\hat{\mathbf{S}}$ the Stokes vector. The quantization axis of the Stokes vector is (arbitrarily) defined by saying that the state of n photons in the x-mode is an eigenstate of $\hat{S}_x$ with eigenvalue $S_x = n/2$

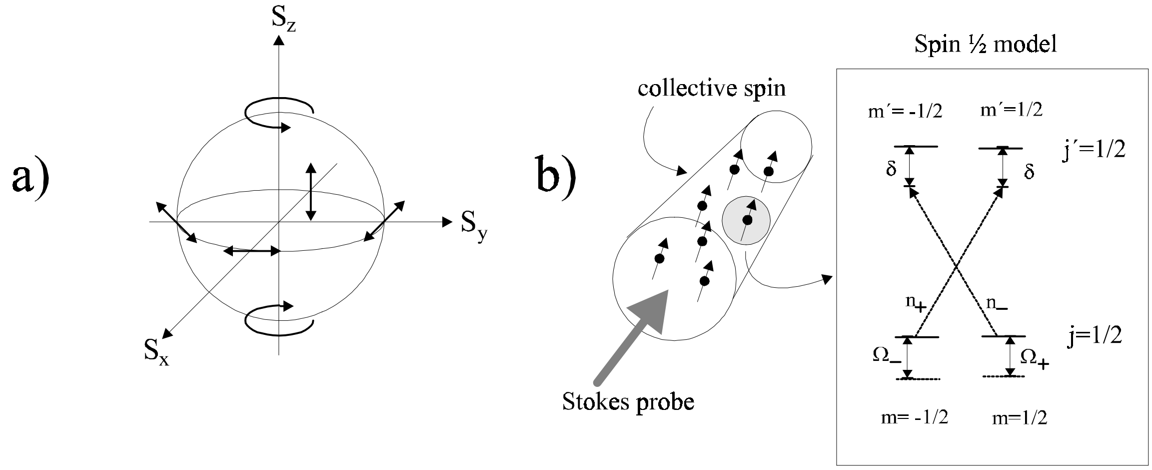

Figure 7.1: a) Stokes sphere respresenting the polarisation state of n identical photons. b) Stokes probe interaction with the collective spin of a roomtemperature ensemble of atoms. Inset) Spin 1/2 model used to derive the dispersive QND interaction.

$$\hat{S}_x = \frac{1}{2}(\hat{a}_x^\dagger \hat{a}_x - \hat{a}_y^\dagger \hat{a}_y) \tag{7.1}$$

Here $\hat{a}_x$ ($\hat{a}_y$) is the step-operator for mode x (y). The other components of the Stokes vector follow from the spin step-operators $\hat{S}_\pm = \hat{S}_y \pm i\hat{S}_z$

$$\hat{S}_y = \frac{1}{2}(\hat{S}_+ + \hat{S}_-) = \frac{1}{2}(\hat{a}_x^\dagger \hat{a}_y + \hat{a}_x \hat{a}_y^\dagger) \tag{7.2}$$

$$\hat{S}_z = \frac{1}{2i}(\hat{S}_+ - \hat{S}_-) = \frac{1}{2i}(\hat{a}_x^\dagger \hat{a}_y - \hat{a}_x \hat{a}_y^\dagger) \tag{7.3}$$

Here we use the fact that the step-operators flip a single spin 1/2 object, i.e. $\hat{S}_+ = \hat{a}_x^\dagger \hat{a}_y$ takes a photon from mode y to mode x and vice versa for $\hat{S}_-$. The Stokes vector has a simple physical interpretation. First note that $S_x = \langle \hat{S}_x \rangle$ measures the photon number difference between the x and y polarized modes. Now rotate the Stokes vector $S_x = n/2$ by an angle α around the z-axis, i.e. rotate each spin 1/2 object by the unitary operator[2]

$$\hat{R}_z(\alpha) = \exp(-i\hat{\boldsymbol{\sigma}}_z \alpha/2) = \begin{bmatrix} \cos(\alpha/2) & -\sin(\alpha/2) \\ \sin(\alpha/2) & \cos(\alpha/2) \end{bmatrix} \tag{7.4}$$

This matrix describes the action of a half-waveplate ($\lambda/2$) and thus all linear polarization states are distributed in the (S_x, S_y)-plane. If we instead rotate $S_x = n/2$ around the y-axis the rotation matrix in Eq.(7.4) becomes that of a quarter-waveplate ($\lambda/4$) and hence all elliptic polarization states (with major axis along x,y) are distributed in the (S_x, S_z)-plane. The pictorial representation of the Stokes vector is shown in Fig.7.1a.

7.2.2 Collective spin and dispersive probe interaction

In Fig7.1b we show a glass cell which confines N identical atoms each with groundstate spin $j = 1/2$. Clearly this system of identical two level systems is described by an angular momentum like the Stokes

---

[2] Note that the Pauli matrices here are defined in accord with the quantization along the x-axis, such that $\hat{\sigma}_x = \begin{bmatrix} 1 & 0 \\ 0 & -1 \end{bmatrix}$, $\hat{\sigma}_y = \begin{bmatrix} 0 & 1 \\ 1 & 0 \end{bmatrix}$, $\hat{\sigma}_z = \begin{bmatrix} 0 & -i \\ i & 0 \end{bmatrix}$.

vector. We call this vector the collective spin $\hat{\mathbf{J}} = \sum_{i=1}^{N} \hat{\jmath}^{(i)}$ and quantize it along the propagation direction of the Stokes probe (z-axis). The Stokes vector is going to probe the groundstate $j = 1/2$ via an electric dipole transition to the excited level $j\prime = 1/2$ as shown by the inset in Fig.7.1b. This interaction shifts the groundstate level $m = \pm 1/2$ by the effective Rabi frequency $\Omega_\pm = ((\delta/2)^2 + 4g^2 n_\mp)^{1/2}$ which depends on the probe detuning δ, the vacuum Rabi frequency g, and the number of left/right-circularly polarized photons in the probe $n_\mp$. For large detuning we can neglect real transitions and approximate the dispersive light shift of the i´th atom by $\Delta E_\pm^{(i)} = \hbar g^2 n_\pm/\delta$. Defining $N_\pm$ as the average number of atoms in state $m = \pm 1/2$ we can write the average light shift for the collective spin in the form

$$\left\langle \sum_{i=1}^{N} \Delta E_\pm^{(i)} \right\rangle = \frac{\hbar g^2}{\delta} \left[N_+ n_- + N_- n_+ \right] = \frac{4\hbar g^2}{\delta} \left[\frac{1}{4} N n - \langle \hat{J}_z \rangle \langle \hat{S}_s \rangle \right] \tag{7.5}$$

In the last step we used the relations $N = N_+ + N_-$, $n = n_+ + n_-$, $\langle \hat{J}_z \rangle = 1/2(N_+ - N_-)$, and $\langle \hat{S}_z \rangle = 1/2(n_+ - n_-)$. Neglecting the constant contribution $\sim nN$ we can generate this light shift from the effective Hamiltonian $\hat{H} = \frac{\hbar g^2}{\delta} \hat{J}_z \hat{S}_z$. The dispersive interaction between the Stokes vector and the collective spin corresponds to a joint rotation of both spins about the z-axis (compare introduction)

$$\hat{U} = \exp(-ia\hat{J}_z\hat{S}_z) \tag{7.6}$$

Here $a = \frac{\sigma\gamma}{A\delta}$ where σ is the atomic resonant absorption cross section, A is the spatial overlap area of the Stokes probe and atomic vapour cell, and γ is the linewidth of the dipole transition[81]. The joint rotation in Eq.(7.6) leaves both $\hat{J}_z$ and $\hat{S}_z$ invariant while their values can be read out in the transverse spin components

$$\hat{S}_y^{(out)} = \hat{S}_y^{(in)} + aS_x\hat{J}_z \tag{7.7}$$

$$\hat{J}_y^{(out)} = \hat{J}_y^{(in)} + aJ_x\hat{S}_z \tag{7.8}$$

These input/output relations assume that (i) both spins are initially polarized along the x-axis and (ii) small rotations, i.e. $\hat{S}_x$ ($\hat{J}_x$) can be replaced its average value S_x (J_x). With these conditions satisfied we are essentially working in the reduced Hilbert space of transverse spin components with commutators $[\hat{S}_y, \hat{S}_z] = iS_x$ and $[\hat{J}_y, \hat{J}_z] = iJ_x$. The transverse spin components are zero on average and their coherent noise proportional the size of the spin, i.e. spin projection noise $\langle \hat{S}_{y,z}^2 \rangle = S_x/2$ and $\langle \hat{J}_{y,z}^2 \rangle = J_x/2$. On the experimental side we are going to monitor the spin noise in $\hat{S}_y$ and try to resolve its modification due to (i) the atomic projection noise in $\hat{J}_z$ (7.7) and (ii) the *backaction noise* on atoms $\hat{S}_z$ (7.8) which we couple back into $\hat{S}_y$ by rotating the collective spin about J_x (see next section). To separate the contributions (i) and (ii) we need a "handle" by which we can redistribute the coherent noise of the input Stokes vector. For this purpose we use the squeezed vacuum output from the OPA (Chapter 4) as described in the next section.

7.2.3 Polarization interferometer and the spectrum of $\hat{S}_y$

Standard two level interferometry can be analyzed in three steps : (i) prepare n spin 1/2 objects in initial state (Stokes vector) (ii) send the objects through the probe region (rotate Stokes vector), (iii) analyze objects in Stern-Gerlach two state analyzer (measure component of Stokes vector). Standard interferometer names are Mach Zehnder, Sagnac, Ramsey and spin 1/2 objects are spatial- or polarization modes of photons, neutrons, atoms etc.[82].

We use the polarization interferometer to prepare, rotate and analyze the Stokes vector as shown in Fig.7.2. The polarizing beamsplitter PBS1 combines a local oscillator (LO) mode $A_x e^{i\varphi}$ with the squeezed OPA mode $\hat{a}_y$. This prepares the Stokes vector $S^{(in)}$ with mean value $\langle \hat{S}_x \rangle = S_x = \frac{1}{2}A_x^2$ and

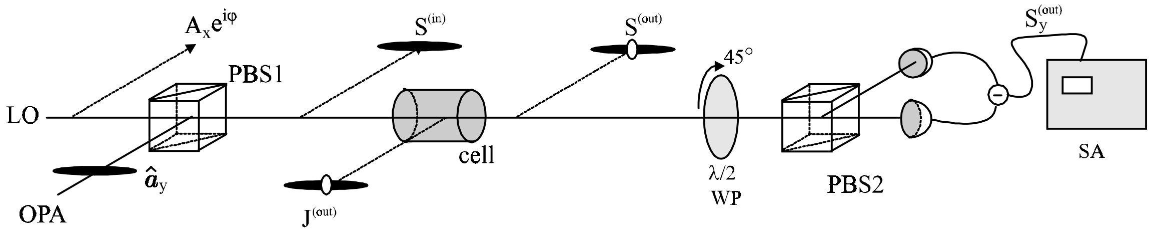

Figure 7.2: Polarization interferometer measuring the noise spectrum of the Stokes probe $S_y^{(out)}$. The spectrum has two contributions : (i) the intrinsic probe noise set by the vacuum fluctuations of the OPA (black ellipse), and (ii) the readout of atomic noise by the dispersive coupling (white ellipse). Note the *backaction* of the probe on the atomic sample (black ellipse on top of $J^{(out)}$).

transverse components

$$\hat{S}_y = \frac{A_x}{2}(\hat{a}_y e^{-i\varphi} + \hat{a}_y^\dagger e^{i\varphi}) = \frac{A_x}{2}\hat{Q}_\varphi, \quad \Rightarrow \langle \hat{S}_y^2 \rangle = \frac{S_x}{2}\langle \hat{Q}_\varphi^2 \rangle = \frac{S_x}{2}\epsilon_y \tag{7.9}$$

$$\hat{S}_z = \frac{A_x}{2i}(\hat{a}_y e^{-i\varphi} - \hat{a}_y^\dagger e^{i\varphi}) = \frac{A_x}{2}\hat{Q}_{\varphi+\pi/2} \quad \Rightarrow \langle \hat{S}_z^2 \rangle = \frac{S_x}{2}\langle \hat{Q}_{\varphi+\pi/2}^2 \rangle = \frac{S_x}{2}\epsilon_z \tag{7.10}$$

Here $\hat{Q}_\varphi$ is the operator describing the quadrature observable of the OPA mode. The phase sensitive noise in this observable and its conjugate is parametrized by the two numbers ϵ_y and ϵ_z. Thus the transverse spin noise on the Stokes vector (solid ellipse on the tip of $S^{(in)}$) is dictated by the quadrature squeezing in the OPA. If we remove the atomic cell in the probe region it is clear that the S_y-analyzer (WP+PBS2) is just a balanced homodyne detector : the classical LO with phase φ is overlapped with the squeezed OPA mode on a 50/50 beamsplitter (PBS2). With the phase locked to $\varphi = \pi/2$ we squeeze (antisqueeze) $\hat{S}_y$ ($\hat{S}_z$). The corresponding noise level $\epsilon_y < 1$ ($\epsilon_z > 1$) reads directly off the spectrum analyzer (SA) by normalization to the coherent spin noise $\epsilon_y = \epsilon_z = 1$.

Next we analyze the change in the interferometer output spectrum when placing the atomic vapour cell in the probe region. The spectral density of the Stokes vector component is introduced in the form $\Phi_{S_{y,z}}(\omega) = \mathcal{F}\{\langle \hat{S}_{y,z}(0), \hat{S}_{y,z}(\tau)\rangle\}$ where as usual $\mathcal{F}$ is the Fourier transform with respect to τ. With the additional definition of the spectrum of atomic fluctuations $\Phi_{J_z}(\omega) = \mathcal{F}\{\langle \hat{J}_z(0), \hat{J}_z(\tau)\rangle\}$ we can write down the interferometer output spectrum from Eq.(7.7)

$$\Phi_{S_y^{(out)}}(\omega) = \Phi_{S_y^{(in)}}(\omega) + a^2 S_x^2 \Phi_{J_z}(\omega) = \frac{S_x}{2}\epsilon_y + a^2 S_x^2 \Phi_{J_z}(\omega) \tag{7.11}$$

To calculate the atomic fluctuation spectrum we combine the backaction term Eq.(7.8) with a simple "cavity" model

$$d\hat{J}_y/dt = -\Omega \hat{J}_z(t) - \Gamma \hat{J}_y(t) + \hat{\mathcal{L}}_y(t) + a J_x \hat{S}_z(t) \tag{7.12}$$

$$d\hat{J}_z/dt = \Omega \hat{J}_y(t) - \Gamma \hat{J}_z(t) + \hat{\mathcal{L}}_z(t) \tag{7.13}$$

The cavity analogy is obvious once we set $a = 0$ and interpret $(J_x/2)^{-1/2}\hat{J}_{y,z}$ as conjugate quadrature observables with commutator $2i$. Then equation (7.12) and (7.13) describe the decay of an oscillator with resonance frequency Ω and full width 2Γ. The scaled Langevin force $(J_x/2)^{-1/2}\hat{\mathcal{L}}_j(t)$ with $j = y, z$ preserves the commutator of the decaying operators. It has zero mean and a delta-correlation $(J_x/2)^{-1}\langle \hat{\mathcal{L}}_j(t), \hat{\mathcal{L}}_k(t')\rangle = 2\Gamma \delta_{jk}\delta(t - t')$ where the diffusion 2Γ is linked to the cavity decay rate by the fluctuation-dissipation theorem[83]. The diffusion for the collective spin, i.e. $(J_x/2)2\Gamma = \Gamma J_x$, equalizes the noise in the conjugate transverse spin components on a timescale Γ^{-1}. The resonant atomic structure gives rise to the usual Lorentzian power spectrum of spin projection noise

$$\Phi^{a=0}_{J_z}(\omega) = \frac{1/4}{(\Omega-\omega)^2+\Gamma^2}\{\Gamma J_x\} \tag{7.14}$$

With reference to the experimental section below we mention in passing that the atomic resonance Ω is controlled by an externally applied DC magnetic field and the primary source of decoherence Γ is the optical pumping process by which we spin polarize atoms. The interferometer probe reads out the Lorentzian structure of $\hat{J}_z$ (white ellipse on tip of $S^{(out)}$) with gain set by the dispersive coupling parameter a (7.11). Simultaneously the conjugate spin component $\hat{J}_y$ is excited (black ellipse on $J^{(out)}$) by the backaction term $aJ_x\hat{S}_z$ (7.12). This in turn modifies the observed Lorentzian. To calculate the change $\Phi^{a=0}_{J_z} \to \Phi^{a\neq 0}_{J_z}$ we simply note that the back action behaves like a stochastic force with delta correlation[3] $\langle aJ_x\hat{S}_z(t), aJ_x\hat{S}_z(t')\rangle = a^2J_x^2\frac{S_x}{2}\epsilon_z\delta(t-t')$. The corresponding diffusion term $a^2J_x^2\frac{S_x}{2}\epsilon_z$ from the probe backaction simply adds to the normal diffusion ΓJ_x within the curly brackets in Eq.(7.14). The predicted probe spectrum Eq.(7.11) can now be written in the form

$$\Phi_{S_y}(\omega) = \frac{S_x}{2}\epsilon_y + \frac{\frac{1}{4}a^2S_x^2}{(\Omega-\omega)^2+\Gamma^2}\left\{\Gamma J_x + \frac{a^2J_x^2S_x\epsilon_z}{2}\right\} \tag{7.15}$$

To briefly summarize, the first term in Eq.(7.15) is the (white) probe shot noise while the last two terms are due to Lorentzian narrowband atomic spin fluctuations. The first term inside the curly brackets is the normal spin diffusion noise caused by optical pumping while the second term describes spin diffusion due to backaction of the probe on atoms. We now turn to discuss specific details of the experimental setup, data -acquisition and analysis.

7.3 Experiment

7.3.1 Phase and frequency locking the probe - Stokes vector preparation

The essential parts of the experimental apparatus are displayed for reference in Fig.7.3a. The probe is prepared with the squeezing setup described in Chapter 4. The squeezed OPA mode is spatially overlapped with the orthogonal polarized local oscillator (PBS1). The two modes are mixed (50/50) by projecting onto a 45 degree rotated polarization basis (WP+PBS2) and the balanced homodyne spectrum $\Phi_{S_y}(\omega)$ is recorded with the spectrum analyzer (SA1). During data acquisition we operate with a squeezed probe quadrature $\epsilon_y < 1$ and antisqueezed backaction quadrature $\epsilon_z > 1$, i.e. we lock the LO phase to the point $\varphi = \pi/2$. The phase lock error signal is derived by exciting a mechanical resonance ($\sim$ 50 kHz) in the feedback piezo mirror (PZT) controlling the LO phase φ. Lock-in detection (Lock-in) of the corresponding modulation on the homodyne spectrum (SA2) generates an errorsignal when crossing the sinusoidal extrema of the phase-sensitive spectrum Φ_{S_y}. The squeezing observed just after the OPA is typically 4 dB but additional loss on the long propagation path (10 m) between the source and the detection zone leaves us with 3 dB noise reduction in the probe quadrature, i.e. $\epsilon_y = 0.5$. The antisqueezing is typically 8-9 dB corresponding to $\epsilon_z = 6-8$. The probe analyzer SA1 is centered on the Lorentzian spin resonance at Ω while the lock analyzer (SA2) is centered on the far wing of the Lorentzian to get a clean errorsignal (no spin contribution).

As discussed in Chapter 4 the OPA is engineered to produce tunable nonclassical light around the Cesium D2 dipole transition at 852 nm. The hyperfine structure of this transition is shown in Fig.7.3b. The blue detuned probe is locked to the dipole transition using the same FM technique ([50]) which we apply for cavity locking (see Chapter 4). But now the cavity resonance is replaced by the Doppler

---

[3] The OPA bandwidth is several orders of magnitude larger than Γ and thus the squeezed vacuum looks like a white noise reservoir to atoms.

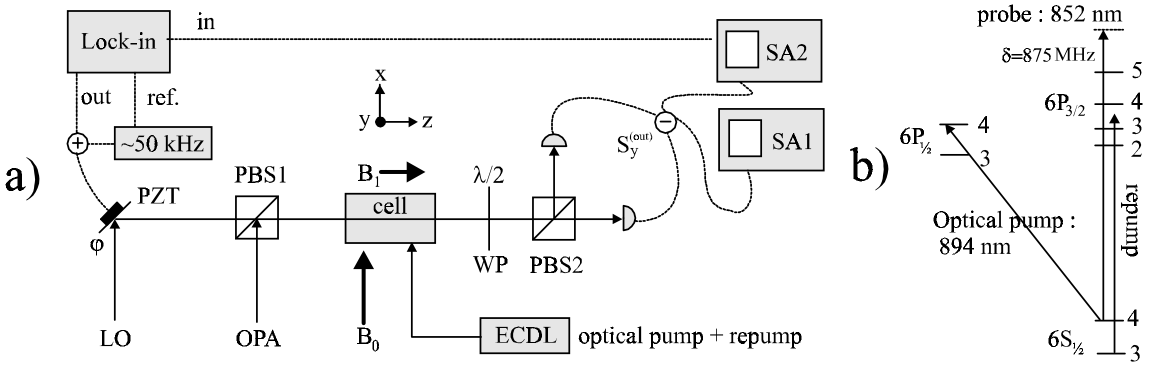

Figure 7.3: a) Experimental setup. The Lorentzian spin noise resonance is recorded on the spectrum analyzer SA1. The phase φ is stablized by lock-in detection of the modulated light noise recorded on SA2. b) Hyperfine level scheme for cesium. The Stokes probe is blue detuned by $\delta = 875$ MHz. The collective spin is created by the optical pump and repump beam.

free saturated absorption signal from $6S_{1/2}(F = 4) \rightarrow 6P_{3/2}(F = 5)$. A small part of the LO is send through a fiber coupled EOM which generates primary sidebands at 875 MHz each with secondary 20 MHz sidebands for locking. Probing the saturated transition with the red primary sideband produces the $\delta = 875$ MHz blue detuned probe shown in Fig.7.3b.

7.3.2 Optical pumping - collective spin preparation

The dispersive probe interacts with roughly 10^{12} cesium atoms inside an atomic vapour glass cell with dimension 2x2x3 cm^3. The atoms are at room temperature with rms velocity $v_{x,rms} = 136$ m/s and all optical transitions are accordingly Doppler broadened with Gaussian width $\delta\nu = 373$ MHz. The elementary angular momentum $\hat{\mathbf{f}}^{(k)}$ is taken to be the Cesium hyperfine groundstate $F = 4$ of the k´th atom and the collective spin in the experiment is defined as the sum $\hat{\mathbf{J}} = \sum \hat{\mathbf{f}}^{(k)}$ over the fraction of atoms in $F = 4$. The remaining fraction of atoms will occupy the second hyperfine groundstate $F = 3$. Experimentally we control the relative population between $F = 3, 4$ and thus the size J_x of the collective spin by tuning the power of a repump laser locked to the crossover transition $6S_{1/2}(F = 3) \rightarrow 6P_{3/2}(F = 3, 4)$. The orientation of the collective spin is defined by applying a DC magnetic field B_0 along the x-axis. This perturbation removes the degeneracy of the groundstate magnetic sublevels $m = -F, ..m = +F$ quantized with respect to the field. The $F = 4$ groundstate is polarized by absorbing angular momentum from a circularly polarized pump beam propagating along the magnetic field axis. The σ_+-helicity of the optical pump drives each atom towards the magnetic sublevel $F, m = 4, 4$ thereby creating the collective spin J_x. The optical pump is locked to the D1 transition $6S_{1/2}(F = 4) \rightarrow 6P_{1/2}(F = 4)$ at 894 nm which has the advantage of turning the groundstate level $F, m = 4, 4$ into a dark state with respect to the σ_+-pump. Both the optical pump and repump beams are derived from extended cavity diode lasers (ECDL).

The Zeeman splitting derives from the magnetic dipole interaction $\hat{H}_{dip} = -\hat{\boldsymbol{\mu}}\mathbf{B} = g_j \mu_B B_0 \hat{\jmath}_x$.Here μ_B is the Bohr magneton and g_j is the Lande factor for $\hat{\mathbf{j}} = \hat{\mathbf{l}} + \hat{\mathbf{s}}$ which is the sum of orbital- and electronic angular momentum. Typically an atom also has nuclear spin $\hat{\mathbf{i}}$ and we have to evaluate $\hat{\jmath}_x$ in the eigen-basis of the total angular momentum $\hat{\mathbf{f}} = \hat{\mathbf{j}} + \hat{\mathbf{i}}$. This can be done by invoking the projection theorem[20] which is valid within a given f-manifold

$$\hat{\jmath}_x = \frac{\left\langle \hat{\mathbf{j}}\hat{\mathbf{f}} \right\rangle}{f(f+1)} \hat{f}_x = \frac{f(f+1) + j(j+1) - i(i+1)}{2f(f+1)} \hat{f}_x \qquad (7.16)$$

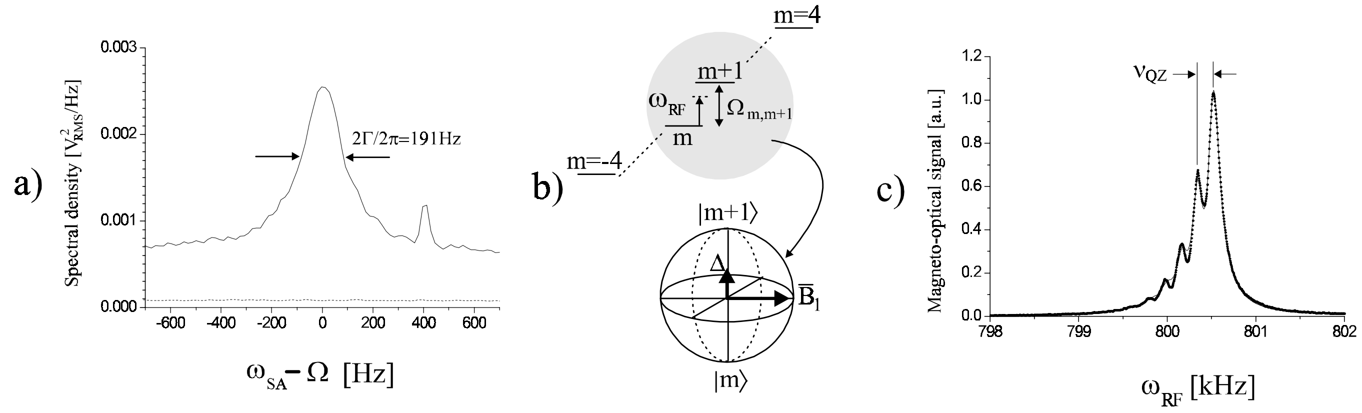

Figure 7.4: a) Lorentzian spin noise measured with coherent probe $\epsilon_y = \epsilon_z = 1$. ω_{SA} is the frequency component of the spectral density and $\Omega = 325$ kHz is the Larmor frequency at the magnetic bias field $B_0 = 0.93$ Gauss. The flat trace close to zero is the noise contribution from electronics. b) Magnetic Zeemann splitting of the m↔m+1 transition in the $F = 4$ manifold. An applied RF-field (B_1) induces transitions between the two magnetic sublevels when the detuning $\Delta = \Omega_{m,m+1} - \omega_{RF}$ is close to zero. c) Scanning ω_{RF} we observe 8 lines in the spectral density. The relative strength of these lines is used to deduce the population and spin polarisation of the $F = 4$ manifold. Note that $B_0 = 2.29$ Gauss in this trace to better resolve the quadratic Zeeman splitting.

For the Alkali-atom groundstate with quantum numbers $l = 0$, $j = s = 1/2$, and $f = i \pm j$ the replacement $g_j \hat{j}_x \rightarrow g_f \hat{f}_x$ leads to the new Lande factor $g_f = \pm\frac{1}{i+1/2}$. The linear (low field) Zeeman splitting of the Cesium groundstate ($i = 7/2$) is then fully characterized by the Larmor frequency

$$\nu_L = \frac{g_f \mu_B B_0}{h} = 349.8 \text{ kHz} \cdot B_0[\text{Gauss}] \tag{7.17}$$

Any time-dependent groundstate observable oscillates at this single Bohr-frequency including the transverse collective spin components $\hat{J}_y$ and $\hat{J}_z$. Thus the angular Larmor frequency $\Omega = 2\pi\nu_L$ is the "cavity"-resonance introduced in Eq.(7.12,7.13), i.e. the Lorentzian spin resonance in Eq.(7.15).

Up to this point we have neglected the following problem. The basic dispersive evolution $\hat{U} = \exp(-ia\hat{J}_z\hat{S}_z)$ is derived for an ensemble of spin $j = 1/2$ atoms, but the experimental work is based on the larger angular momentum $F = 4$. This substitution is identical to the replacement of the Alkali-groundstate electronic spin $\hat{j}_x$ with the total spin $\hat{f}_x$ which is the essence of the projection theorem Eq.(7.16). Thus at least in the linear Zeeman regime there seems to be some justification for the replacement scheme : $j = 1/2 \rightarrow F = 4$ and $a \rightarrow a(g_f/g_j)$[81].

7.3.3 Spin noise with coherent probe and magnetometry

Spin noise data are recorded with the magnetic field strength $B_0 = 0.93$ Gauss corresponding to a spin resonance at $\Omega/2\pi = 325$ kHz. The resonance is recorded in the following way. First the $\hat{S}_y$-photocurrent is mixed down to DC with an RF lock-in amplifier (SR844) supplied with a stable reference signal at the Larmor frequency (HP3325B). This signal is then processed by a high resolution FFT analyzer (SR780) which displays the powerspectrum of $\hat{S}_y$ in a frequency window varying from 1.6 kHz to 3.2 kHz around $\Omega/2\pi$. A typical spin noise spectrum is shown in Fig.7.4a where datapoints are separated by the resolution bandwidth $RBW = 16$ Hz and the curve is averaged with video bandwidth $VBW < 1$ Hz. It should be stressed that this trace is obtained with a coherent probe ($\epsilon_y = \epsilon_z = 1$). The corresponding squeezed probe spectrum will be analyzed in the next section. The flat trace (dotted curve) shows the power contribution from detector noise.

In accordance with our model (7.15) we fit the spectrum in Fig.7.4a with a Lorentzian (spin noise) plus a constant (probe shot noise). From the Lorentzian part we extract the linewidth $2\Gamma/2\pi = 191$ Hz (FWHM) and the total spin noise area A_{COH} where the subscript refers to the coherent probe. The linewidth is much smaller than the average wall-to-wall collision rate due to a paraffin coating of the atomic cell which preserves the spin coherence. In fact this coating allows for linewidth well below what we observe. Our linewidth is limited to above 100 Hz by atom collision, quadratic Zeeman effect (see below), and power broadening caused by the probe beam. The power broadening is hard to avoid since the readout of spin noise scales with S_x (7.15) and a strong probe is needed to get a spin noise dominated spectrum. Additional power broadening is caused by the pump laser and we use this effect in the experiment to vary the linewidth in the range from 100 Hz to 1 kHz.

The spin noise area A_{COH} depends on the size of the collective spin and for quantitative analysis we need an independent (relative) measure of J_x for each area. We obtain this information by magnetometry[84] where we observe the spin noise in $\hat{S}_y$ against the frequency ω_{RF} of an RF magnetic field with amplitude B_1 and orientation perpendicular to B_0 (see Fig.7.3a). The two level interaction picture in Fig.7.4b demonstrates how the orthogonal RF-field induces transitions between the magnetic sublevels m and $m+1$. Here $\Delta = \omega_{RF} - \Omega_{m,m+1}$ is detuning of the RF frequency from the $m \to m+1$ resonance and $\bar{B}_1$ is the on-resonance Rabi-frequency proportional to the field strength B_1 and the magnetic dipole coupling. With linear Zeeman splitting all $\Omega_{m,m+1}$ are identical in which case the magnetometer signal would be identical to the spin noise spectrum in Fig.7.4a with additional classical noise caused by the slow Rabi-modulation. This degenerate resonance can reveal no information about the different m-level populations and hence J_x. However the quadratic Zeeman effect removes this degeneracy and we obtain 8 transition lines separated by

$$\nu_{QZ}[\mathrm{Hz}] = 2.18 \cdot 10^{-4} (\nu_L[\mathrm{kHz}])^2 \tag{7.18}$$

Fig.7.4c shows a magnetometer trace with evenly spaced Zeeman resonances. The solid line is a three parameter fit to magnetometer signal from which we extract the (relative) number N of atoms in $F = 4$ and the single atom polarization p. We then assign the collective spin value $J_x = Np$ to the spin noise area A_{COH} observed with the same probe and pump parameters. Note that the magnetometer signal is recorded at a higher Larmor frequency to observe well separated Zeeman resonances.

7.3.4 Spin noise with squeezed probe

In Fig.7.5a we reproduce the spin noise trace from Fig.7.4a (solid curve) which was obtained with a coherent probe $\epsilon_y = \epsilon_z = 1$, i.e. with the OPA blocked. With identical parameters (pump, repump, Larmor frequency etc.) we now unblock the OPA and obtain a second Lorentzian trace (dotted curve). During acquisition the Stokes vector is fixed with parameters $\epsilon_y < 1$ and $\epsilon_z > 1$ by stabilizing the local oscillator phase to $\varphi = \pi/2$. Comparing the two traces we observe several effects. First the reduced probe shotnoise ($\epsilon_y < 1$) is seen in the Lorentzian wing as expected. Second, and more interesting, the increased noise in the backaction quadrature ($\epsilon_z > 1$) is seen as an increase in peak height of the Lorentzian spin noise. Finally the linewidth 2Γ is left unchanged. These effects are in qualitative agreement with the theoretical model as expressed by the probe spectrum $\Phi_{S_y}(\omega)$ in Eq.(7.15).

For a quantitative comparison we now fit the squeezed probe trace (dotted curve) and extract the spin noise area A_{SQ}. Since the backaction contribution to the spin noise area is proportional to ϵ_z it is useful to introduce the separation $A_{SQ} = A_B\epsilon_z + A_R$, where we have defined the *back action noise area* A_B and the *residual spin noise area* A_R. For a coherent probe we have the additional relation $A_{COH} = A_B + A_R$, and we find the useful relation $A_B = (A_{SQ} - A_{COH})/(\epsilon_z - 1)$ together with $A_R = (A_{SQ} - \epsilon_z A_{COH})/(\epsilon_z - 1)$.

The experimental spin noise areas are tested against theoretical predictions by integrating the spectral density Eq.(7.15) over frequency. The result is

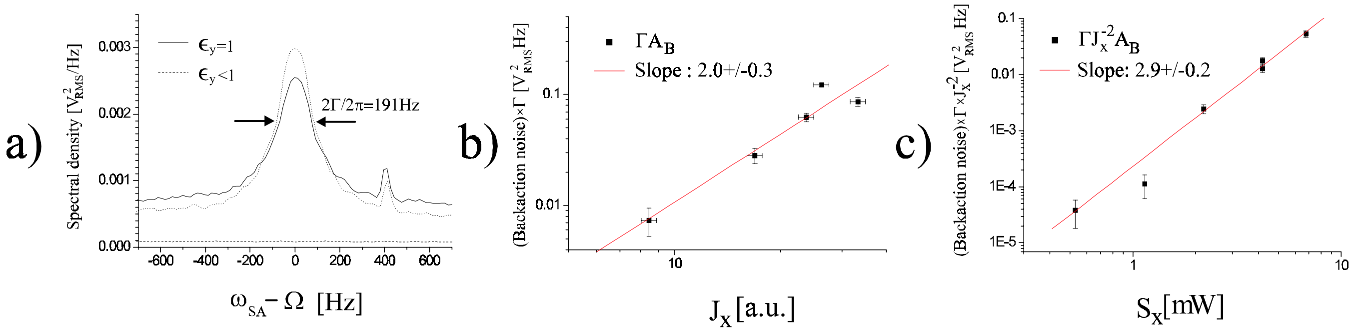

Figure 7.5: a) Lorentzian spin noise measured with squeezed probe ($\epsilon_y < 1$) and compared to the coherent probe spectrum ($\epsilon_y = 1$). With a squeezed probe the Lorentzian part from atoms increases while the probe part, which dominates the wing, decreases. b) Scaling of backaction noise A_B with collective spin J_x, i.e. number of atoms in $F = 4$. The linear fit is consistent with our simple model, see Eq.7.19. c) Scaling of backaction noise with probe power S_x. Again the experimental data agree with theory.

$$A_B = \frac{\pi a^4 J_x^2}{\Gamma}\left(\frac{S_x}{2}\right)^3 \tag{7.19}$$

$$A_P = 2\pi a^2 J_x \left(\frac{S_x}{2}\right)^2 \tag{7.20}$$

Here we have introduced the *projection noise area* A_P which would equal the residual noise A_R in the absence of technical (classical) spin noise in the measurement. Combining the backaction- and projection noise areas we obtain the relation

$$A_P = 2(\pi\Gamma \times A_B \times S_x/2)^{1/2} \tag{7.21}$$

Note that the *shot noise level* $S_x/2$ comes out as the constant in the "constant+Lorentzian" fit. Now by respectively blocking/unblocking the OPA input to the interferometer we vary the quantum state of the probe ϵ_z and measure A_{COH}/A_{SQ} from which we calculate the backaction area A_B. With the knowledge of A_B and $S_x/2$ we use Eq.(7.21) to deduce the projection area A_P.

7.3.5 Experimental results

In the first two measurement series we confirm the scaling of the back action noise area A_B with Stokes vector S_x and collective spin J_x. Shown in Fig.7.5c is A_B against S_x which is controlled by the probe power. In Fig.7.5b we plot A_B against J_x which we vary by adjusting the repumping laser power and thereby the relative populations in $F = 3, 4$. We find A_B to scale with S_x^p where $p = 2.9 \pm 0.2$, and J_x^q with $q = 2.0 \pm 0.2$ in good agreement with theory (7.19). During the sequence of measurements we observe less than 10% variation in the parameters ϵ_y and ϵ_z which together with the statistical error from the Lorentzian fits account for the error bars on the datapoints.

Next we observe the change in $A_{COH} = A_B + A_R$ with Γ. Again the extra datapoint with squeezed probe A_{SQ} allow us to separate the two contributions A_B and A_R. In Fig.7.6a the back action contribution A_B is shown to decrease with Γ^{-1} to within a few percent in accord with the theoretical prediction. The residual noise contribution A_R, shown in Fig.7.6b, also decreases roughly like Γ^{-1} until a value of approximately $2\Gamma = 500$ Hz is reached. Here A_R approaches a constant value

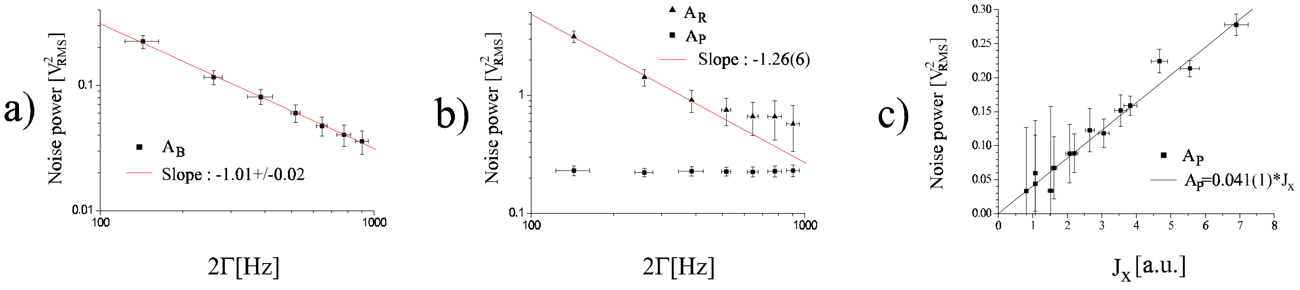

Figure 7.6: a) Backaction noise A_B plotted against the width Γ of the Lorentzian spin resonance. The experimental data agree with the scaling law $A_B \propto \Gamma^{-1}$. b) Measured residual spin noise A_R versus Γ. For high Γ this contribution decreases towards the limit set by intrinsic projection noise A_P (see text). c) From experimental data we predict and plot the projection noise A_P against the collective spin J_x. Varying the number of atoms over roughly one order of magnitude we confirm proportionaly between A_P and J_x (compare Eq.7.20).

independent of Γ which we interpret in the following way. As Γ is increased the spin diffusion ΓJ_x caused by optical pumping washes out technical spin noise and thus leads to a reduction in residual spin noise. At even higher Γ this mechanism will dominate and A_R will converge to the (constant) projection noise level A_P set by the optical pump. To support this picture we estimate A_P for each datapoint using Eq.(7.21). This estimate is also shown in Fig.7.6b where we see that A_R indeed approaches A_P for higher Γ.

Finally, we fix Γ and vary the number of atoms J_x. We measure A_B and use Eq.(7.21) to infer the projection noise area A_P which we plot against J_x in Fig.7.6c. The linear fit through zero confirms the predicted scaling (7.20). The plotted results are obtained at two very different decay rates $2\Gamma = 264 \pm 20$ Hz and $2\Gamma = 485 \pm 20$ Hz, thus confirming the independence of A_P on Γ already observed in Fig.7.6b.

7.4 Summary and outlook

In this Chapter we use a simple spin 1/2 model to derive a dispersive QND-type coupling between the polarization state of an optical probe beam and the collective spin state of an atomic ensemble. Combining this coupling with a resonant "cavity" decay model for the collective spin we calculate the spectrum of fluctuations of the transmitted probe. The spectrum is composed of two parts : (i) the white probe noise, and (ii) the resonant spin noise which has a Lorentzian profile set by the decay model. The integrated spin noise density is the sum of a backaction part $A_B\epsilon_z$ and a residual noise part A_R. Here the backaction part is proportional to the parameter ϵ_z which defines the quantum fluctuations in one probe quadrature. A_R is independent of the parameter ϵ_z which can be modulated by respectively blocking/unblocking the squeezed vacuum output from our optical parametric oscillator. By this method we separate the backaction noise from the residual spin noise. Comparing experimental data with the spin 1/2 model we find good agreement, but it should be pointed out that the regime of reduced backaction noise ($\epsilon_z < 1$) remains to be explored.

Experimentally the collective spin is "approximated" by the $F = 4$ hyperfine groundstate in a room temperature vapour of cesium. Applying a magnetic bias field we control the Larmor frequency which defines the spin resonance (325 kHz). The width of this resonance is limited to above 100 Hz by collisions, quadratic Zeeman effect, and probe power broadening. Additional power broadening by an optical pump laser allow us to control this width over one order of magnitude. All experimental data is recorded in the form of Lorentzian traces from which we extract A_B and A_R (see Fig.7.5a).

The results from analyzing this data is presented in the plots shown in Fig.7.5b,c and Fig.7.6a,b,c. In conclusion our data agree well with the theory thus supporting the suggested dispersive QND coupling between atoms and light.

7.4.1 Hot topic: quantum memory

It is interesting to discuss our results in relation to the emerging field of quantum information science. We approach this subject through the generic two level superposition $\alpha|\uparrow\rangle + \beta|\downarrow\rangle$ also known as a qubit. While classical computers code binary information on the north- and south pole of the qubit Bloch sphere, quantum computers should take advantage of the full 4π solid angle. What should then be the physical realization of qubits ? It turns out that for qubits coded in the polarization or phase of single photons it is quite easy to keep track of the point on the Bloch sphere. Thus photons are ideal carriers of quantum information and they are used as such in quantum cryptography (see Chapter 8). For universal quantum computing the local qubit rotation must be supplemented with a two qubit gate as for example the conditional rotation used in QND schemes (see introduction). This gate is more easily implemented with qubits coded in massive particles (ions, atoms, solids,...) which can be engineered with strong mutual interaction. Thus it is evident that the photon-atom coupling plays an important role as an interface between the qubit carrier (photon) and qubit *memory* (ion, atom..). Such an interface has been realized experimentally in a cavity QED setting[85]. A Rydberg atom prepared in a superposition $|\psi\rangle_R = \alpha|g\rangle + \beta|e\rangle$ between the ground- and excited state is send trough a resonant microwave cavity carefully prepared in the vacuum state $|\phi\rangle_C = |0\rangle$. The (strong) atom-photon coupling is tuned to match a π-pulse such that the Rydberg- and cavity qubit are swapped : $|\psi\rangle_R \otimes |\phi\rangle_C = (\alpha|g\rangle + \beta|e\rangle) \otimes |0\rangle \Leftrightarrow \pi\text{-pulse} \Leftrightarrow |g\rangle \otimes (\alpha|0\rangle + \beta|1\rangle) = |\phi\rangle_R \otimes |\psi\rangle_C$. Note that the scheme is reversible, i.e. a second Rydberg atom (prepared in $|g\rangle$) can read out the qubit information stored in the microwave cavity. The cavity thus acts a quantum memory device with a lifetime close to 200 μsec.

In our experiment we also realize an atom-light interface but now for continuous quantum variables (the issue of implementing quantum algorithms for observables with continuous spectra is adressed in Ref.[81]). Let us focus on the quantum memory aspect for continuous variables. Ideally we should map both transverse Stokes components $S_{y,z}$ onto the collective spin components $J_{y,z}$. In the experiment we realize the unitary evolution $\hat{J}_y^{(out)} = \hat{J}_y^{(in)} + aJ_x\hat{S}_z$ (see 7.8) which suggest that only a single light quadrature S_z is mapped onto the atomic quadrature J_y. Furthermore it must be realized that S_y is continuously recorded 1 foot (1 nsec) after the atomic cell interaction region. In fact the atom-light interface acts like a beamsplitter and since we at least in principle record both S_y and S_z we could make infinitely many copies of the original Stokes vector but at the cost of a fidelity limited to below 1/2. To realize a continuous variable quantum memory with higher fidelity one should take full advantage of the beam splitter relation and use it to *teleport* the Stokes mode $S_{y,z}$ onto the atomic collective mode $J_{y,z}$[63]. The resources needed for this operation are EPR correlated atomic modes (for storing) and EPR correlated optical modes (for read-out). Clearly such schemes are experimentally quite involved, and the experimental results presented in this Chapter are only a preliminary step demonstrating the unitary beamsplitter operation $\hat{U} = \exp(-ia\hat{S}_z\hat{J}_z)$.

It must be stressed that teleportation is certainly not necessary to transfer the quantum state of one harmonic oscillator to a second. Take two degenerate oscillators described by the Hamiltonian $\hat{H} = \hbar\omega_0(\hat{a}_1^\dagger\hat{a}_1 + \hat{a}_2^\dagger\hat{a}_2)$. If we now introduce a linear coupling $\hat{V} = \hbar\kappa(\hat{a}_1^\dagger\hat{a}_2 + \hat{a}_1\hat{a}_2^\dagger)$ it is easy to show that the "excitation" oscillates periodically, i.e. $\hat{a}_j(t) = [\hat{a}_j(0)\cos(\kappa t) - i\hat{a}_k(0)\sin(\kappa t)]e^{-i\omega_0 t}$ where $j, k = 1, 2$. Thus after a period $t = \pi/2\kappa$ the initial quantum states of the two oscillators are *coherently* swapped. This is the continuous variable analogue of the qubit cavity memory discussed above. This system has been suggested for the vibrational modes of two trapped ions linearly coupled through their trap endcaps[24]. A more recent proposal suggest to couple a single optical mode (defined by a high finesse cavity) with the vibrational mode of single trapped atom/ion using Raman transitions[62]. This system would swap the quadrature statistics between the cavity field and the ion motion.

It is important to realize that quantum memory is not merely a toy for the future. It is already being experimentally implemented in ion trap architectures for scalable quantum computing[86]. In an ion trap the qubit is realized between two hyperfine groundstates which we can call spin up $|\uparrow\rangle$ and spin down $|\downarrow\rangle$. Any stray magnetic field rotates the qubit on the Bloch's sphere in an arbitrary uncontrolled direction leading to dephasing or decoherence. Now imagine coding the qubit into a two dimensional *decoherence free subspace* (DFS) spanned by two trapped ions : $\alpha|\uparrow\downarrow\rangle + \beta|\downarrow\uparrow\rangle$. If the two ions that span the DFS are very close they both see the same stray field and α and β both pick up the same phase shift leaving the DFS qubit unchanged. More precisely, if the magnetic field has a linear gradient over 10 cm and two ions separated by 10 μm traverse this gradient the dephasing of a DFS qubit is reduced by a factor of 10^4 as compared to a single ion qubit. The DFS can thus be seen as a robust quantum memory protecting the qubit from *collective* dephasing.

Another approach to quantum memory is based on the coherent optical information storage in atomic media using electromagnetically induced transparency[87]. At MIT the group of J. Shapiro have suggested an elaborate architecture for long distance quantum teleportation[88]. This system, which is technically quite challenging to implement, proposes to use single ^{87}Rb atoms confined by a CO_2-laser as quantum memory blocks. Each memory block is loaded by absorbing 795 nm photons from a polarisation entangled source based on periodically poled KTP. For long distance entanglement distribution the poling period is changed to create polarisation entangled pairs in the low loss telecommunication window at 1.55 μm. Finally a 5 cm long periodically poled lithium niobate (PPLN) crystal inside a cavity pumped with 0.5 W at 1570 nm is proposed to convert a 1608 nm flying qubit to a 795 nm memory qubit.

To briefly summarize this subject we can say that quantum memory has been experimentally demonstrated for discrete qubits and there exists several theoretical proposals for continuous variable memory. Our line of research approaches this subject through teleportation between harmonic oscillator modes while other approaches suggest to coherently swap oscillators with a linear coupling.

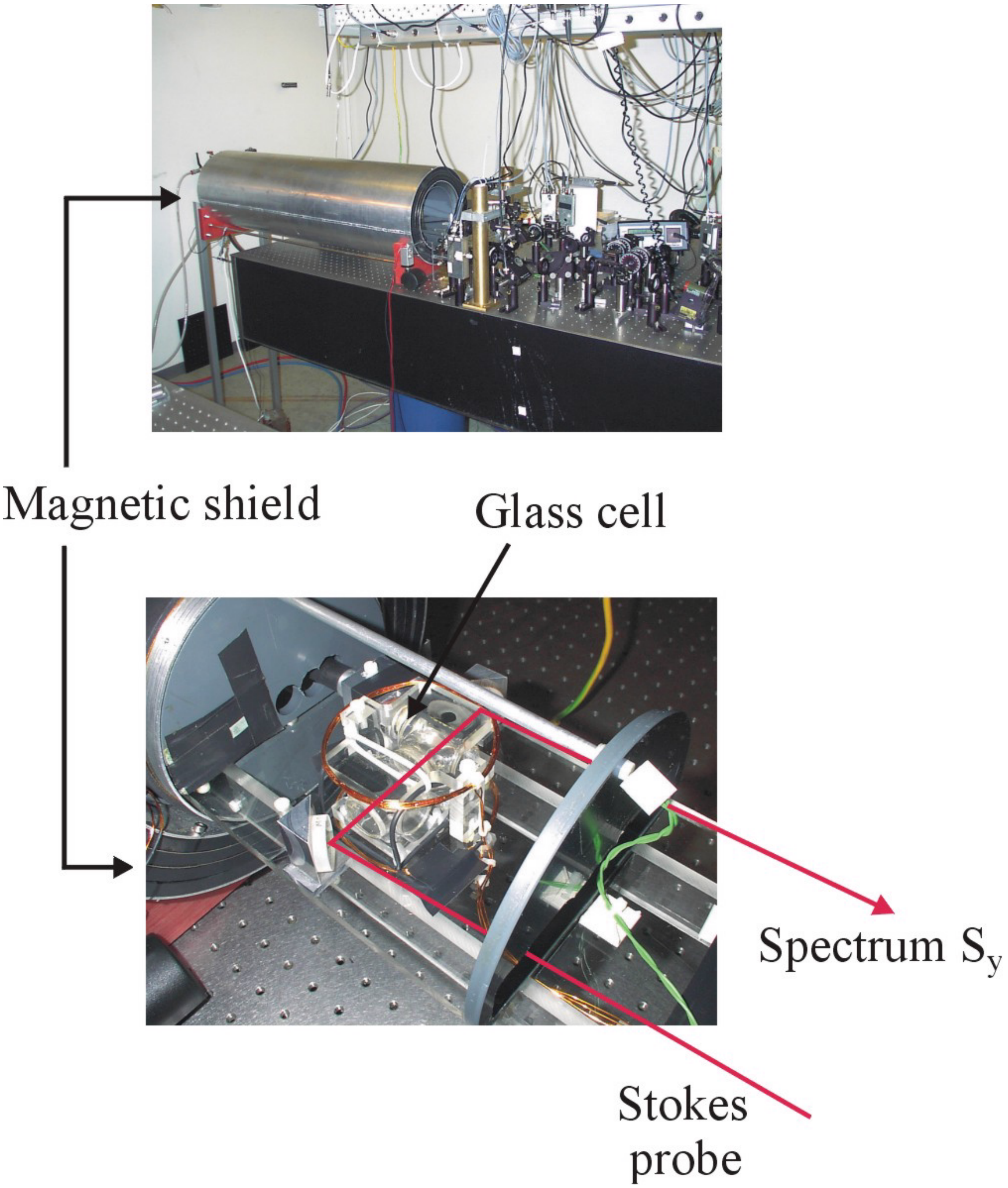

Figure 7.7: Pictures from the laboratory. Top : Magnetic shield used to isolate the cesium atoms from stray fields. Buttom : propagation of Stokes probe inside magnetic shield. The copper-wire above/below the glass cell generates the RF-field B_1 for magnetometry. The static field B_0 which defines the spin resonace (Larmor frequency Ω) derives from a solenoid co-axial with the magnetic shield.

Chapter 8

Quantum Cryptography

8.1 Introduction

In his book "Modern Quantum Mechanics" the author J.J. Sakurai points to the amusing fact that four Nobel Prizes where awarded to physicist who exploited the simple quantum mechanical two level system. Today, twenty years later, this system has earned the name qubit (for quantum bit) and it now forms the basic building block in our understanding and development of the emerging field of quantum information[89]. The simplest qubit application in this field is quantum cryptography (QC) with the goal to distribute a truly random and secret string of zeros and ones between two users Alice and Bob. The principle behind the security of QC is qubit projection noise, i.e the unavoidable perturbation introduced when the qubit measurement- and preparation-basis are conjugate or incompatible. The idea is simple : Alice and Bob *on purpose* introduce projection noise in a completely *random* subset of the distributed bit-string called the *raw key.* A posteriori classical communication allow them to identify and discard this subset. The remaining bit-string is called the *sifted key.* An eavesdropper (Eve) trying to extract information through measurement introduces additional projection noise in a *random and uncorrelated* subset of the raw key. Her presence is revealed when Alice and Bob check the sifted key for errors, i.e. they apply the basic logic

$$\text{error} \Rightarrow \ \text{measurement} \Rightarrow \ \text{eavesdropping} \tag{8.1}$$

and throw away the key. If on the other hand they find no errors in the sifted key they again apply the logic in Eq.(8.1) now with the word "no" infront and keep the key.

The basic idea of QC presented above was discovered almost twenty years ago but went unnoticed for nearly a decade[90]. Then during the last ten years the field developed rapidly and today it is standard material in many quantum mechanics courses. The first major review article has appeared[91], and the first commercial QC system is now available[1]. To appreciate the potential of QC as a future technology one must compare it against a classical public key cryptosystem such as RSA[2]. The RSA system derives its security from computational complexity. All public key cryptosystems operate with a mathematical object called a one-way function $f(x)$. The idea is that it is easy to compute $f(x)$ knowing x while the inverse operation is difficult. Here the word easy/difficult means that the time it takes to perform a task grows polynomially/exponentially with the number of bits in the input. RSA is based on the *unproven* assumption that factoring large numbers is a one-way function. However an overnight breakthrough in mathematics could prove this assumption wrong and instantly make electronic money worthless. In 1994 Peter Shor actually discovered an easy factoring algorithm on a quantum computer meaning that tomorrows technology (quantum computer) can reveal todays

---

[1] See www.idquantique.com

[2] RSA was developed in 1978 at MIT by Ronald Rivest , Adi Shamir, and Leonard Adleman. It is the most widely deployed public key cryptosystem today[89].

secrets (based on RSA encryption). QC closes this loophole since its security is based only on the laws of nature, i.e. projection noise or more precisely the Heisenbergs uncertainty principle. To avoid compromising this security Alice and Bob use todays only provable secure encryption scheme, the so-called Vernam cipher (proposed by Gilbert Vernam in 1926 at AT&T). Alice encrypts her message m with the sifted key k by simple binary addition $s = m \oplus k$ (binary addition $\oplus$ is also called XOR). The cipher s is send over a public channel to Bob who decrypts it with his copy of the sifted key, i.e. $s \oplus k = m \oplus k \oplus k = m$.

In 1998 we started construction of an experimental QC system and the following Chapter is aimed at covering this part of the authors Ph.D.-studies. The Chapter is structured to give a self-contained presentation of QC including the basic theory (section 8.2) and present-day technology in this field (section 8.3). Then in section 8.4 we describe our QC system in terms of a basic set of parameters by which we can identify present limitations and predict the impact on improved system components. Finally we summarize in section 8.5 and comment on recent results from other groups underlining the rapid development of QC which by now has evolved into an engineering science. We also use this section to re-establish contact with the field of continuous variables which is now playing an increasing role in the field of secure data transfer at least at the level of theoretical proposals.

8.2 Theory

We implement in our work the original quantum key distribution protocol called BB84[90] which is explained in subsection 8.2.1. Then in subsection 8.2.2 we discuss the relation between security and basic physics in the form of quantum noise governed by Heisenbergs uncertainty principle. The presentation and notation in this section follows the review article by Gisin *et al.*[91].

8.2.1 BB84 protocol

Since we are dealing with a communication application it is natural to implement the qubit in the polarisation state of single photon. Then by drawing the polarisation state on the Stokes sphere (Fig.8.1a) we can always generalize to an abstract spin 1/2 system on a Bloch sphere.

The BB84 key distribution protocol can now be explained as follows. Through a public channel Alice and Bob agree beforehand on the assignment of two classical binary numbers. The first is a basis-bit and its value 0 (1) selects a polarisation basis $\{|\rightarrow\rangle, |\uparrow\rangle\}$ ($\{|\nearrow\rangle, |\nwarrow\rangle\}$) in the equatorial plane (gray zone in Fig.8.1a). The second is a key-bit which determines the state within each basis as shown in Fig.8.1b. Alice now prepares a single qubit by supplying two binary numbers from a random number generator. The qubit is send through a quantum channel (optical fiber, free space,..) to Bob's side where its polarisation is measured. Bob uses an (independent) random number generator to supply a basis-bit which determines the basis for this measurement while the result is assigned to Bob's key-bit. In the next step Alice and Bob compare their basis-bit through the public channel (basis reconciliation). If identical they are certain that their (unrevealed) key-bits are identical. On the other hand, if the basis-bits do not match, the key-bits are completely uncorrelated due to projection noise and thus neglected. Repeating the qubit transmission sequence N times Alice and Bob distill a *random* subset of average length $N/2$ (*sifted key)* among the N key-bits (*raw key*). The following table shows a typical sample from the BB84 protocol

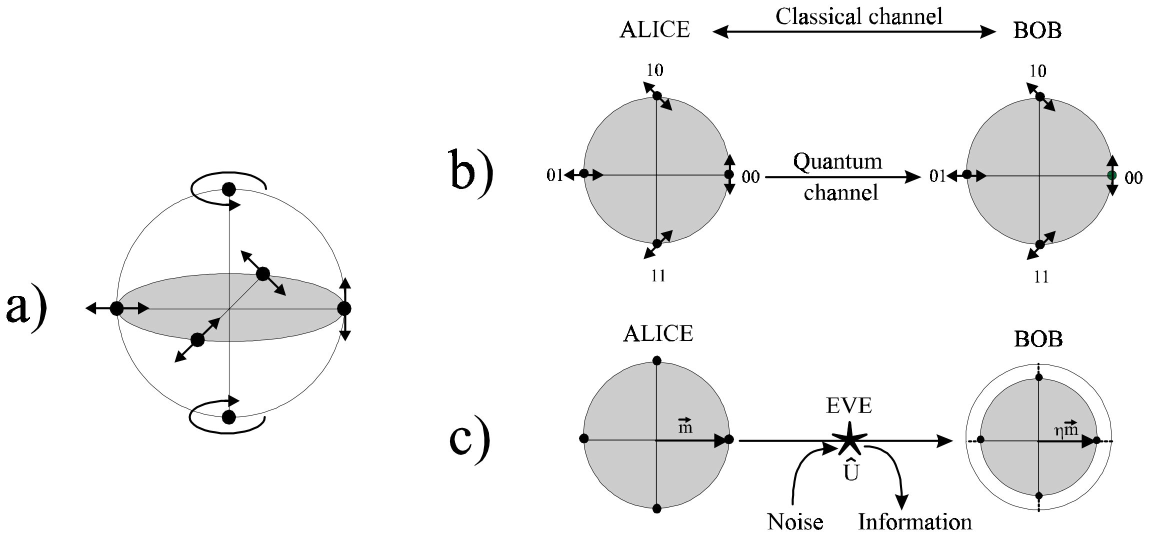

Figure 8.1: a) Polarisation state on the Stokes sphere. b) BB84 protocol with encoding in the equatorial plane of the Stokes sphere. The four qubit states are described by two classical bits. c) Eavesdropping on the quantum channel between Alice and Bob. Eve extracts information at the cost of introducing noise.

Alice base-bit	0	1	1	0	1	1	0	0	1
Alice key-bit	1	0	1	0	1	0	1	1	1
Qubit coding	$\vert\longrightarrow\rangle$	$\vert\nwarrow\rangle$	$\vert\nearrow\rangle$	$\vert\uparrow\rangle$	$\vert\nearrow\rangle$	$\vert\nwarrow\rangle$	$\vert\longrightarrow\rangle$	$\vert\longrightarrow\rangle$	$\vert\nearrow\rangle$
Bob base-bit	1	1	0	0	1	1	1	0	0
Bob key-bit	1	0	1	0	1	0	0	1	0
Raw key	1	0	1	0	1	0	0	1	0
Reconciliation	%	√	%	√	√	√	%	√	%
Sifted key	–	0	–	0	1	0	–	1	–

Other QC protocols developed since BB84 can be divided into two classes. The first is based on different encodings of the qubit including the two-state[92] and six-state protocol[93]. The second involves protocols where the qubit is replaced by higher dimensional quantum systems[94],[95]. In principle the quantum part of any QC protocol is covered by the raw key generation over the quantum channel. Everything beyond this stage including reconciliation, error correction and privacy amplification (see below) proceed over the classical public channel. But quantum physics also plays an essential role in providing unconditional security. This aspect of QC is an intriguing one since it involves the theory of measurement which lies at the heart of quantum mechanics.

8.2.2 Security in BB84

Consider again the BB84 protocol shown in Fig.8.1c where we have added the eavesdropper Eve. Alice prepares a qubit along the unit vector $\mathbf{m}$ which we describe by the density matrix

$$\hat{\rho}_A = \frac{1 + \mathbf{m}\hat{\boldsymbol{\sigma}}}{2} \tag{8.2}$$

Here the Pauli matrix components of $\hat{\boldsymbol{\sigma}}$ describe a general spin 1/2. Eve is going to extract information about $\hat{\rho}_A$ and at the same time introduce noise into the quantum channel. To set the stage we limit

Eve's power to *individual attacks* : (i) she can entangle each qubit send by Alice with a probe $\hat{\rho}_E$ (arbitrary dimension) using the rules of quantum mechanics, i.e. a unitary operator $\hat{U}$, and (ii) she can only measure probes individually but she is allowed to postpone her measurement until after the basis reconciliation between Alice and Bob. In addition we assume that Eve's attack is *symmetric* such that she introduces the same amount of noise into the two conjugate basis used by Alice and Bob. In this case Bob receives each qubit with a density matrix $\hat{\rho}_B$ related to $\hat{\rho}_A$ by a simple shrinking factor $\eta \in [0,1]$ (see Fig.8.1c)

$$\hat{\rho}_B = Tr_E \left[\hat{U}(\hat{\rho}_A \otimes \hat{\rho}_E)\hat{U}^\dagger\right] = \frac{1+\eta\mathbf{m}\hat{\boldsymbol{\sigma}}}{2} \tag{8.3}$$

The presence of Eve is revealed by the reduced fidelity between Alice and Bob $\mathcal{F}$ =Tr$[\rho_A\rho_B] = (1+\eta)/2$. Thus a fraction $\mathcal{D} = 1-\mathcal{F}$ of the bits in the sifted key are wrong, i.e. flipped. This fraction is called the *quantum bit error rate* QBER and it is an essential parameter for any security statement. Alice and Bob estimate the QBER by comparing a random subset of the sifted key over the public channel. In any realistic implementation of QC there will always be errors in the sifted key caused by dispersion in the quantum channel, detector dark counts etc. But Alice and Bob have to assume that *any* nonzero QBER is caused by Eve. Thus there is *always* eavesdropping (nonzero QBER) and the essential question is whether there exists a threshold QBER=$\mathcal{D}_0$ below which Alice and Bob can still obtain a secure key by applying some classical protocol to the sifted key. As we shall see the answer is yes and the magic number $\mathcal{D}_0$ is pulled out of the hat by combining two basic theorems.

The first theorem derives from a translation of Heisenbergs uncertainty relation into an information exclusion principle[96]. It puts an upper bound on the sum of information $I_{AB} + I_{AE}$ on Alice's key available to Bob and Eve. Here $I_{AB} = H_i - H_f$ is Bob's information gain defined as the difference between the Shannon entropy in the initial and final state[97]. The Shannon entropy describes Bob and Eve's ignorance of Alice's state $\hat{\rho}_A$ through the entropy function

$$H = -\sum_r p_r \log(p_r) \tag{8.4}$$

Before any measurement the density matrix $\hat{\rho}_A$ averaged over Alice's random preparation is just the identity. Thus Bob and Eve's initial Shannon entropy is maximal $H_i = -\sum \frac{1}{2}\log(\frac{1}{2}) = 1$. If Eve does not interfere with the key exchange ($\eta = 1$) she stays ignorant $H_f = 1$ and her information gain is zero $I_{AE} = 0$. At the same time Bob's fidelity $\mathcal{F} = (1+\eta)/2 = 1$ and the zero QBER $\mathcal{D} = 1-\mathcal{F} = 0$ leaves him with full information on Alice's qubit $H_f = 0$ and unity information gain $I_{AB} = 1$. In the general case Eve perturbs the quantum channel ($\eta < 1$) and introduces a nonzero QBER which reduces Bob's information gain

$$I_{AB} = 1 - \mathcal{D}\log(\mathcal{D}) - \mathcal{F}\log(\mathcal{F}) = 1 - \mathcal{D}\log(\mathcal{D}) - (1-\mathcal{D})\log(1-\mathcal{D}) \tag{8.5}$$

I_{AB} is shown in Fig.8.2a as a function of the QBER $\mathcal{D}$ (solid curve). Note that for $\mathcal{D} = 1/2$ we have $I_{AB} = 0$ which is quite reasonable : if on average every second bit in the sifted key is wrong Bob must assume that his key is completely uncorrelated with Alice's key and consequently his information gain is zero. Now the information exclusion principle (Heisenbergs uncertainty relation) bounds Eve's information gain I_{AE} once Alice and Bob have determined the QBER $\mathcal{D}$ and $I_{AB}(\mathcal{D})$.

Theorem 1. Information exclusion principle : $I_{AB} + I_{AE} \leq 1$

The second basic theorem is a mathematical result from classical information based cryptography. Given I_{AB} and I_{AE} it states the necessary and sufficient conditions to extract a secret key by applying error correction and privacy amplification to the sifted key[98].

Theorem 2. Error correction and privacy amplification is possible if and only if : $I_{AB} \geq I_{AE}$[3].

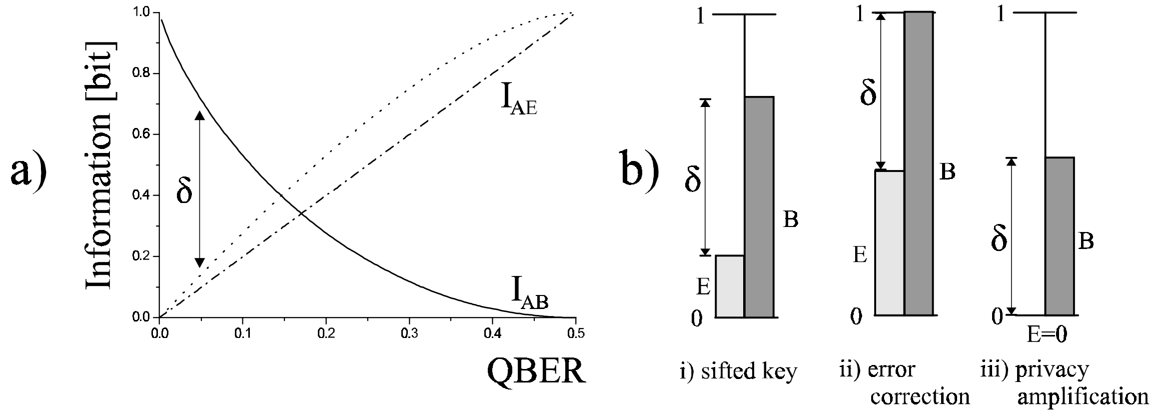

Figure 8.2: a) Shannon information versus quantum bit error rate QBER. The dotted curve is Eve's information gain for the *optimal individual attack* which is compared with the more realistic *intercept-resend* strategy (dash-dot curve) b) illustration of Theorem 2 : when $\delta = I_{AB} - I_{AE} > 0$ Alice and Bob can use error correction and privacy amplification to extract a completely sectret key (E=0). Note that the effective key distribution rate scales with δ.

Theorem 2 is (probably) hard to prove but quite intuitive as shown in Fig.8.2b. When combined with theorem 1 it leads to the bound $I_{AB} \geq 1/2$ which, when inserted into Eq.(8.5), returns the threshold $\mathcal{D}_0 = 11\%$ (see Fig.8.1a). If Alice and Bob measure $\mathcal{D} \leq 11\%$ they can establish a cryptographic key whose security is based on the laws of nature (Heisenbergs uncertainty relation plus a mathematical result). It must be stressed that $\mathcal{D}_0$ is only a *sufficient* threshold. An interesting question is whether Eve can saturate the exclusion principle at the threshold $\mathcal{D}_0$, i.e. can she find a unitary operator $\hat{U}$ such that $I_{AB} = I_{AE} = 1/2$? This turns out to be impossible when Eve is restricted to the class of symmetrical individual attacks defined above. The optimal information gain I_{AE} that Eve can obtain in this case is calculated in Ref.[99] and shown in Fig.8.2a (dotted curve). From the cross point $I_{AB} = I_{AE}$ we obtain the *necessary* threshold $\bar{\mathcal{D}}_0 \approx 15\%$ for protection against any individual attacks on the BB84 protocol.

The discussion so far has indeed been quite generous towards Eve. She can implement an arbitrary coherent evolution between two quantum systems and she can store her quantum probe and wait reading it until after the basis reconciliation phase. Let us see how the more realistic Eve performs in comparison by limiting her strategy to *intercept-resend* : (i) using the same basis as Bob, Eve performs a direct measurement on a fraction f of the qubits send by Alice, and (ii) at every intercept she re-sends a photon to Bob in the same state she measured. On average Eve picks the correct basis on half the intercepts and thus her information gain is $I_{AE} = f/2$. Whenever she picks the wrong basis she will introduce an error in the sifted key with 50% probability, i.e. $\mathcal{D} = f/4$. The resulting curve $I_{AE} = 2\mathcal{D}$ is shown in Fig.8.2a (dash-dot curve). The new crossing at $\bar{\mathcal{D}}_0 \approx 17\%$ clearly demonstrates that Eve only gains marginally by replacing todays technology by futuristic toys like quantum memory. As a final remark we point out the (minimal) cost of error correction and privacy amplification on the key generation rate. If Alice and Bob generate the sifted key at a rate R_{sift} then the bits revealed on the public channel during error correction and privacy amplification reduce this rate according to $\bar{R}_{sift} \leq R_{sift}(I_{AB} - I_{AE}) = R_{sift}\delta$ (see Fig.8.2b).

---

[3] For simplicity we assume $I_{AE} = I_{BE}$ througout. When this is not true theorem 2 should read : $I_{AB} \geq I_{AE}$ or $I_{AB} \geq I_{BE}$.

8.3 QC technology

8.3.1 Qubit source - faint laser pulse

The optimal information carrier is the photon in which we typically code the qubit in polarisation or phase (see below). Ideally we want a *photon gun* for QC, i.e. a practical device which when triggered emits one (and only one) photon into a well defined mode such as an optical fiber. The photon gun is not on the market yet, but several groups are working on prototypes/proof of principles. A good candidate is the nitrogen-vacancy center in diamond since it is stable at room temperature. When pumped with 532 nm laser light the re-emitted fluorescence (700 nm) exhibits strong photon antibunching[100],[101]. The challenge of capturing the fluorescence photon still remains (0.1 % efficiency at the moment). The 700 nm wavelength is ideal for single photon detection but there is no optimal quantum channel at this wavelength (see subsection8.3.2).

Without the ideal photon gun in the belt experimentalists today mimic the single photon by using faint laser pulses from diode lasers. This is actually a quite good solution even though the Fock state distribution with its single peak at photon number $n = 1$ looks quite different compared to the weak pulse Poisson distribution

$$P(n, \mu) = \frac{\mu^n}{n!} \exp(-\mu) \tag{8.6}$$

The argument is that with average photon number $\mu << 1$ in each pulse the probability to have more than one photon in any non-empty pulse is very low

$$P(n > 1 \mid n > 0, \mu) \simeq \mu/2 \tag{8.7}$$

There is an ongoing debate about the potential security loophole caused by the fraction of pulses with 2 or more photons[102],[103],[104]. It is argued that Eve in principle could use a photon number QND detector to identify this fraction. She would then split off a single photon, store it in a quantum memory and read it only after basis reconciliation and obtain maximal information gain $I_{AE} = 1$. Let us point out that "splitting off 1 photon" with average probability $1 - (1/2)^n$ takes n beamsplitters (50/50) and $2n$ QND detectors. Even though QND detection at the single photon level has been demonstrated in Ref.[74] the efficiency is low and the technology not suited for tapping an optical fiber. With these technical challenges (including the need for quantum memory) it is safe to argue that the photon gun will close this security loophole long time before it ever becomes a serious treat. If we take this approach then the faint pulse laser source behaves as a photon gun with a low efficiency $P(n = 1, \mu) = \mu$. In principle the high modulation rate possible with laser diodes could compensate this low efficiency. But detector dark counts caused by afterpulsing (see subsection8.3.2) limit the pulse repetition rate f_{rep} to a few MHz. The final important parameter of the qubit source is the operating wavelength. This is set by the choice of quantum channel and detector.

8.3.2 Quantum channel and single photon detection

The quantum channel should guide the qubit (photon) from Alice to Bob while protecting it against decoherence. The waveguide at optical frequencies is the optical fiber. Propagation along a guide with transverse index profile $n(x, y)$ is usually described by the slowly varying envelope approximation to the Helmholtz equation. The resulting equation turns out to be identical to the Schrödinger equation with a potential $V(x, y) = -n(x, y)$. If the width of the index step is small enough (core of a few wavelengths) the fiber only supports a single mode (SM) and it protects the qubit (photon) from decoherence. Currently telecommunication fibers are manufactured close to the so-called "clarity limit" where absorption is limited by Rayleigh scattering and infrared absorption in SiO_2[105]. In Fig.8.3a we show the different contributions to the fiber attenuation [dB/km] versus wavelength. This graph should be correlated with the performance of avalanche photodiodes (APD) used for single photon counting (see Fig.8.3b and discussion below).

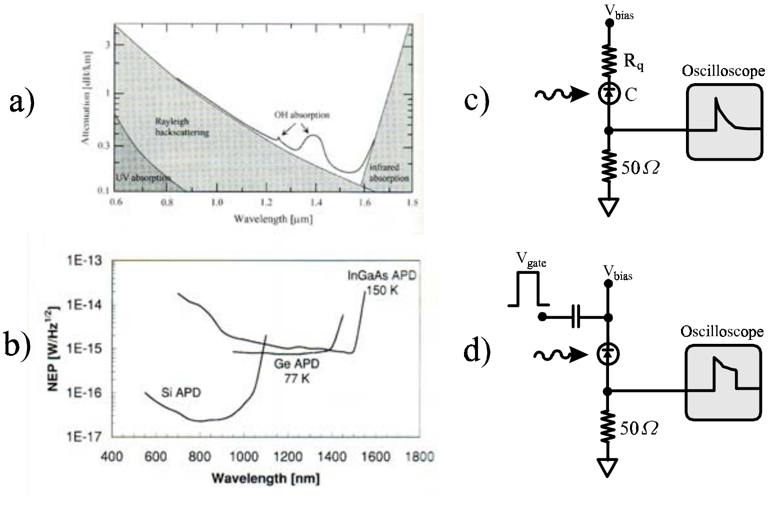

Figure 8.3: a) Attenuation in optical fiber as a function of wavelength. b) Noise equivalent power (NEP) for silicon, germanium, and InGaAl/InP APD's in the same wavelength window. c) APD operated in Geiger mode with passive quenching circuit. d) APD operated in gated mode. The gate is typically a few nanoseconds wide and activated when a photon is expected to arrive.

At 800 nm silicon APD's operated in *Geiger mode* outperform photomultipliers. In this mode the applied reverse bias voltage exceeds the breakdown voltage and a single photon absorption can trigger an electron avalanche with probability equal to the quantum efficiency η of the device. The avalanche persists until quenched by reducing the field strength in the diode junction below the break down point[106]. Fig.8.3c shows a simple *passive quenching* circuit where the voltage drop over a large serial quench resistor R_q (50-500 kΩ) brings the bias below breakdown as soon as the avalanche starts. The detector dead time is set by charging of the diode capacity C (timeconstant R_qC) which takes the bias back across the breakdown point. Avalanches are also triggered by thermal excitation leading to a dark count rate R_{dark}. As a point of reference the commercial silicon APD from EG&G (SPCM-AQ-151) performs with $\eta = 60\%$ (800 nm), maximum count rate >5 MHz, and $R_{dark} = 50$ Hz (-20°C). In QC the detector figure of merit is the ratio of darkcounts to quantum efficiency. However the literature typically quotes the noise equivalent power (NEP) which shows similar behavior

$$\text{NEP}=\frac{h\nu}{\eta}(2R_{dark})^{1/2} \tag{8.8}$$

Fig.8.3b plots the NEP of silicon, germanium and InGaAs/InP APD used for single photon counting. While the silicon APD in Geiger mode offers an almost perfect photon counting solution an apparent drawback is the high optical fiber attenuation in the window from $0.6 - 1$ μm. But it turns out that free space has a high transmission window near 770 nm. This has lead to experiments in free space QC with distances up to 1.6 km at daylight[107] and 1.9 km at night conditions[108]. The optical depth encountered in Ref.[107] is close to the effective depth encountered in a surface-to-satellite transmission which opens up the possibility of QC over arbitrary distances. In short, Alice and Bob independently establish secret keys k_A and k_B with a *trusted* satellite. The satellite broadcasts in public the sum $K = k_A \oplus k_B$ and Bob infers Alice's key by subtracting his own $k_A = K \oplus k_B$[4]. A final remark regarding free space QC is the isotropy of the sky and hence lack of birefringence and polarisation rotation.

---

[4] Governments might even favour this scheme of QC since they are likely to control the satellite and hence communication (the *Echelon* project could continue!).

For earthbound systems the transmission windows at 1.3 μm and 1.55 μm are are good candidates for a QC link. Unfortunately the energy gap in silicon cuts off these wavelengths and one has to resort to other materials such as germanium and InGaAs/InP. As shown in Fig.8.3b APD's constructed with these materials perform inferior to silicon. They are cooled to very low temperatures to reduce darkcounts and this increases the lifetime of trapping centers in the diode junction. If the lifetime approaches the deadtime of the detector then trapped carriers from a primary avalanche can trigger a secondary. This process is called *afterpulsing* and it effectively rules out passive quenching in InGaAs/InP. The solution is to operate the APD in *gated-mode* which is shown in Fig.8.3d[109]. Here the bias voltage is kept below threshold and a short gate (few ns) activates the Geiger-mode. This mode of operation is well suited for QC since the photon arrival time is known in advance, but note that gate repetition rate is limited by the lifetime of trapped carriers. The first commercial APD based on InGaAs/InP was introduced only recently[5]. Depending on the bias/gate voltage this device operates from $\eta = 5\%$ and $R_{dark} = 10$ kHz up to $\eta = 30\%$ at $R_{dark} = 1$ MHz. Also Hamamatsu this year introduced an InGaAs/InP photomultiplier, but they only promise $\eta > 0.3\%$ with $R_{dark} = 200$ kHz. Although single photon detection above 1 μm still suffers from low quantum efficiency and high dark count rates it is reasonable to expect improvements in the near future. The existence of installed fiber networks in both the second/third telecommunication window (1.3/1.5 μm) in combination with APD detectors has already allowed researches to explore and demonstrate QC prototypes outside the laboratory[110]. The experiment in Ref.[110] used polarisation as qubit encoding of photons send over a 23 km phone conversion fiber between the Swiss cities Nyon and Geneva. This experiment demonstrated the problems associated with birefringence in fibers which cause polarisation rotation and basis misalignment between Alice and Bob. If the polarisation rotation is slow it is in principle possible to compensate with active feedback[111], but research in this direction has not been pursued. Instead the next generation of experiments replaced the polarisation coding with phase coding[112],[113].

8.3.3 Polarisation- versus phase coding

In Fig.8.4a we show again BB84 with qubit polarisation encoding in the equatorial plane of the Stokes sphere. For free space QC the absence of birefringence in air leaves the coding plane invariant. On the other hand the (random) residual stress in SM fiber manufacturing introduces a birefringence vector **b** in the equatorial plane. This vector causes a rotation $\exp(-i\mathbf{b}\boldsymbol{\sigma}/2)$ and thus misalignment of the coding plane also shown in Fig.8.4a. Note that **b** also has a small component perpendicular to the equatorial plane due to a nonzero Verdet constant of SiO_2. It is interesting to note that the circular birefringence may also have a contribution from the Berry's phase related to the purely *geometric* winding of the fiber on a spool[114]. **b** has three components and the basis misalignment can thus be compensated by three waveplates ($2\times$ $\lambda/4$ plus $1\times\lambda/2$) realized by stress induced birefringence in three fiber loops (see Fig.8.4a). Mechanical and thermal fluctuations in real fiber networks randomly change **b** and this prompted researchers to look for alternative ways to code a qubit in a photon.

The solution is called phase coding and is shown in Fig.8.4b. The north- and south pole of the Blochs sphere are now represented by the presence of a photon in either of two spatial modes $|p_1\rangle$ and $|p_2\rangle$ and the relative phase φ between (equal) mode amplitudes describes the equatorial coding plane. The coding/measurement of φ is implemented with a Mach-Zehnder interferometer shown in Fig.8.4c. Alice uses a 50/50 beamsplitter (BS1) to take the interferometer into the equatorial coding plane. Then with her base- and key bit she randomly prepares one of the four BB84 qubits $\varphi_A = 0, \pi/2, \pi, 3\pi/2$ using a phasemodulator (PM_A). Bob uses his random basis bit to rotate the coding plane by $\varphi_B = 0,\ \pi/2$ (PM_B) and his beamsplitter (BS2) brings the interferometer back along the north-south pole. Finally Bob assigns his key-bit the value 0 (1) if he detects the photon in path $|p_1\rangle$ ($|p_2\rangle$). In short, Alice and Bob agree on the following coding scheme ("?" occurs when Alice and Bob have different basis-bits)

---

[5] id Quantique: www.idquantique.com

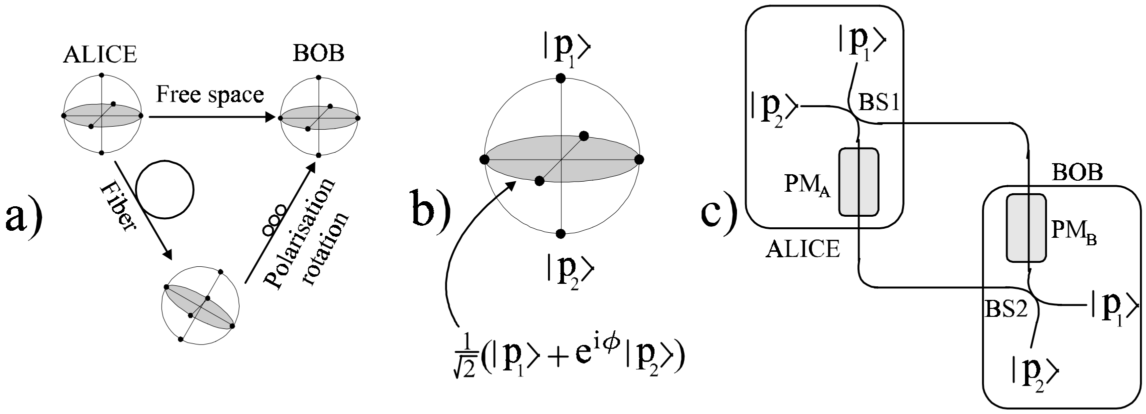

Figure 8.4: a) Residual birefringence in optical fibers leads to rotation of the coding plane in BB84. Bob can compensate this effect by using polarisation rotators. Alternatively Alice can transmit photons in free space which is isotropic. b) Phase coding : the qubit is a single photon in superpostion between two spatial modes. c) BB84 protocol where the phasecoding and readout is implemented with a Mach-Zehnder interferometer.

Bob\Alice	0	$\pi/2$	π	$3\pi/2$
0	0	?	1	?
$\pi/2$	?	0	?	1

Basically Alice and Bob each control the length of one interferometer arm. The relative length between these arms (i.e. the phase φ) should be stabilized to a fraction of a wavelength while the QC link should be as long as possible (>10-20 km). This technical challenge is overcome by the ingenious setup shown in Fig.8.5a and demonstrated in Ref.[112]. In this setup the 50/50 beamsplitter BS plays the role of both BS1 and BS2. Bob's interferometer arm can be traced on the Stokes sphere as shown in Fig.8.5b : From point A via the the short arm, polarizing beamsplitter (PBS), and optical fiber (with birefringence) to point B; Inversion to point C via Faraday mirror (FM); then via optical fiber to point D orthogonal to A; and finally via long arm back to point A. Alice's interferometer arm is simply the exact reverse path on the Stoke's sphere. There are several important remarks about this setup : (i) The length of the two interferometer arms is identical since fiber fluctuations are slow compared to the time it takes a photon to travel from BS to FM and back, (ii) both interferometer arms start and end in the same polarisation state at BS, and (iii) at point C they are separated in time by an amount $\tau = nL/c$ where L =(long arm)-(short arm), $n = 1.5$ is the refractive index of glass-fiber, and c is the speed of light in vacuum. The automatic length- and polarisation alignment (i,ii) motivated the name "plug and play" interferometer for the setup in Fig.8.5a. The time-multiplexing (iii) is used by Alice to apply the phase φ_A only to her arm of the interferometer (see next section). The quality of the auto-alignment is characterized the visibility V of the of the interferometer.

The original "plug and play" setup from 1997[112] used an ordinary beamsplitter in place of the polarizing beamsplitter PBS shown in Fig.8.5a. Even though the visibility was very high ($V = 0.998$) multiple reflections caused spurious pulses in the interferometer and the repetition rate was limited to 1 kHz. In the beginning of 1998 we proposed to introduce the PBS and started construction of a QC link[6]. The next section describes our results which are published in Ref.[104].

---

[6] The same year (october) the Geneva group published a paper where they had already implemented the PBS[115].

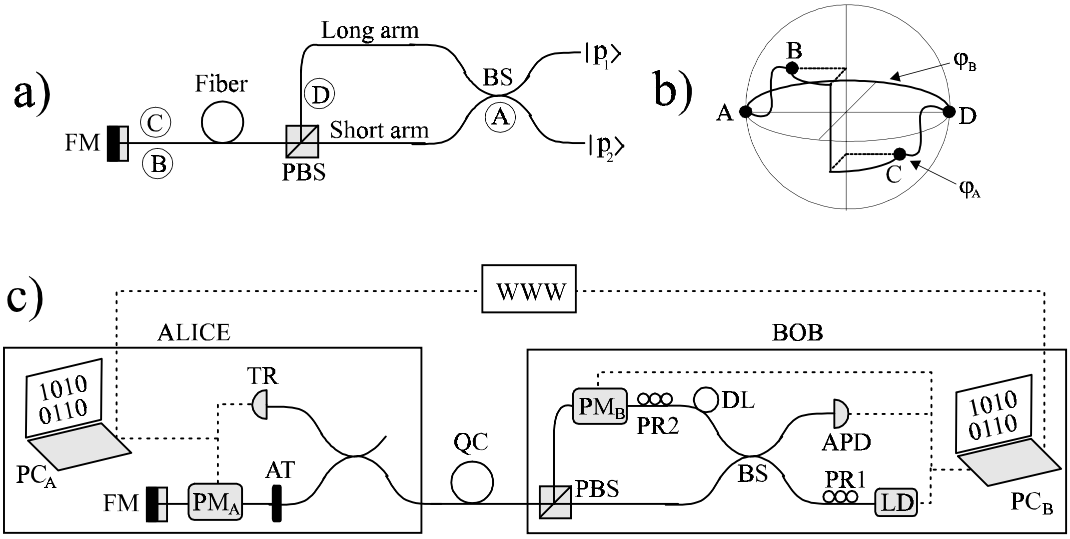

Figure 8.5: a) "Plug&play" interferometer with automatic length- and polarisation alignment. b) Stokes sphere track of interferometer arms : Bob=ABCDA and Alice=ADCBA. c) Experimental version of plug&play : LD=laser diode; PR=polarisation rotator; BS=50/50 beamsplitter; PBS=polarisation beamsplitter; QC=quantum channel; Tr=classical trigger detector; AT=attenuator; FM=Faraday mirror; PM$_j$=phase modulator; DL=delay line; APD=avalanche photodiode; WWW=internet; solid curve=optical fiber; dotted curve=classical communication wire.

8.4 Experimental "plug and play" QC

We have build an all fiber-optic plug and play interferometer according to the schematic in Fig.8.5a. To close the loop on the Stokes sphere we need several fiber optic elements which are explained in subsection 8.4.1. Then in subsection 8.4.2 we list the key parameters for out setup which we use in subsection 8.4.3 to calculate the QBER as a function of the quantum channel length. From this dependence we derive the maximum distance for secure key distribution between Alice and Bob. We end this section with a brief comment on a public demonstration of our system implementing classical communication over the internet (subsection 8.4.4).

8.4.1 Basic interferometer elements

In Fig.8.5c we show the more detailed plug&play system that we have build in the laboratory. In the following we briefly explain the action of each fiber-optic component that connect the points on the track in Fig.8.5b. Bob initializes the interferometer with a strong coherent pulse from a pigtailed laser diode LD (Fujitsu). The spreading of the pulse (1ns) is reduced to a minimum by working at the zero dispersion wavelength 1.3 μm, i.e. all fiber-optic components are tailored to this wavelength. The homebuild polarisation rotator PR1 prepares the input state A. The second rotator PR2 connect points A and D. Points A and B (C and D) are connected by 20 km of standard telecommunication single mode fiber (QC). Finally points B and C are connected by a Faraday mirror (FM). We insert a delay line (DL) of length $L = 150$ m such that Alice and Bob cross point C with a delay $\tau = 750$ ns. This delay enables Alice to control the phase φ_A in her arm by activating a travelling waveguide modulator PM$_A$(Pilkington) after receiving a trigger signal (TR). Similarly Bob controls the phase φ_B in his arm by activating the phasemodulator PM$_B$ (Uniphase) between points D and A. The phase coding by Alice and Bob is shown on the Stokes sphere in Fig.8.5b. Monitoring the interferometer output with a classical detector we observe a high fringe contrast ($V = 0.995$) when varying either φ_A or φ_B continuously.

8.4.2 QC parameters

For QC application we insert a calibrated attenuator (AT) and return the pulse from Alice to Bob with mean photon number $\mu = 0.1$. The output from the interferometer is now detected by a homebuild single photon counter using an InGaAs/InP APD cooled to -150°C and operated in gated-mode. The gate width is 1.1 ns (FWHM) and we apply a bias voltage of 30.3 V and a gate voltage of 2.0 V. With these settings we measure the quantum efficiency $\eta = 0.1$ and dark count rate $R_{dark} = 410$ kHz. The probability to observe a dark count in a single gate (1.1 ns) is then $p_{dark} = 4.5 \times 10^{-5}$. There is an apparent flaw with the setup in Fig.8.5c since we only monitor one interferometer output. Even though Bob uses a random bit to select the basis ($\varphi_B = 0, \pi/2$) he always measures the same state within each basis and the sifted key is deterministic. The obvious solution is to combine LD with a circulator and a second APD to also monitor this output arm of the interferometer[115]. Instead we keep a single detector in our setup but switch *randomly* between the two states in each basis. This is realized by Bob applying an additional phase $0/\pi$ according to a random *state*-bit 0/1. This scheme corresponds to having two detectors with average quantum efficiency $\eta/2 = 0.05$. We observe an additional 4 dB loss in Bob's fiber optic system (mainly due to PM$_B$) which we include in the effective quantum efficiency $\bar{\eta} = 10^{-0.4}\eta/2 = 0.02$.

The quantum channel is characterized by its transmission $t_{link} = 10^{-(l\alpha/10)}$.Here l is the length of the quantum link and α is the attenuation (in dB) per unit length. For our system we measure $l\alpha = 6.6$ dB close to the expected value for $l = 20$ km and $\alpha \simeq 0.35$ dB/km (1.3 μm). The visibility is identical to that measured with classical pulsed, i.e. $V = 0.995$. The final parameter we need is the repetition rate $f_{rep} = 70$ kHz.

In summary, we characterize our QC setup by the following parameters. (i) source : f_{rep} and μ, (ii) quantum channel : t_{link}, (iii) detector : $\bar{\eta}$ and p_{dark}, (iv) interferometer : V. In the next section we use these parameters to calculate the QBER and the effective key rate $\bar{R}_{sift}$ after error correction and privacy amplification.

8.4.3 QBER and effective secret key rate

When Alice and Bob compare a random subset of the sifted key they get an estimate of the QBER which is the ratio of wrong bits to the total number of bits

$$\text{QBER} = \frac{N_{wrong}}{N_{right} + N_{wrong}} = \frac{R_{error}}{R_{sift}} \tag{8.9}$$

The second equality expresses the QBER as the ratio of two rates R_{error} and R_{sift}. Here R_{sift} is simply the raw key rate reduced by a factor or two due to incompatible bases choices between Alice and Bob

$$R_{sift} = \frac{1}{2} f_{rep} \mu t_{link} \bar{\eta} \tag{8.10}$$

The error rate R_{error} has two sources. The first R_{opt} derives from the imperfect interference contrast ($V < 1$) whereby a photon ends up in the wrong detector with probability p_{opt}. It scales with R_{sift} and thus contributes a constant fraction to the QBER independent of the length of the quantum channel

$$\text{QBER}_{opt} = \frac{R_{opt}}{R_{sift}} = \frac{R_{sift} p_{opt}}{R_{sift}} = \frac{1-V}{2} \tag{8.11}$$

The second source R_{det} derives from the probability p_{dark} of a dark count in the detector during the gate

$$\text{QBER}_{\text{det}} = \frac{R_{\text{det}}}{R_{sift}} = \frac{\frac{1}{2}\frac{1}{2} f_{rep} p_{dark}}{R_{sift}} = \frac{p_{dark}}{2\mu t_{link} \bar{\eta}} \tag{8.12}$$

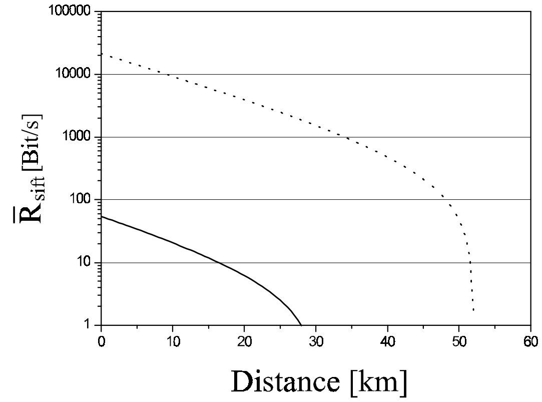

Figure 8.6: Effective key rate versus length of quantum channel. Solid curve shows the performance of our setup with : $f_{rep} = 70$ kHz, $\mu = 0.1$, $\alpha = 0.35$ dB/km, $p_{dark} = 4.5 \times 10^{-5}$, $\bar{\eta} = 0.02$, and $V = 0.995$. The dotted curve shows the predicted performance with commercial available peltier cooled InGaAs/InP APD's : $p_{dark} = 2 \times 10^{-5}$, $\bar{\eta} = 0.05$, and $f_{rep} = 10$ MHz (μ, α, and V unchanged).

Here the two factors 1/2 reduce the effect of p_{dark} since there is 50% chance that a dark count appeared "outside" the sifted key while a dark count appearing in the sifted key has 50% chance of being correct. The important point is the exponential scaling of QBER$_{\text{det}}$ with the length of the quantum link ($t_{link}^{-1} = 10^{(\alpha l/10)}$). It is detector noise which eventually limits the transmission distance since it increases QBER to a point where $I_{AE} = I_{AB}$ and the effective key rate is zero

$$\bar{R}_{sift} = R_{sift}(I_{AB} - I_{AE}) \tag{8.13}$$

To see this more clearly we plot in Fig.8.6 $\bar{R}_{sift}$ against the distance of the quantum link. Initially the key rate drops exponentially like the transmission until $I_{AE} \approx I_{AB}$ and the cost of error correction plus privacy amplification rapidly brings it down to zero. We assume that Eve uses the optimal individual attack in which case $\delta = I_{AB} - I_{AE}$ as a function of QBER can be read off Fig.8.2. The solid curve in Fig.8.6 is the maximal secure key rate possible with the parameters of our experiment. With a 20 km quantum channel we produce around 10 secure bits per second! This can be improved substantially by reducing the detector figure of merit $p_{dark}/\bar{\eta}$ along with increasing the repetition rate f_{rep}. By using two commercial peltier cooled InGaAs/InP APD (id Quantique) we would have $p_{dark} = 10^{-5}$ (1 ns gate) and $\bar{\eta} = 0.05$ (we assume that we can eliminate the 4 dB excess loss in Bob's equipment). More importantly the higher operating temperature of the APD will reduce the effect of afterpulsing and we can increase f_{rep} to say 10 MHz. These improvements correspond to the dotted curve in Fig.8.6 where we observe an increase in both the key rate and the maximum secure distance.

8.4.4 Prototype key distribution over the internet

The QC project is a joined effort between our group and the computer science department at the university. While we developed the hardware for distributing the raw key, the computer scientists developed a software packet 'QuCrypt'[7] for internet based classical communication between Alice and Bob. QuCrypt handles (i) basis reconciliation, (ii) QBER estimation, (iii) error correction, and (iv) privacy amplification. In December 2000 we demonstrated this prototype QC link between two

---

[7] Written by Louis Salvail and Ivan Damgaard

locations in our university operating with real time speed of 14 secure bits per second[104]. During this period we found that the 150 meter delay line in the 'long arm' is very sensitive to acoustic noise leading to a reduced visibility V and a corresponding increase in QBER_{opt}. Improved electronic design can reduce this delay to 50 ns (10 m delay) and eliminate this source of error. If we further substitute new peltier cooled detectors and increase the pulse repetition rate we believe our system can operate with a secure bit rate approaching the predicted result in Fig.8.6 (dotted curve).

8.5 Summary and Outlook

In this Chapter we describe the useful application of quantum projection noise to distribute a secret bit-string (key) over an open quantum channel. The basic BB84 protocol is explained using the photon as qubit carrier and implementing the qubit in either phase or polarisation. The ultimate security of the BB84 is derived from the intuitive notion that the information (per bit) released by Alice is bounded, i.e. Eve and Bob can not simultaneously have unit information gain : $I_{AE} + I_{AB} \leq 1$ (see section 8.2.2). This "information exclusion principle" is just a rewriting of Heisenbergs uncertainty relation and thus the security of quantum cryptography (QC) is based on a "proven" physical principle as opposed to todays public key systems which trust unproven computational complexity.

From an experimental point of view the challenge of transmitting single qubits is well matched by todays commercial photonics products such as laser diodes, optical fibers, and avalanche photodiodes (APD). However, while optical fiber manufacturing has already reached the "clarity limit", there is now a rapid development towards improved single photon detection at telecom wavelength and the construction of true single photon sources, i.e. photon guns (see below).

Based on the available technology (1998) we build a plug&play interferometer to transmit qubits coded in the phase of faint laser pulses with (average) $\mu = 0.1$ photon. Testing our setup we find very high visibility $V = 0.995$ due to the automatic length- and polarisation alignment with a Faraday mirror. A major drawback of the present setup is a homebuild InGaAs/InP single photon detector operated in gated-mode (1.1 ns) and cooled to -150°C. It shows an effective single photon detection efficiency $\bar{\eta} = 0.02$ and dark count probability per gate $p_{dark} = 4.5 \times 10^{-5}$. The low operating temperature is necessary to avoid thermal dark counts, but prolongs the lifetime of trapped carriers thus limiting the effective repetition rate to $f_{rep} = 70$ kHz due to afterpulsing. With these parameters our system performs secure key distribution over 20 km at a rate close to 10 bits/sec (see solid curve in Fig.8.6). With new commercial peltier cooled InGaAs/InP APD's the afterpulsing is reduced and realistic repetition rates approach 10 MHz while dark counts are limited to $p_{dark} = 1 \times 10^{-5}$ (1 ns gate) and counting efficiency is close to $\bar{\eta} = 0.05$. Substituting these parameters we predict that our system can perform secure key distribution over 20 km with a rate around 3 kbit/sec (see dotted curve in Fig.8.6). Furthermore it is important to reduce the length of Bob's long arm which presently act as a microphone for acoustic noise and reduces the interferometer visibility . This problem can be completely circumvented if we make all Bob's fiber optic equipment polarisation maintaining.

8.5.1 QC - fundamental physics versus engineering science

Clearly the goal of quantum information is to take weird or paradoxical quantum phenomena and turn them into useful applications which can not be reproduced using only classical physics. This strategy has led to the discovery of novel protocols such as quantum- cryptography, -teleportation, and -computation[89]. This is fundamental physics : it stimulates the search for the ultimate potential/limit of quantum physics. Only now we start asking basic questions which could have been formulated and answered by the pioneering quantum physicists 70 years ago. One simple example is the question of the optimal fidelity of a universal $1 \rightarrow M$ qubit cloner[116]. This simple question has triggered new beautiful discoveries : (i) the qubit copymachine fidelity $\mathcal{F}_{1\rightarrow 2} = 5/6$ is the maximal allowed for Alice and Bob not to be able to build a superluminal communicator based on EPR entanglement[117], (ii) this copymachine is realized for the polarisation qubit of a single photon by stimulated emission in nonlinear crystals[118], and (iii) maybe not surprisingly the 1 → 2 copymachine is the optimal attack in certain QC protocols[119].

While the input to the quantum information field derives from fundamental physics, the output in terms of application devices is defined by the state the art in engineering science. Today the fundamental physics input to the field of QC is more or less saturated while the practical output is undergoing a rapid development. This is evident from a number of focus articles published very recently in New J. Phys. **4** (2002) : (nr.41) the first commercial available plug&play QC system is demonstrated over 67 km of installed fiber network[8], (nr.42) IBM researchers have develop their first plug&play QC system[9], and (nr.43) the Los Alamos National Laboratory (LANL) demonstrate free-space QC over 10 km in daylight. In addition the group of P.Grangier demonstrate for the first time QC with a photon gun using the nitrogen-vacancy color center in a diamond nanocrystal (q-ph/0206136). The photon gun reduces the fraction of two-photon pulses by a factor of 14 as compared to an equivalent Poisson distributed source, but due to problems with coupling the fluorescence photon into a single spatial mode the efficiency is only 1.3% (it is not yet suited for duelling). It is interesting to note that this last experiment uses the QuCrypt software package which is made available at: http://www.cki.au.dk/experiment/qrypto/doc/.

The above results demonstrate that single photon QC has reached its full potential possible with todays technology. To avoid technical limits imposed by single photon generation and detection one can think of using continuous quantum variables, i.e. the optical field quadrature observables which we have discussed at length in the previous chapters. In the following subsection we briefly comment on this direction of QC research/application.

8.5.2 Continuous variable quantum cryptography

The following discussion is based on results derived and published by F. Grosshans and P. Grangier, see Ref.[120],[121],[122]. It is important to realize that the basic objects used to analyze continuous variable quantum cryptography (CVQC) are again the mutual information I_{AB}, I_{AE} and I_{BE}. The tool used to calculate these objects is the Shannon formula for the maximum capacity of a noisy transmission channel (in units of bits/measurement). If the signal and noise statistics are both Gaussian and their ratio is Σ (signal-to-noise ratio or SNR) the maximum channel capacity is

$$I_{AB} = \frac{1}{2}\log_2(1+\Sigma_B) \tag{8.14}$$

This equation has the following interpretation. Alice draws a random amplitude x_A from a Gaussian law with variance VN_0 and prepares a coherent state $|x_A\rangle$ with Gaussian vacuum noise N_0. For a perfect quantum channel Bobs homodyne detector measures the amplitude quadrature x_B with a SNR $\Sigma_B = VN_0/N_0 = V$. As an example suppose $\Sigma_B = 15$ for which the maximal channel capacity is $I_{AB} = 2$ bit per measurement. Then using a classical algorithm (called *sliced reconciliation)* Alice and Bob convert with high probability their correlated amplitudes x_A and x_B into two shared bits[121].

The CVQC scheme can now be described by the following steps : (i) Alice draws two random amplitudes x and p from a Gaussian law with variance VN_0.(ii) She sends to Bob the coherent state $|x+ip\rangle$ with vacuum noise N_0. (iii) Bob measures randomly either the X or P quadrature with a homodyne detector. (iv) Bob informs Alice which quadrature he measured and Alice keeps only her random amplitude for this quadrature. (v) Using "sliced reconciliation" Alice and Bob transform their correlated Gaussian amplitudes into errorless bit strings.

After step (v) Alice and Bob share identical bits which are partially known by Eve and they can use privacy amplification to distill a secret key if $\delta = I_{AB} - I_{AE} > 0$. With an eye to Fig.8.2 we introduce the added noise $N_B = \chi N_0$ on Bob's side which is the continuous equivalent of the discrete QBER. Then according to Fig.8.2 our job is to calculate the threshold value χ_0 where $\delta = 0$. It is

---

[8] see also Nature **418** (2002) p.270

[9] see also Optics & Photonics News **13** (7) /2002 p. 26

straightforward to calculate $I_{AB}(\chi)$. To calculate $I_{AE}(\chi)$ we note that the *minimum* added noise on Eve's side is $N_E = \chi^{-1}N_0$. This result is a Heisenberg inequality $N_B N_E \geq N_0^2$ which in fact is equivalent to the optimal cloning fidelity $\mathcal{F}_{1\rightarrow 2} = 2/3$ for coherent states[120]. Putting things together we have $1 + \Sigma_B = \frac{1+\chi+V}{1+\chi}$ and $1 + \Sigma_E = \frac{1+\chi^{-1}+V}{1+\chi^{-1}}$ and thus the effective key rate scales as (the subscript DR is explained below)

$$\delta_{DR}(\chi) = \frac{1}{2}\log_2\left[\frac{1+\Sigma_B}{1+\Sigma_E}\right] = \frac{1}{2}\log_2\left[\frac{1+\chi+V}{1+\chi+\chi V}\right] \tag{8.15}$$

Privacy amplification is possible as long as $\chi < 1$, i.e. the added noise on Bob's side is less than one vacuum unit. But if the quantum channel has more than 3 dB loss the above CVQC protocol is no longer secure. This result is quite intuitive : the >3dB loss can in principle be due to Eve splitting off more than 50% of the signal beam in which case she can clearly obtain better knowledge of Alice's key than Bob.

The above limit is somewhat disappointing since it limits CVQC to roughly 10 km in optical fibers. But it has recently been realized that this limit can actually be removed completely by reversing the direction of step (v) in the above CVQC protocol[122]. The apparent problem is the sliced reconciliation protocol which runs from Alice to Bob, i.e. Alice tells Bob how he should correct his binary string to match her own. This direction of error correction is called *Direct Reconciliation* (DR) and the relevant security parameter is $\delta_{DR} = I_{AB} - I_{AE}$ which leads to the 3 dB limit. On the other hand the direction of *Reverse Reconciliation* (RR) is from Bob to Alice, i.e. Bob tells Alice how to change her key to match his own. Now the relevant security parameter is $\delta_{RR} = I_{AB} - I_{BE}$ and since Alice can always guess better than Eve what Bob received it turns out that the RR is secure ($\delta_{RR} > 0$) for any channel loss. The equivalent mathematical statement is

$$\delta_{RR} = \frac{1}{2}\log_2\left[\frac{V_{B|E}}{V_{B|A}}\right] \tag{8.16}$$

Here $V_{B|E}$ is the noise (conditional variance) for Eve's guess on Bobs quadrature measurement. Since Alice has less noise (her guess is better) the ratio in Eq.(8.16) is always larger than one. The result in Eq.(8.16) can be written in the form $\delta_{RR} = -\frac{1}{2}\log_2\left[1 - \eta(1 - V^{-1})\right]$ where η is the channel transmission[122] . With a quadrature modulation/measurement rate of 5 MHz, 20 dB channel loss (0.2 dB/km loss in 100 km 1550 nm fiber) and a realistic modulation $V = 10$ the effective key rate is above 30 kbit/sec. This number should be compared with zero for single photon QC since at 100 km dark counts have already increased the QBER beyond the point where $\delta = 0$.

The above numerical example clearly motivates the installation of CVQC. With erbium-doped fiber lasers/amplifiers it is technically possible to establish long distance phase-sensitive communication using germanium or InGaAs/InP detectors (PIN or APD) operated at room temperature. Furthermore the CVQC protocol described above uses only coherent state modulation. The security against any individual attack by Eve derives from the impossibility to clone continuous variables which is the same whether they come with coherent- or nonclassical Gaussian statistics. But encoding using squeezed or EPR-entangled fields does in fact improve security when the quantum channel has excess noise beyond the transmission loss[122]. CVQC is thus a field where a compact squeezing source could find possible application although it is probably more likely that a coherent state modulation scheme will be implemented. Beyond the application considerations it is quite interesting to note that the exact formulation of the limits on cloning continuous quantum variables has only appeared within the last few years[123]. This clearly shows the impact of the increased focus on quantum physics as a new information science.

Chapter 9

Summary

This thesis investigates quantum noise in observables with either continuous or discrete spectra. The continuous observable is a linear combination of (scaled) position and momentum of the harmonic oscillator. We probe an optical oscillator ($\omega_0/2\pi = 3.5 * 10^{14}$ Hz) through homodyne noise detection. By scanning the phase of the local oscillator we perform a 2π-sweep in phasespace. Anisotropy in the Wigner distribution is revealed by an increase/decrease in the fluctuation level of the homodyne current relative to the constant level of the isotropic vacuum, i.e. the standard quantum level (SQL). For the Gaussian noise-statistics reported in this thesis it is sufficient to observe the smallest/largest fluctuations (relative to SQL) to specify completely the Wigner distribution or quantum state of the oscillator.

The workhorse in the continuous variable experiments is a phase-sensitive optical parametric amplifier or OPA. An intuitive (classical) picture of the OPA is presented in Chapter 2, while a more formal derivation of the Gaussian noise output follows in Chapter 3. The most compact formulation of the OPA is through the Bogoluibov transformation $\hat{a}^{(out)} = \mu\hat{a}^{(in)} + \nu\hat{a}^{(in)\dagger}$ where $\hat{a}$ is the (non-hermitian) step-operator of the oscillator. The dependence of μ, ν on scaled pump parameter and spectral frequency determines the full spectrum of squeezing/antisqueezing as $|\mu \mp \nu|^2$ relative to SQL=1. In Chapter 4 we describe in detail the design and construction of our OPA and test it against theory. The individual OPA components and parameters are chosen for spectral tunability and the cavity free spectral length (FSR=Δ=370 MHz) is matched to a standard acousto optical double pass frequency shift. This is important for the experimental demonstration of quadrature entanglement between *frequency* nondegenerate signal and idler optical modes which is the subject of Chapters 5 and 6.

In Chapter 5 we start out by discussing the parametric coupling of two arbitrary oscillators and then specialize to the case of signal/idler (ω_1/ω_2) optical modes realized by the symmetric, resonant pair $\omega_{1,2} = \omega_0 \pm \Delta$ inside our OPA. Again the most compact formulation of the NOPA (nondegenerate OPA) is through the Bogoliubov transformations $\hat{a}_{1,2}^{(out)} = \mu\hat{a}_{1,2}^{(in)} + \nu\hat{a}_{2,1}^{(in)\dagger}$ where we note that a simple 50/50 mixing of signal and idler results in two uncorrelated squeezed modes. The full correlation-spectrum of (two-mode) squeezing/antisqueezing between signal and idler is again $2|\mu \mp \nu|^2$ relative to SQL=2. Although this simple result in principle describes all NOPA experiments (including the one presented in this thesis) we also include a more formal theory deriving the optimal measurement strategy for asymmetric loss between signal and idler mode. In chapter 6 we present the NOPA experimental setup and results. The setup is simply the OPA cavity extended with a filter cavity allowing for spatial mode separation between signal and idler. We characterize our result according to a recent continuous variable entanglement criteria which can be explained as follows. The nature of the NOPA state is an approximate co-eigenstate of the joint observables $x_- = x_1 - x_2$ and $y_+ = y_1 + y_2$ (this type of quantum state was introduced by Einstein, Podolsky and Rosen or EPR). Thus in the NOPA state the variance sum $V = V(x_-) + V(y_+)$ tends to zero. The entanglement criteria is based on the observation that for *any separable* two mode state this sum is bounded from below by two ($V \geq 2$). In the experiment reported in Chapter 6 we observe $V = 0.82(4)$ clearly demonstrating inseparability and in contrast to previous experiments this entanglement was observed between oscillators separated $2\Delta = 740$ MHz in frequency.

Chapter 7 combines a theoretical and experimental investigation of the "back-action" noise transfer between optical- and atomic continuous variables. A dispersive probe is used to read out the atomic noise in the spinpolarized $F = 4$ hyperfine groundstate of atomic cesium contained in a room temperature vapour cell. Adding the tunable squeezed vacuum from the OPA we can modulate the quantum noise on the dispersive probe. This modulation is directly visible on the Lorentzian atomic spin noise signal allowing us to isolate the "back-action" noise". We carefully measure the scaling of this noise against probe power, total spin and Lorentzian linewidth. The observed scaling is well described by simple theory assuming a non-demolition type interaction between optical- and atomic observables.

Chapter 8 describes the construction of a fiber-optic "plug-&-play" quantum cryptography link. This system is complementary to the rest of the thesis : (i) we consider single photons with discrete spin 1/2 spectra, and (ii) we are not seeking to reduce the projection noise in this spin 1/2 (which is anyway impossible for a single spin), but actually exploit it to distribute a secret key. We discuss the state of the art in single photon optics, i.e. single photon sources ("photon guns"), optical fiber- versus free space quantum channel, and single photon detection both with silicon ($\sim$ 0.8 μm) and germanium/InGaAs ($\sim$ 1.3 μm/1.5 μm). With this background we discuss possible improvements to our "plug-&-play" setup which could possible speed up the current rate ($\sim$ 14 secure bits/sec over 20 km 1.3 μm fiber) by three orders of magnitude.

9.1 Outlook

The engineered quantum states discussed in this thesis and elsewhere can, at least on paper, be applied (i) in continuous variable quantum information protocols, (ii) to improve the signal to noise ratio in spectroscopy and atomic clocks, (iii) to improve optical imaging[124], and (iv) to improve clock synchronization[125].

Let us discuss the first application (i). The deterministic preparation of an approximate EPR-state is the basic building block in the continuous variable quantum teleportation protocol[126]. To date all continuous variable teleportation experiments have mixed two squeezed beams to realize this state[52],[54],[55]. These experiments observe a reduction in the quality of the EPR correlations as compared to the theoretical expectation[1] In contrast, we observe 3.8 dB two-mode squeezing in the frequency nondegenerate NOPA-state (Chapter 6) which is roughly identical to the observed degree of squeezing from the OPA (Chapter 4) as one should expect. With realistic improvements in OPA parameters we can expect to observe 6 dB of squeezing and hence, according to the argument above, 6 dB of two-mode squeezing between the signal and idler. Such high quality EPR-correlation is essential for teleporting nonclassical properties of the electromagnetic field[127]. Furthermore we have, at least in principle, access to a whole range of signal-idler pairs at frequencies $\omega_{1,2} = \omega_0 \pm m\Delta$ ($m > 1$) under the phasematching curve of $KNbO_3$. Also the NOPA source is easy tunable opening the door towards transfer of Gaussian noise statistics between light to atoms. The experiment presented in Chapter 7 clearly demonstrates that spin polarized cesium atoms are sensitive to the quantum state of an optical probe. However, actual quantum state transfer from an optical mode to an "atomic mode" can only be achieved by teleportation[63]. It is not likely that the first generation of quantum networks are going to be implement this technology simply due to poor fidelity in reconstructing the teleported quantum state. It seems more realistic that (small scale) prototype quantum devices will emerge in strongly coupled systems where deterministic coherent evolution beats dissipation. But one should not yet focus to strongly on the issue of "fittest" quantum technology since many new results (and

---

[1] According to the simple Bogoliubov transformation 6 dB of vacuum squeezing should ideally transform to 6 dB of EPR correlation.

some rewritings of old ones) are surely going to emerge when viewing a specific physical system from the point of quantum information. A simple example is the discussion of the meaning of 1/2 and 2/3 in quantum teleportation highlighting the issue of classical cloning versus quantum cloning.

As discussed in Chapter 8 quantum information science has already produced commercial spin-off's such as quantum cryptography links, quantum random number generators and single photon detectors at telecom wavelengths. The rapid development of these products is related to the fact that they rely on the presence, rather than absence, of quantum noise. Hence it is almost certain that the near future will see quantum cryptography realized with continuos variables. These systems will be protected against eavesdropping by the presence of Gaussian quantum noise (see Chapter 8).

With respect to the second application (ii) the atomic quantum projection noise scaling $N^{-1/2}$ has been observed in a cesium frequency standard[128]. Here N is the number of spin 1/2 objects entering the interferometer which stabilizes the microwave clock. In a recent experiment the group of D.J. Wineland looked at $N = 2$ spin 1/2 objects (^{9}Be$^+$-ions) probed with Ramsey spectroscopy[129]. By entangling the two ions (squeezing the transverse spin) they where able to improve the precision of frequency measurement by a factor of 1.14(1) relative the ideal SQL (perfect state preparation and detection). The limit in improved precision is set by the scaling N^{-1} known as the Heisenberg limit[130]. Thus the cesium fountain operated with $N = 10^6$ allows for a maximal improvement in frequency precision by 3 orders of magnitude. This should however be compared to already existing optical clocks which now surpass microwave clocks and promise improvements beyond 3 orders of magnitude using only a single ion[131]. Thus when trying to implement squeezing in practical systems operating at the quantum limit one should always remember that major improvements in technology can make these efforts obsolete.

Appendix A

OPA parameters

A.1 Threshold for parametric oscillation

In Chapter 3 we calculate the quantum fluctuations from a degenerate optical parametric amplifier. At threshold, when amplification balances cavity losses, sustained oscillations are possible. This is also the point where fluctuations in the linearized model diverge and optimal squeezing is predicted. To design the squeezing experiment and later analyze the data we need to express this threshold in terms of laboratory observables such as the Q-value of the OPA cavity and the crystal nonlinearity E_{NL}.

From the parametric interaction $\hat{V} = i\hbar g(\hat{b}^\dagger \hat{a}^2 - \hat{b}\hat{a}^{\dagger 2})/2$ in Eq.(3.6) we obtain the equation of motion for the averages of the cavity mode excitations $\alpha = \langle \hat{a} \rangle$ and $\beta = \langle \hat{b} \rangle$

$$\begin{aligned} \dot{\alpha} &= -(\gamma_1 + \gamma_2)\alpha - g\alpha^\star \beta + \sqrt{2\gamma_1}\alpha_1^{in} + \sqrt{2\gamma_2}\alpha_2^{in} && \text{(A.1)} \\ \dot{\beta} &= -\gamma_3 \beta + (g/2)\alpha^2 + \sqrt{2\gamma_3}\beta^{in} && \text{(A.2)} \end{aligned}$$

The cavity amplitude decay rates $\gamma_{1,2}$ couple the oscillator mode α to the external fields $\alpha_{1,2}^{in}$ through mirrors M1 and M2 as shown in Fig.A.1. The pump mode β is excited from the external field β^{in} through the mirror M3 with decay rate γ_3. For the following threshold calculation we set $\alpha_{1,2}^{in} = 0$. Integration of Eq.(A.1) and its complex conjugate around the (resonant) OPA cavity with optical length l gives

$$\begin{bmatrix} \alpha(l) - \alpha(0) \\ \alpha^*(l) - \alpha^*(0) \end{bmatrix} = - \begin{bmatrix} \bar{\gamma} & \bar{g}\beta \\ \bar{g}\beta^* & \bar{\gamma} \end{bmatrix} \begin{bmatrix} \alpha(0) \\ \alpha^*(0) \end{bmatrix} \tag{A.3}$$

The scaled decay rate is $\bar{\gamma} = \gamma/\Delta$ with total cavity decay rate $\gamma = \gamma_1 + \gamma_2$ and $\Delta = c/l$ is the cavity free spectral range. The scaled coupling is $\bar{g} = g(l_c/c)$ where l_c is the crystal length and we have used the fact that the oscillator mode only couples to the pump mode inside the crystal. Further we assume a high oscillator quality factor ($Q = \pi/\bar{\gamma} >> 1$) such that we can include losses to lowest order. At threshold and above the decay and amplification balance such that the left hand side of Eq.(A.3) is zero. For a nontrivial solution, that is sustained parametric oscillation, the determinant in Eq.(A.3) must vanish. This gives the threshold condition for the pump mode excitation $|\beta_{th}| = \bar{\gamma}/\bar{g}$ which is the quantity we seek to relate to experimental observables. The scaled decay rate $\bar{\gamma}$ can be simply related to the cavity parameters through

$$2\gamma = \frac{c}{l}(T_1 + T_2) = \Delta(T_1 + L_c + L_b) \tag{A.4}$$

Here we *interpret* the transmission through M2 as the sum of linear cavity losses L_c and blue pump light induced losses L_b and take T_1 to be the transmission through the OPA input coupler. All these parameters can easily be measured as described below and in Chapter 4. The scaled coupling constant

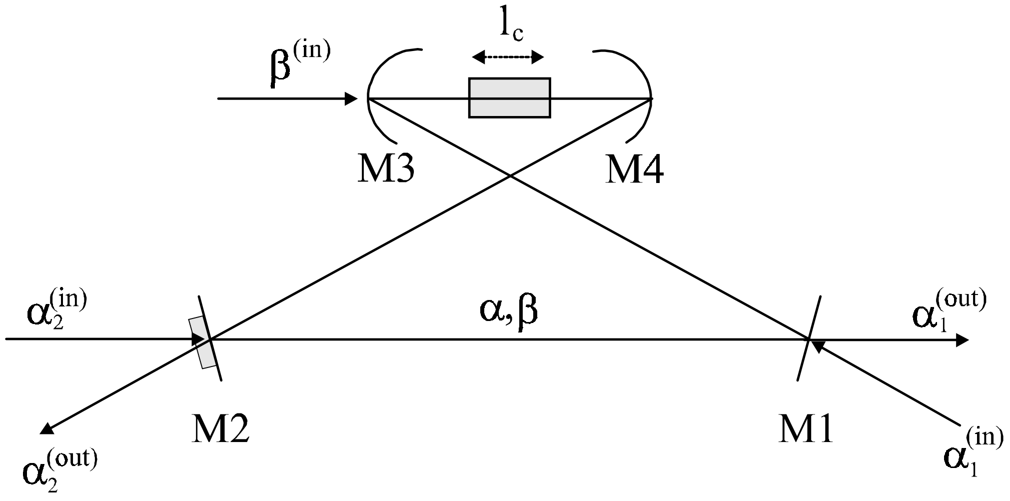

Figure A.1: OPA cavity geometry. The probe fields $\alpha_{1,2}^{(in)}$ are used to measure cavity losses and parametric gain.

$\bar{g}$ can also be linked to the laboratory through the single pass nonlinearity $E_{NL} = P_\beta / P_\alpha^2$ of the OPA crystal. To make this connection we set $\gamma_2 = 0$ in Eq.(A.2) (single pass SHG) and integrate over the crystal length to obtain $\beta(l_c) = (\bar{g}/2)\alpha^2$ with the boundary condition $\beta(0) = 0$. In addition we need an expression relating the circulating cavity power and the mode excitation

$$P_\alpha = (\text{photon density})*(\text{velocity})*(\text{Energy}) = (\frac{|\alpha|^2}{l})(c)(\hbar\omega_\alpha) = |\alpha|^2 \Delta\hbar\omega_\alpha \tag{A.5}$$

with a similar expression for P_β. Using Eq.(A.5) together with the above single pass integration we find

$$E_{NL} = \frac{P_\beta}{P_\alpha^2} = \frac{\bar{g}^2}{\Delta\hbar\omega_\beta} \tag{A.6}$$

where energy conservation in the form $2\omega_\alpha = \omega_\beta$ has been applied. Combining Eq.(A.4), Eq.(A.5) and Eq.(A.6) with the threshold excitation $|\beta_{th}| = \bar{\gamma}/\bar{g}$ gives the final result

$$P_\beta^{th} = \frac{\bar{\gamma}^2}{E_{NL}} = \frac{\pi^2}{Q^2 E_{NL}} = \frac{(T_1 + L_c + L_b)^2}{4E_{NL}} \tag{A.7}$$

This equation tells us how to reduce the threshold for parametric oscillation by optimizing the nonlinearity (see A.4) and/or using a high quality cavity. Improving the cavity quality is limited to changing the coupler transmission T_1 since linear cavity losses L_c are already bound by the coating- and optical quality of the crystal and mirrors. The choice of coupler transmission has to carefully take into account the dependence of L_b on pump intensity since this loss together with L_c will reduce the escape efficiency as described in Chapter 4. Eq.(A.7) is very useful for designing the squeezing experiment, i.e. picking the right coupler, but for measuring the pump parameter $\epsilon = (P_\beta / P_\beta^{th})^{1/2}$ we would need to perform several independent measurements with respective errors. In the next section we develop a single gain measurement which gives us directly the pump level.

A.2 Parametric gain

Let us return to the average mode excitation α as described by Eq.(A.1). We keep α_1^{in} zero but assume that the mode is excited by the probe field α_2^{in} coupled through the mirror M2 in Fig.A.1. In steady state the cavity round-trip integration of Eq.(A.1) is zero and we find the coupled set of equations

$$\gamma \begin{bmatrix} 1 & \epsilon \\ \epsilon & 1 \end{bmatrix} \begin{bmatrix} \alpha \\ \alpha^* \end{bmatrix} = \sqrt{2\gamma_2} \begin{bmatrix} \alpha_2^{in} \\ \alpha_2^{in*} \end{bmatrix} \tag{A.8}$$

The definition of the pump parameter $\epsilon = (P_\beta / P_\beta^{th})^{1/2} = (\beta/\beta_{th})^{1/2}$ has been used together with the threshold excitation $\beta_{th} = \bar{\gamma}/\bar{g}$. We are going to observe the cavity transmission of the excitation coupled through mirror M1 into the output mode α_1^{out}. For this purpose we introduce the boundary condition on M1 in the form of the input/output relation $(2\gamma_1)^{1/2}\alpha = \alpha_1^{in} + \alpha_1^{out}$[36]. Substitution of this relation (with $\alpha_1^{in} = 0$) into Eq.(A.8) followed by simple inversion gives

$$\begin{bmatrix} \alpha_1^{out} \\ \alpha_1^{out*} \end{bmatrix} = \frac{\sqrt{(2\gamma_1)(2\gamma_2)}}{\gamma(1-\epsilon^2)} \begin{bmatrix} 1 & -\epsilon \\ -\epsilon & 1 \end{bmatrix} \begin{bmatrix} \alpha_2^{in} \\ \alpha_2^{in*} \end{bmatrix} \tag{A.9}$$

Now inserting into Eq.(A.9) an input field $\alpha_2^{in} = \left|\alpha_2^{in}\right| e^{i\varphi}$ with phase φ relative to the (real) pump field β we obtain

$$\frac{\alpha_1^{out}}{\left|\alpha_2^{in}\right|} = \frac{\sqrt{(2\gamma_1)(2\gamma_2)}}{\gamma} \left[\frac{1}{1+\epsilon}\cos(\varphi) + i\frac{1}{1-\epsilon}\sin(\varphi) \right] \tag{A.10}$$

To generate an observable photodetector signal we square Eq.(A.10) and insert the mirror transmissions from Eq.(A.4)

$$V(\epsilon,\varphi) = \frac{P_1}{P_2} = \frac{4T_1T_2}{(T_1 + L_c + L_b)^2} \left[\frac{1}{|1+\epsilon|^2}\cos^2(\varphi) + \frac{1}{|1-\epsilon|^2}\sin^2(\varphi) \right] \tag{A.11}$$

When the pump mode is zero ($\epsilon = 0$) the right hand side of Eq.(A.11) is just the OPA cavity transmission coefficient between mirrors M1 and M2. As soon as we add the pump ($0 < \epsilon < 1$) we clearly see the phase-sensitive gain characteristic of the parametric amplification process. The divergence when we reach threshold is inherent in the linearized approach used here. Measuring $V(\epsilon, \varphi)$ while scanning the phase φ and comparing this signal to the phase-insensitive reference level $V(\epsilon = 0)$ we can extract the pump level ϵ from a single oscilloscope trace. This approach is used in the experimental work to establish the pump level for later comparison between theory and experiment.

A.3 Measuring L_c and L_b

The starting point is again Eq.(A.1) now with $\alpha_2^{in} = g = 0$ and excitation coming from α_1^{in}. The Fourier transform of this equation gives the steady state cavity excitation

$$\alpha(\omega) = \frac{(2\gamma_1)^{1/2}}{(\gamma_1+\gamma_2) + i\delta}\alpha_1^{in}(\omega) \tag{A.12}$$

Here $\delta = \omega - \omega_c$ is the detuning of the probe field $\alpha_1^{in}(\omega)$ from the cavity resonance ω_c. In experiments the probe frequency is fixed and we scan the cavity resonance by displacing the piezo mounted mirror M2. Combining Eq.(A.12) with the (transformed) boundary condition $(2\gamma_1)^{1/2}\alpha(\omega) = \alpha_1^{in}(\omega) + \alpha_1^{out}(\omega)$ on mirror M1 we obtain the input/output relation

$$\frac{\alpha_1^{out}(\omega)}{\alpha_1^{in}(\omega)} = \frac{(\gamma_2-\gamma_1) - i\delta}{(\gamma_2+\gamma_1) + i\delta} \tag{A.13}$$

We now define the experimental parameter $r(\delta) = \left|\alpha_1^{out}/\alpha_1^{in}\right| = (P_1^{out}/P_1^{in})^{1/2}$ with the value $r(0) = (\gamma_2 - \gamma_1)/(\gamma_2 + \gamma_1)$ on resonance and $r(\infty) = 1$ off resonance ($\delta >> \gamma_1 + \gamma_2$). Then from the measurement of the ratio $r = r(0)/r(\infty)$ we can derive the residual cavity losses

$$L_c + L_b = T_1\frac{1-r}{1+r} \tag{A.14}$$

where we have inserted the mirror transmissions from Eq.(A.4). With zero pump mode ($\beta = 0$) the blue light induced losses vanish ($L_b = 0$) and from the reflection measurement on the OPA coupler we derive the passive linear cavity loss L_c. Knowing L_c we repeat the reflection measurement now with the blue pump present and thus derive L_b. To avoid any interference from the phase-sensitive gain we detune the crystal temperature away from phasematching ($\epsilon = g = 0$). An alternative way to measure the blue light induced loss comes from the gain measurement described in the previous section, Eq.(A.11). When $\epsilon = 0$ we see that the ratio between the probe power P_2 injected trough M2 and the power P_1 transmitted through the coupler M1 is given by

$$V(L_b) = \frac{P_1}{P_2} = \frac{4T_2T_1}{(T_1 + L_c + L_b)^2} \tag{A.15}$$

Defining the ratio $r = V(0)/V(L_b)$ we can rewrite Eq.(A.15) in the form

$$L_b = (T_1 + L_c)(r^{1/2} - 1) \tag{A.16}$$

Again knowing the linear cavity loss L_c we can measure the ratio r and derive the blue light induced loss L_b. From the (symmetric) transmission expression Eq.(A.15) we see that the cavity buildup factor is

$$\frac{P_c}{P_1} = \frac{4T_1}{(T_1 + L_c + L_b)^2} \tag{A.17}$$

Here P_c is the power of the resonant cavity field and the cavity is excited through the mirror M1 with power P_1. Finally we remark that the Fourier method used in this section fails to identify the multiple resonance structure of the OPA. But again since the cavity quality factor Q is relatively high our results agree with those obtained from a correct calculation where losses are treated to lowest order.

A.4 Optimal focusing in SHG

The plane wave approximation predicts that the conversion efficiency in SHG is proportional to the intensity of the fundamental [26]. This suggest to focus the fundamental to a small waist inside the nonlinear crystal. This idea works up to the point where the Rayleigh length, the distance over which the maximal intensity is reduced by a factor two, is comparable to the crystal length. Below we derive the optimal value for this ratio between crystal length and Rayleigh length. To do this calculation we first introduce a Gaussian solution to the wave equation, which describes very well the spatial properties of laser beams in the laboratory.

From the source free Maxwell equations we obtain the scalar wave equation in the form

$$\nabla^2 E(\mathbf{r}, t) - \mu\epsilon \frac{\partial^2}{\partial t^2} E(\mathbf{r}, t) = \mu \frac{\partial^2}{\partial t^2} P_{NL}(\mathbf{r}, t) \tag{A.18}$$

where the nonlinear polarisation of the crystal P_{NL} is separated from the linear response characterized by the bulk refractive index $n = (\mu\epsilon/\mu_0\epsilon_0)^{1/2}$. Let us first consider the homogenous equation with the familiar plane- and spherical wave solutions. We introduce a spherical wave with the following structure

$$E(\rho, t) = \frac{A}{\rho} e^{ik\rho} e^{-i\omega t} \tag{A.19}$$

The wave vector k and oscillation frequency ω satisfy the linear dispersion relation $\omega = kc/n$ and A is the wave amplitude. The radial distance has the generalized definition $\rho = (x^2 + y^2 + q(z)^2)^{1/2}$ which reduces to $\rho = |\mathbf{r}|$ when $q(z) = z$. We now choose a "complex" source point of the spherical wave by taking $q(z) = z - iz_0$ with z_0 the Rayleigh length[132]. The paraxial approximation, which amounts to keeping quadratic terms in the exponent and only linear terms in the denominator, can now be applied to the spherical wave to obtain

$$E(x, y, z, t) = \frac{A}{q(z)} e^{ik\frac{x^2+y^2}{2q(z)}} e^{i(kz - \omega t)} \tag{A.20}$$

where we have dropped the constant phase e^{-ikz_0}. This is the Gaussian TEM$_{00}$ mode. To further elaborate on this solution we expand $1/q(z)$ and relate it to the radius of curvature $R(z)$ and waist $w(z)$

$$\begin{aligned} \frac{1}{q(z)} &= \frac{z}{z^2+z_0^2}+i\frac{z_0}{z^2+z_0^2}=\frac{1}{R(z)}+i\frac{2}{kw(z)^2} && \text{(A.21)} \\ R(z) &= z+z_0^2/z,\ w(z)=w_0(1+(z/z_0)^2)^{1/2},\ w_0=(2z_0/k)^{1/2} && \text{(A.22)} \end{aligned}$$

The TEM$_{00}$ mode is uniquely defined by specifying the minimum waist w_0 and its position. We want to calculate the optimal waist w_0 of the fundamental beam in SHG. The fundamental field E_1 is approximated by the Gaussian TEM$_{00}$ mode with constant amplitude A_1 (zero pump depletion). The second harmonic field E_2 can not be an exact TEM$_{00}$ but the build up of this field from a Gaussian fundamental is likely to be well described by Eq.(A.20) with a spatially dependent amplitude $A_2(z)$[1]. The nonlinear polarisation driving the second harmonic generation is described by the relation $P_{NL}=dE_1^2$ where d is an effective nonlinear coefficient derived from a general third rank tensor d_{ijk}[26]. When trying to solve the wave equation with this source polarisation a nice trick is to start out with the spherical waveform in Eq.(A.19) which leads to the expression

$$\frac{\partial A_2(z)}{\partial z}2ik_2q_2\frac{1}{\rho_2^2}e^{i(k_2\rho_2-\omega_2 t)}=-\mu d A_1^2\omega_1^2\frac{1}{\rho_1^2}e^{i(2k_1\rho_1-2\omega_1 t)} \tag{A.23}$$

where we have used a slow varying envelope approximation. Energy is naturally conserved in the form $2\omega_1=\omega_2$. Further we observe that optimal conversion is obtained when the wavefront curvature of the harmonic field is everywhere identical with that of the fundamental. Since this curvature is dictated by the Rayleigh length alone as shown in Eq.(A.22) we have the condition $q_1=q_2=z-iz_0$ and therefore $\rho_1=\rho_2$. Now we again apply the paraxial approximation and at the same time divide out the transverse (x,y)-terms which is legitimate since $2k_1\approx k_2$. In this way we reduce Eq.(A.23) to the form

$$\frac{\partial A_2(z)}{\partial z}=i\alpha A_1^2\frac{e^{i\Delta kz}}{q_2} \tag{A.24}$$

with the phase mismatch defined as $\Delta k=2k_1-k_2$ and the constant $\alpha=\mu d\omega_1^2/2k_2$. The generated second harmonic field amplitude is found by integrating Eq.(A.24) over the crystal length l_c. For the field in Eq.(A.20) we find that the power at any point z is related to the amplitude by the relation

$$P_j(z)=\frac{c\epsilon}{2n}\int da\,|E_j(x,y,z)|^2=\frac{c\epsilon\pi}{2nk_jz_0}\,|A_j(z)|^2 \tag{A.25}$$

which when combined with the integral of Eq.(A.24) allows us to calculate the total power in the harmonic field

$$P_2=\beta P_1^2\frac{1}{u_c}\left|\int_{-u_c/2}^{u_c/2}du\frac{e^{i\kappa u}}{1+iu}\right|^2 \tag{A.26}$$

Here we have introduced the scaled crystal length $u_c=l_c/z_0$ and phase mismatch $\kappa=\Delta kz_0$. For a fixed crystal length the constant $\beta=nk_1l_c\alpha^2/\pi c\epsilon$ is independent of these scaled parameters. Using numerical analysis we can optimize the experimentally accessible nonlinearity parameter $E_{NL}=P_2/P_1^2$. The optimal scaled parameters are $\bar{\kappa}=0.57$ and $\bar{u}_c=5.68$, in agreement with previous results based on diffraction theory[133]. In Fig.A.2 the nonlinearity is plotted against the ratio u_c for different values of the phase mismatch κ. The diffraction limited nature of the Gaussian wave solution is clearly displayed by the nonzero optimal wave vector matching.

---

[1] Note we use subscript $1,2$ to distinguish the fundamental and second harmonic field (the previous sections used α,β).

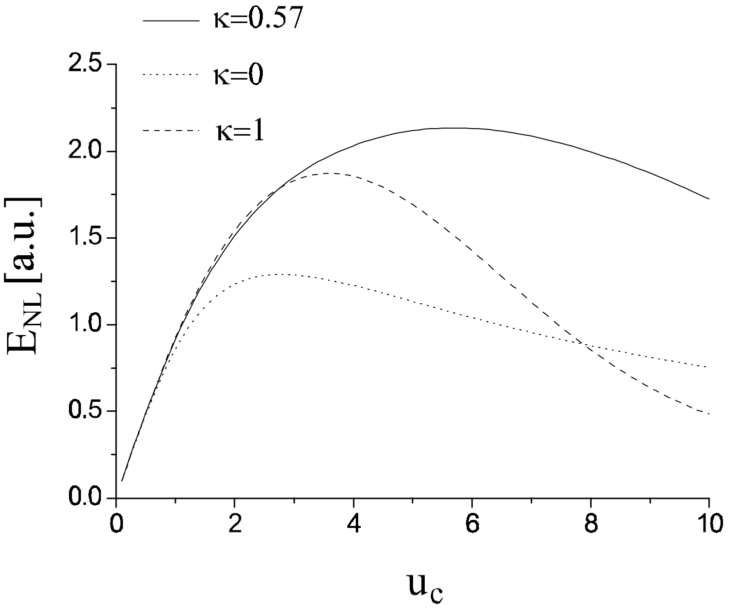

Figure A.2: The single pass nonlinearity E_{NL} plotted against the ratio between crystal- and Rayleigh length $u_c = l_c/z_0$. Shown are curves above and below the optimal (scaled) wavevector matching $\kappa = 0.57$.

A.5 ABCD formalism

As an additional application of Eq.(A.19) we "derive" the ABCD matrix formalism for the Gaussian TEM$_{00}$ mode. The radius of curvature for the spherical wave is $\rho = (x^2 + y^2 + q^2(z))^{1/2}$. When $q(z) = z$ and we confine the discussion to paraxial rays we can use the ABCD formalism to propagate the vector $\mathbf{v} = (r_\perp, \varphi)$ where $r_\perp = (x^2 + y^2)^{1/2}$ is the distance to the optical axis and $\varphi \approx r_\perp/q(z)$ is the ray angle with respect to the axis. Thus the propagation of the paraxial spherical ray from the point z_1 to z_2 through an optical element described by the ABCD matrix takes the form[26]

$$\begin{bmatrix} r_\perp(z_2) \\ \varphi(z_2) \end{bmatrix} = \begin{bmatrix} A & B \\ C & D \end{bmatrix} \begin{bmatrix} r_\perp(z_1) \\ \varphi(z_1) \end{bmatrix} \tag{A.27}$$

Taking the ratio of these two linear equations we find the propagation law for $q(z) = r_\perp(z)/\varphi(z)$

$$q(z_2) = \frac{Aq(z_1) + B}{Cq(z_1) + D} \tag{A.28}$$

Next we simply transform the ordinary spherical wave with $q(z) = z$ into the Gaussian TEM$_{00}$ wave by adding the complex sourcepoint in the form $q(z) = z - iz_0$. We can now propagate the complex q parameter using Eq.(A.28) and the classical ABCD matrix elements. The relevant ABCD matrices $\mathbf{M}$ for cavity construction are

$$\mathbf{M}_l = \begin{bmatrix} 1 & l \\ 0 & 1 \end{bmatrix}, \ \mathbf{M}_n = \begin{bmatrix} 1 & 0 \\ 0 & n \end{bmatrix}, \ \mathbf{M}_R = \begin{bmatrix} 1 & 0 \\ -2/R & 1 \end{bmatrix} \tag{A.29}$$

Here $\mathbf{M}_l$ is free propagation through the distance l, $\mathbf{M}_n$ describes the refraction when the ray enters a material with refractive index n, and $\mathbf{M}_R$ accounts for the reflection from a mirror with curvature R. The results from this section are applied in Chapter 4 to derive the OPA cavity stability curve.

Appendix B

Photodetection and Correlation Spectra

The quantum statistical aspects of photodetection theory are well documented in the literature (see [83] with references). Here we briefly summarize the derivation of the main results as they apply to the detection of squeezed light. We assume perfect detection efficiency without loss of generality (finite efficiency can always be modelled by inserting a beamsplitter in the optical path, see Chapter 3).

B.1 Single balanced homodyne detector

With reference to Fig.B.1a our first task is to establish the relationship between the spectral density of fluctuations in the photocurrent $i(t)$ and the optical field $E(t)$. Defining the correlation $\langle a, b\rangle \equiv \langle ab\rangle - \langle a\rangle \langle b\rangle$ the spectral distribution of photocurrent fluctuations takes the form

$$\Phi_i(\omega) = \mathcal{F}\{r(\tau)\} = \mathcal{F}\{\langle i(0), i(\tau)\rangle\} \tag{B.1}$$

with $\mathcal{F}$ the Fourier transform with respect to τ and $r(\tau) = \langle i(0), i(\tau)\rangle$. The photocurrent is generated as the sum of single photoionization events. To model this situation we divide time into intervals Δt_j and introduce the photoionization probability p_j for each interval. The temporal profile of a single ionization event occurring at time t_j is $Q(t - t_j)$ and the total sum gives the current

$$i(t) = \sum_j p_j Q(t - t_j) \tag{B.2}$$

With this expression the temporal current correlation becomes

$$\langle i(0)i(\tau)\rangle = \sum_j \langle p_j\rangle Q(-t_j)Q(\tau - t_j) + \sum_{j\neq k} \langle p_j p_k\rangle Q(-t_j)Q(\tau - t_k) \tag{B.3}$$

The quantum statistical properties of the light field $\hat{E}(t)$ enter though the moments $\langle p_j p_k ...\rangle$ of the photoelectron generation

$$\langle p_j p_k ...\rangle = \langle : \hat{I}(t_j)\hat{I}(t_k).. :\rangle \Delta t_j \Delta t_k.. \tag{B.4}$$

where $\hat{I}(t) = \hat{E}^\dagger(t)\hat{E}(t)$ is the photon flux in front of the detector with unit quantum efficiency and $\langle ::\rangle$ means time- and normal ordering of operators. Since each photoelectron produces a current pulse which is short compared to the interesting correlation time (∼inverse OPA bandwidth) we can use the approximation $Q(t) = q\delta(t)$. Here q is the total charge from a single detection event including post amplification. Next we let the intervals Δt_j approach zero and replace sums by integrals to obtain the result

$$r(\tau) = q i_0 \delta(\tau) + q^2 R(\tau) \tag{B.5}$$

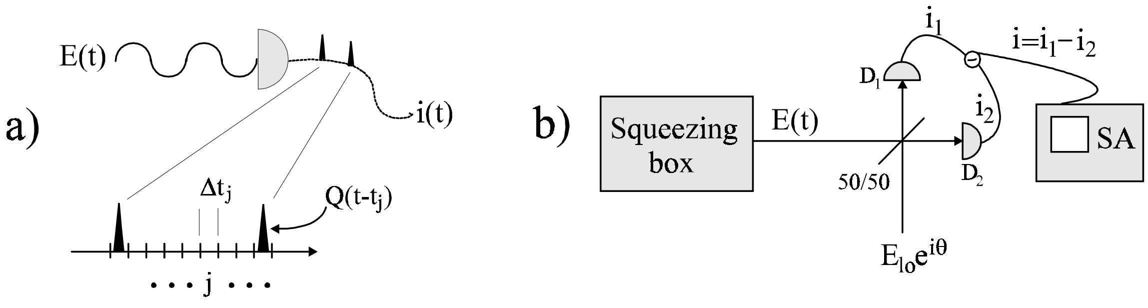

Figure B.1: a) Photocurrent $i(t)$ viewed as sum of ionization events. b) Single homodyne detector. The model in (a) is used to relate the fluctuations in the optical field to the measured fluctuations in the balanced photocurrent.

where $i_0 = q\langle\hat{I}\rangle$ is the average current from a single detector and $R(\tau) = \langle : \hat{I}(0), \hat{I}(\tau) : \rangle$. The first delta correlated term represents the unavoidable shotnoise contribution while the second term can be "engineered" to probe the quadrature fluctuations by way of the balanced homodyne setup shown in Fig.B.1b. In this configuration we must calculate correlations $r_{ij}(\tau) = \langle i_i(0), i_j(\tau)\rangle$ between photoelectrons generated in detectors $D_{i,j}$ $(i, j = 1, 2)$. For $i = j$ we recover the result in Eq.(B.5) while for $i \neq j$ only the last term survives since we no longer have the shotnoise contribution, i.e. product of identical currents at $\tau = 0$. With the definition $R_{ij}(\tau) = \langle: \hat{I}_i(0), \hat{I}_j(\tau) :\rangle$ the formal expression becomes

$$r_{ij}(\tau) = qi_0\delta(\tau)\delta_{ij} + q^2R_{ij}(\tau) \tag{B.6}$$

where we assume equal gain q and photon flux for each detector. This last result invites us to formulate a very simple and perhaps intuitive "correlation protocol". When correlating a linear sum of currents i_j from detectors D_j just replace $i_j(t)$ with the normally ordered "electron flux" operator $q\hat{I}_j(t)$ and remember to add a shotnoise contribution from self-correlation $q^2\langle\hat{I}_j\rangle\delta(\tau) = qi_0\delta(\tau)$. Let us apply this protocol to obtain the spectral density of fluctuations in the balanced current $i = i_1 - i_2$

$$\begin{aligned} \Phi_i(\omega) &= \mathcal{F}\{\langle i_1(0) - i_2(0), i_1(\tau) - i_2(\tau)\rangle\} = 2qi_0 + q^2\mathcal{F}\{R(\tau)\} && \text{(B.7)} \\ R(\tau) &= \langle: \hat{I}_1(0) - \hat{I}_2(0), \hat{I}_1(\tau) - \hat{I}_2(\tau) :\rangle && \text{(B.8)} \end{aligned}$$

The final task is to setup a specific field configuration for the homodyne detector and evaluate $R(\tau)$. As shown in Fig.B.1b the squeezed field $\hat{E}(t)$ beats with a strong *classical* local oscillator field $E_{lo} = E_0e^{i\theta}$ with amplitude E_0 and phase θ. The 50/50 beamsplitter combines these fields into $\hat{E}_{1,2}(t) = 2^{-1/2}(E_{lo} \pm \hat{E}(t))$ which impinge on detectors $D_{1,2}$. The local oscillator noise is common mode in both detectors an the noise of the squeezed field appears in the noise of the balanced current $i = i_1 - i_2$. Substituting the photon flux operators $\hat{I}_j(t) = \hat{E}_j^\dagger(t)\hat{E}_j(t)$ into Eq.(B.8) we obtain the approximate result

$$\hat{I}_1(t) - \hat{I}_2(t) = E_0\hat{Q}_\theta(t) \tag{B.9}$$

Thus the balanced current probes the quadrature observable $\hat{Q}_\theta(t) = \hat{E}(t)e^{-i\theta} + \hat{E}^\dagger(t)e^{i\theta}$ of the squeezed field. Application of this result in Eq.(B.8) yields

$$R(\tau) = E_0^2\langle: \hat{Q}_\theta(0), \hat{Q}_\theta(\tau) :\rangle \tag{B.10}$$

Clearly we have to tag our spectral density in Eq.(B.7) with the phase θ of the local oscillator, i.e. $\Phi_i(\omega, \theta)$. The demodulation from the optical carrier frequency has left us with quadrature fluctuations plus shotnoise. The quadrature fluctuations decay on a timescale set by the OPA cavity bandwidth which is typical several MHz. Thus one is naturally led to examine the spectral density with an electronic spectrum analyzer (SA). Like any spectral instrument this device operates with a finite resolution bandwidth $RBW = \Delta\omega$ and the digitized output is the integral of the (symmetric) spectral density over this bandwidth. From Eq.(B.7) and Eq.(B.10) we have

$$\Phi_i(\omega,\theta)\Delta\omega = 2qi_0\Delta\omega[1+\Phi_Q(\omega,\theta)] \tag{B.11}$$

where $2qi_0\Delta\omega$ is the photocurrent shotnoise in resolution bandwidth and $\Phi_Q(\omega,\theta)$ is spectrum of quadrature fluctuations

$$\Phi_Q(\omega,\theta) = \mathcal{F}\{\langle : \hat{Q}_\theta(0), \hat{Q}_\theta(\tau) :\rangle\} \tag{B.12}$$

The (normalized) version of Eq.(B.11) connecting the fluctuation spectrum of the balanced current $i(t)$ and the quadrature $Q_\theta(t)$ is the main result of this section.

B.2 Pair of balanced homodyne detectors

Consider the detection setup in Fig.B.2. From Eq.(B.11) we know that the balanced current $i_j = i_{ja} - i_{jb}$ carries the fluctuations of the quadrature observable $\hat{Q}^{(j)}_{\varphi_j}(t) = \hat{E}_j(t)e^{-i\varphi_j} + \hat{E}^\dagger_j(t)e^{i\varphi_j}$ defined for each field $\hat{E}_j(t)$ with $j = 1,2$. From this observation we may expect the fluctuations in the current combination $i = i_1 - i_2$ to reflect the fluctuations in the quadrature combination $Q^{(-)}_\theta(t)$ defined by the operator

$$\hat{Q}^{(-)}_\theta(t) = \hat{Q}^{(1)}_{\varphi_1}(t) - \hat{Q}^{(2)}_{\varphi_2}(t) \tag{B.13}$$

Here the notation $\theta = \varphi_1 + \varphi_2$ presumes that observable effects will only depend on the sum of individual quadrature phases (see Chapter 5). We now proceed using the simple correlation protocol introduced earlier. As usual the center of attention is the spectral density of photocurrent fluctuations

$$\begin{aligned}
\Phi_i(\omega,\theta) &= \mathcal{F}\{\langle i(0), i(\tau)\rangle\} = \mathcal{F}\{\langle i_1(0)-i_2(0), i_1(\tau)-i_2(\tau)\rangle\} = 4qi_0 + q^2\mathcal{F}\{R(\tau)\} &\text{(B.14)}\\
R(\tau) &= \langle: \hat{I}_{1a}(0)-\hat{I}_{1b}(0)-(\hat{I}_{2a}(0)-\hat{I}_{2b}(0)), \hat{I}_{1a}(\tau)-\hat{I}_{1b}(\tau)-(\hat{I}_{2a}(\tau)-\hat{I}_{2b}(\tau)) :\rangle &\text{(B.15)}
\end{aligned}$$

The first term in Eq.(B.14) represents the shotnoise contribution from the four detectors $D_{1a,1b,2a,2b}$. Direct application of Eq.(B.9) allows us to rewrite Eq.(B.15) in the simple form

$$R(\tau) = E_0^2\langle: \hat{Q}^{(-)}_\theta(0), \hat{Q}^{(-)}_\theta(\tau) :\rangle \tag{B.16}$$

To complete the calculation we generalize the definition of the quadrature spectrum in Eq.(B.12) to account for correlated fluctuations in quadratures of different optical modes

$$\Phi_Q(\omega,\theta) = \mathcal{F}\{\langle : \hat{Q}^{(-)}_\theta(0), \hat{Q}^{(-)}_\theta(\tau) :\rangle\} \tag{B.17}$$

The integral of the spectral density in Eq.(B.14) over RBW returns the digitized output from the electronic spectrum analyzer

$$\Phi_i(\omega,\theta)\Delta\omega = 2qi_0\Delta\omega[2+\Phi_Q(\omega,\theta)] \tag{B.18}$$

This result is the generalization of Eq.(B.11) for a pair of homodyne detectors. Note that the shotnoise contribution $4qi_0\Delta\omega$ is twice that of a single balanced detector working in the same RBW. Up to this point we have assumed identical gain $q_j = q$ for each of the four detectors $D_{1..4}$. In any experiment we always balance each homodyne pair such that it is safe to assume $q_1 = q_2$ and $q_3 = q_4$. On the other hand it is quite realistic that the quantum fields $\hat{E}_{1,2}$ in Fig.(B.2) experience different losses in the process of generation and propagation to the detectors. In this case the optimal measurement observable is $\hat{Q}^{(-)}_{\theta,\psi}(t) = \cos(\psi)\hat{Q}^{(1)}_{\varphi_1}(t) - \sin(\psi)\hat{Q}^{(2)}_{\varphi_2}(t)$. Optimization of the mixing angle ψ partially compensates asymmetry between signal and idler mode. It is straightforward to incorporate this adjustment into the theory and here we just note that the shotnoise contribution in Eq.(B.18) is reduced : $2 \rightarrow \sin^2(\psi) + \cos^2(\psi) = 1$. Next we turn to the important question of how to evaluate the quadrature spectrum $\Phi_Q(\omega,\theta)$ for a specific quantum system.

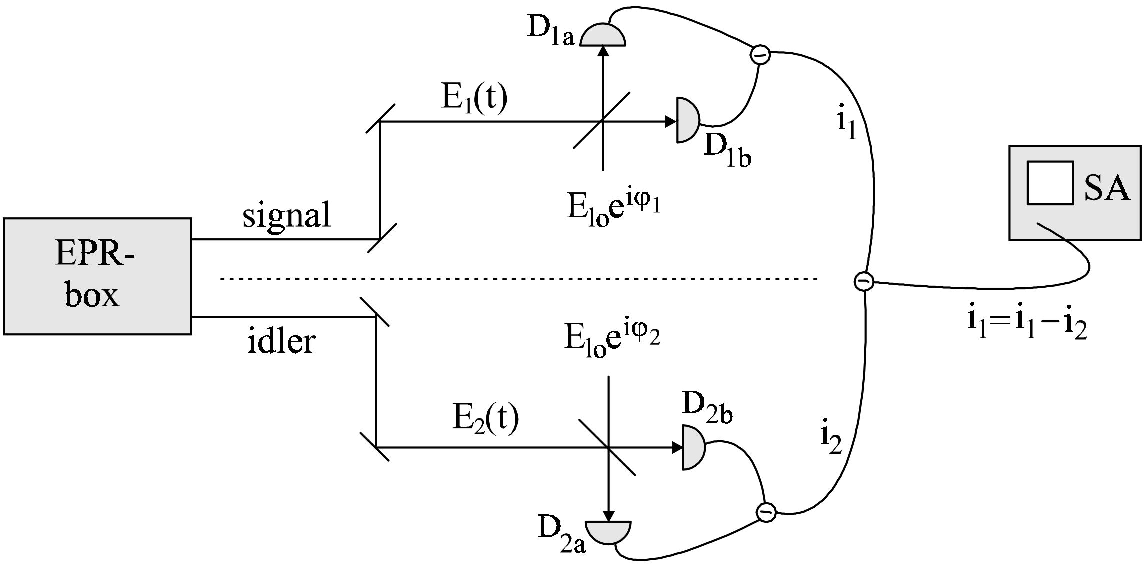

Figure B.2: Pair of homodyne detectors used to investigate the correlated fluctuations in signal and idler field. The text derives the link between optical fluctuations and electronic fluctuations monitored by an electronic spectrum analyzer (SA).

B.3 Quantum dynamics and the quadrature correlation spectrum

The brief review of photodetection results presented in the previous sections showed how experimental data are linked to theory via the quadrature correlation spectrum $\Phi_Q(\omega,\theta)$. In principle further progress would require knowledge of the "squeezing box" Hamiltonian to derive this spectrum. But it is interesting to see how much further one can proceed without specifying the detailed Hamiltonian We shall demand that the system master equation can be rewritten as an equivalent Fokker-Planck equation for a generalized $P(\boldsymbol{\alpha})$-distribution

$$\frac{\partial}{\partial t}P(\boldsymbol{\alpha}) = \sum_{i.,j}\left[\frac{\partial}{\partial\alpha_i}\mathbf{A}_{ij}\alpha_j + \frac{1}{2}\frac{\partial^2}{\partial\alpha_i\partial\alpha_j}\mathbf{D}_{ij}\right]P(\boldsymbol{\alpha}) \tag{B.19}$$

Here the vector $\boldsymbol{\alpha} = (\alpha_1, \alpha_1^\dagger, \alpha_2, \alpha_2^\dagger, ...)$ contain the pairs $(\alpha_j, \alpha_j^\dagger)$ of independent complex variables used to describe the mode j. The drift matrix $\mathbf{A}$ determines the time evolution of meanvalues while the diffusion matrix $\mathbf{D}$ controls the dynamics of second order moments[35]. Basically it takes a nonlinear interaction to produce a squeezed optical field and therefore $\mathbf{A}$ and $\mathbf{D}$ are both functions of $\boldsymbol{\alpha}$. However one usually works with a small ratio of nonlinear coupling rate to linear decay rate which allow a linearization procedure to be applied. Let us assume this has been done so that we can work with constant matrices $\mathbf{A}$ and $\mathbf{D}$ parametrized by the given physical system under study. To proceed further the linear Fokker-Planck equation (B.19) is now replaced by an equivalent set of stochastic Langevin equations[35]

$$\dot{\boldsymbol{\alpha}} = -\mathbf{A}\boldsymbol{\alpha} + \mathbf{B}\boldsymbol{\eta} \tag{B.20}$$

Here $\mathbf{BB^T} = \mathbf{D}$ and the Langevin force vector $\boldsymbol{\eta}$ has zero mean and δ-correlation in time

$$\langle \eta_i(t), \eta_j(t')\rangle = \delta_{ij}\delta(t-t') \tag{B.21}$$

The derivation from the P-distribution means that we can replace quantum averages of normally ordered operator products by the corresponding classical averages of stochastic variables. The normally ordered quadrature spectrum $\Phi_Q(\omega)$ is such an example which is completely determined by the stochastic noisematrix defined by

$$\mathbf{N}(\omega) = \mathcal{F}\left\{\left\langle \boldsymbol{\alpha}(0), \boldsymbol{\alpha}^{\mathbf{T}}(\tau)\right\rangle\right\} \tag{B.22}$$

The linearization of the problem allow us to determine $\mathbf{N}(\boldsymbol{\omega})$ by Fourier transformation. To demonstrate this we introduce the transform pair

$$\boldsymbol{\alpha}(t) = (2\pi)^{-1} \int d\omega \boldsymbol{\alpha}(\omega) e^{-i\omega t}, \;\; \boldsymbol{\alpha}(\omega) = \int dt \boldsymbol{\alpha}(t) e^{i\omega t} \tag{B.23}$$

Then substitution of Eq.(B.23) in the definition of $\mathbf{N}(\omega)$ leads to the alternative expression

$$\mathbf{N}(\boldsymbol{\omega}) = (2\pi)^{-1} \int d\omega' \langle \boldsymbol{\alpha}(\omega'), \alpha^{\mathbf{T}}(\omega)\rangle \tag{B.24}$$

Next we solve the Langevin equation in frequency space by direct transformation of Eq.(B.20)

$$\boldsymbol{\alpha}(\boldsymbol{\omega}) = (\mathbf{A} - \mathbf{I}\omega)^{-1} \mathbf{B} \boldsymbol{\eta}(\boldsymbol{\omega}) \tag{B.25}$$

Here $\mathbf{I}$ is the identity matrix. From Eq.(B.21) we find that the Langevin force in frequency space is also diagonal and δ-correlated

$$\langle \boldsymbol{\eta}(\boldsymbol{\omega}), \boldsymbol{\eta}^{\mathbf{T}}(\boldsymbol{\omega}')\rangle = 2\pi \boldsymbol{\delta}(\boldsymbol{\omega} + \boldsymbol{\omega}')\mathbf{I} \tag{B.26}$$

Combining Eq.(B.25) and Eq.(B.26) and using the relation $\mathbf{B}\mathbf{B}^{\mathbf{T}} = \mathbf{D}$ we find

$$\langle \boldsymbol{\alpha}(\boldsymbol{\omega}), \boldsymbol{\alpha}^{\mathbf{T}}(\boldsymbol{\omega}')\rangle = 2\pi(\mathbf{A} - \mathbf{I}\omega)^{-1} \mathbf{D} (\mathbf{A}^{\mathbf{T}} + \mathbf{I}\omega)^{-1} \delta(\omega + \omega') \tag{B.27}$$

Performing the integration over ω' motivated by Eq.(B.24) leads to the final expression

$$\mathbf{N}(\omega) = (\mathbf{A} - \mathbf{I}\omega)^{-1} \mathbf{D} (\mathbf{A}^{\mathbf{T}} + \mathbf{I}\omega)^{-1} \tag{B.28}$$

This result can be applied to any "squeezing box" which can be approximated by a linear Fokker-Planck equation. The quadrature spectrum $\Phi_Q(\omega)$ is a simple linear combination of elements from the noise matrix $\mathbf{N}(\omega)$ which in turn derives directly from the drift- and diffusion matrix of the system.

Bibliography

[1] E. Schrödinger. *Die Naturwissenschaften*, 28:664, 1926.

[2] W. Heisenberg. *Zeitschrift für Physik*, 43:172, 1927.

[3] E. H. Kennard. *Zetschrift für Physik*, 44:326, 1927.

[4] D. F. Walls. *Nature*, 306:141, 1983.

[5] D. F. Walls. *Nature*, 324:210, 1986.

[6] R. E. Slusher, L. W. Hollberg, B. Yurke, J. C. Mertz, and J. F. Valley. *Phys. Rev. Lett.*, 55:2409, 1985.

[7] L. Wu, H. J. Kimble, J. L. Hall, and H. Wu. *Phys. Rev. Lett.*, 57(20):2520, 1986.

[8] A. Einstein, B. Podolsky, and N. Rosen. *Phys. Rev.*, 47:777, 1935.

[9] M. D. Reid. *Phys. Rev. A*, 40(2):913, 1989.

[10] L.-M. Duan, G. Giedke, J. I. Cirac, and P. Zoller. *Phys. Rev. Lett.*, 84(12):2722, 2000.

[11] E. S. Polzik. *Physics World*, September, 2002.

[12] M. Inguscio, S. Stringari, and C. Wieman, editors. *Bose-Einstein Condensation in Atomic Gases*, Amsterdam, 1999. Int. School Phys. "Enrico Fermi" Course CXL, IOS Press.

[13] S. L. Rolston and W. D. Phillips. *Nature*, 416, 2002.

[14] L. Deng, E. W. Hagley, J. Wen, M. Trippenbach, Y. Band, P. S. Julienne, J. E. Simarian, K. Helmerson, S. L. Rolston, and W. D. Phillips. *Nature*, 218, 1999.

[15] J. M. Vogels, K. Xu, and W. Ketterle. *Phys. Rev. Lett.*, 89(2), 2002.

[16] C. Orzel, A. K. Tuchman, M. L. Fenselau, M. Yasuda, and M. A. Kasevich. *Science*, 291, 2001.

[17] M. Greiner, O. Mandel, T. Esslinger, T. W. Hänsch, and I. Bloch. *Nature*, 415:39, 2002.

[18] P. Bouyer and M. Kasevich. *Phys. Rev. A*, 56:R1083, 1997.

[19] D. Jaksch, H.-J. Briegel, J. I. Cirac, C. W. Gardiner, and P. Zoller. *Phys. Rev. Lett.*, 82:1975, 1999.

[20] J. J. Sakurai. *Modern Quantum Mechanics.* Addison-Wesley Publishing Company, 1994.

[21] E. P. Wigner. *Phys. Rev.*, 40:749, 1932.

[22] A. Royer. *Phys. Rev. A*, 15(2):449, 1977.

[23] M. Morinaga, I. Bouchoule, J. C. Karam, and C. Salomon. *Phys. Rev. Lett.*, 83(20):4037, 1999.

[24] D. J. Heinzen and D. J. Wineland. *Phys. Rev. A*, 42(5):2977, 1990.

[25] D. M. Meekhof, C. Monroe, B. E. King, W. M. Itano, and D. J. Wineland. *Phys. Rev. Lett.*, 76(11):1796, 1996.

[26] A. Yariv. *Optical Electronics in Modern Communications.* Oxford University Press, 1997.

[27] A. I. Lvovsky, H. Hansen, T. Aichele, O. Benson, J. Mlynek, and S. Schiller. *Phys. Rev. Lett.*, 87(5):050402, 2001.

[28] G. Nogues, A. Rauschenbeutel, S. Osnaghi, P. Bertet P, M. Brune, J. M. Raimond, S. Haroche, L. G. Lutterbach, and Davidovich. *Phys. Rev. A*, 62:054101, 2000.

[29] D. Leibfried, D. M. Meekhof, B. E. King, C. Monroe, W. M. Itano, and D. J. Wineland. *Phys. Rev. Lett.*, 77(21):4281, 1996.

[30] E. Schrödinger. *Naturwissenschaften*, 23:807, 823, 844, 1935.

[31] M. Brune, E. Hagley, J. Dreyer, X. Maître, A. Maali, C. Wunderlich, J. M. Raimond, and S. Haroche. *Phys. Rev. Lett.*, 77(24):4887, 1996.

[32] C. Monroe, D. M. Meekhof, B. E. King, and D. J. Wineland. *Science*, 272:1131, 1996.

[33] Z. Y. Ou, S. F. Pereira, and H. J. Kimble. *Appl. Phys. B*, 55:265, 1992.

[34] P. D. Drummond and M. D. Reid. *Phys. Rev. A*, 41:3930, 1990.

[35] D. F. Walls and G. J. Milburn. *Quantum Optics.* Springer, 1994.

[36] M. J. Collett and C. W. Gardiner. *Phys. Rev. A*, 30(3):1386, 1984.

[37] H.-A. Bachor. *A Guide to Experiments in Quantum Optics.* Wiley-VCH, 1998.

[38] P. D. Drummond and S. Chaturvedi. volume 561 of *Lecture Notes in Physics*, chapter 4, page 283. Springer, 2001.

[39] H. J. Kimble and D. F. Walls. Squeezed states of the electromagnetic field. *J. Opt. Soc. Am. B*, 4(10), 1987.

[40] E. S. Polzik, J. Carri, and H.J. Kimble. *Appl. Phys. B*, 55:279, 1992.

[41] K. Schneider, M. Lang, J. Mlynek, and S. Schiller. *Optics Express*, 2(3):59, 1998.

[42] U. Strössner, J. P. Meyn, R. Wallenstein, P. Urenski, A. Arie, G. Rosenman, J. Mlynek, and S. Schiller. *J. Opt. Soc. Am. B*, 19(6):1419, 2002.

[43] J. Hald, J. L. Sørensen, C. Schori, and E. S. Polzik. *Phys. Rev. Lett.*, 83(7):1319, 1999.

[44] B. Julsgaard, A. Kozhekin, and E. S. Polzik. *Nature*, 413:400, 2001.

[45] C. Schori, B. Julsgaard, J. L. Sørensen, and E. S. Polzik. *Phys. Rev. Lett.*, 89(5):057903, 2002.

[46] L. Shiv. Blue-light-induced infrared absorption in KNbO3. Master's thesis, Institute of Physics and Astronomy, Aarhus University, 1995.

[47] H. Mabuchi, E. S. Polzik, and H. J. Kimble. *J. Opt. Soc. Am. B*, 11(10):2023, 1994.

[48] E. S. Polzik and H. J. Kimble. *Opt. Lett.*, 16(18):1400, 1991.

[49] Z. Y. Ou, S. F. Pereira, E. S. Polzik, and H. J. Kimble. *Opt. Lett.*, 17(9):640, 1992.

[50] R. W. P. Drever, J. L Hall, F. V. Kowalski, J. Hough, G. M. Ford, A. J. Munley, and H. Ward. *Appl. Phys. B*, 31:97, 1983.

[51] Z. Y. Ou, S. F. Pereira, H. J. Kimble, and K. C. Peng. *Phys. Rev. Lett.*, 68(25):3663, 1992.

[52] A Furusawa, J. L. Sørensen, S. L. Braunstein, C. A. Fuchs, H. J. Kimble, and E. S. Polzik. *Science*, 282:706, 1998.

[53] C. Silberhorn, P. K. Lam, O. Weiss, F. Konig, N. Korolkova, and G. Leuchs. *Phys. Rev. Lett.*, 86(19):4267, 2001.

[54] W.P. Bowen, N. Treps, B. C. Buchler, R. Schnabel, T. C. Ralph, H.-A. Bachor, T. Symul, and P. K. Lam. *quant-ph/0207179*, 2002.

[55] T. C. Zhang, K. W. Goh, C. W. Chou, P. Lodahl, and H. J. Kimble. *quant-ph/0207076*, 2002.

[56] C. Schori, J. L. Sørensen, and E. S. Polzik. *quant-ph/0205015*, 2002.

[57] J. Mertz, T. Debuisschert, A. Heidmann, C. Fabre, and E. Giacobino. *Opt. Lett.*, 16(16):1234, 1991.

[58] P. H. Souto Ribeiro, C. Schwob, A. Maitre, and C. Fabre. *Opt. Lett.*, 22(24):1893, 1997.

[59] A.. Porzio, C. Altucci, M. Autiero, A. Chiummo, C. De Lisio, and S. Solimeno. *App. Phys. B*, 73:763, 2001.

[60] R. Simon. *Phys. Rev. Lett.*, 84:2726, 2000.

[61] M. Lewenstein, D. Bruss, J. I. Cirac, B. Kraus, M. Kus, J. Samsonowicz, A. Sanpera, and R. Tarrach. *quant-ph/0006064*, 2000.

[62] A. S. Parkins and H. J. Kimble. *J. Opt. B: Quantum Semiclass. Opt.*, 1:496, 1999.

[63] A. Kuzmich and E. S. Polzik. *Phys. Rev. Lett.*, 85(26):5639, 2000.

[64] J. S. Bell. *Speakable and Unspeakable in Quantum Mechanics.* Cambridge University Press, England, 1987.

[65] K. Banaszek and K. Wodkiewicz. *Phys. Rev. A*, 58(6):4345, 1998.

[66] Z-B. Chen, J.-W. Pan, G. Hou, and Y.-D. Zhang. *Phys. Rev. Lett.*, 88(4):040406, 2002.

[67] A. Aspect, J. Dalibard, and G. Roger. *Phys. Rev. Lett.*, 49:1804, 1982.

[68] S. A. Gardiner, J. I. Cirac, and P. Zoller. *Phys. Rev. A*, 55:1683, 1997.

[69] A. Kuzmich, I. A. Walmsley, and L. Mandel. *Phys. Rev. Lett.*, 85(7):1349, 2000.

[70] Vladimir B. Braginsky and Farid Ya. Khalili. *Quantum Measurement.* Cambridge University Press, 1992.

[71] A. La Porta, R. E. Slusher, and B. Yurke. *Phys. Rev. Lett.*, 62:28, 1989.

[72] S. F. Pereira, Z. Y. Ou, and H.J. Kimble. *Phys. Rev. Lett.*, 72(2):214, 1994.

[73] M. Brune, S. Haroche, V. Lefevre, J. M. Raimond, and N. Zagury. *Phys. Rev. Lett.*, 65:976, 1990.

[74] G. Nogues, A. Rauschenbeutel, S. Osnaghi, M. Brune, J. M. Raimond, and S. Haroche. *Nature*, 400:239, 1999.

[75] A. Kuzmich, N. P. Bigelow, and L. Mandel. *Europhys. Lett.*, 42(5):481, 1998.

[76] A. Kuzmich, L. Mandel, and N.P. Bigelow. *Phys. Rev. Lett.*, 85(8):1594, 2000.

[77] E. S. Polzik, J. Carri, and H. J. Kimble. *Phys. Rev. Lett.*, 68(20):3020, 1992.

[78] J. L. Sørensen, J. Hald, N. Jørgensen, J. Erland, and E. S. Polzik. *Quantum Semiclass. Opt.*, 9:239, 1997.

[79] J. L. Sørensen, J. Hald, and E. S. Polzik. *Phys. Rev. Lett.*, 80(16):3487, 1998.

[80] A. Kuzmich, K. Mølmer, and E. S. Polzik. *Phys. Rev. Lett.*, 79:4782, 1997.

[81] A. Kuzmich and E. S. Polzik. *Quantum Information Processing with Continuous Variables*, chapter 1, pages 1–37. to be published by Kluwer, 2002.

[82] B. Yurke, S. L. McCall, and J. R. Klauder. *Phys. Rev. A*, 33(6):4033, 1986.

[83] H. J. Kimble. Quantum fluctuations in quantum optics - squeezing and related phenomena. In J .Dalibard, J. M. Raimond, and J. Zinn-Justin, editors, *Les Houches LIII*. Elsevier, 1990.

[84] B. Julsgaard. Experimental entanglement of two macroscopic atomic ensembles. Master's thesis, Institute of Physics and Astronomy, University of Aarhus, 2001.

[85] X. Maitre, E. Hagley, G. Nogues, C. Wunderlich, P. Goy, M. Brune, J. M. Raimond, and S. Haroche. *Phys. Rev. Lett.*, 79(4):769, 1997.

[86] D. Kielpinski, C. Monroe, and D. J. Wineland. *Nature*, 417:709, 2002.

[87] C. Liu, Z. Dutton, C. H. Behroozi, and L. V. Hau. *Nature*, 409:490, 2001.

[88] J. H. Shapiro. *New J. of Phys.*, 4:47.1–47.18, 2002.

[89] M. A. Nielsen and Isaac L. Chuang. *Quantum Computation and Quantum Information.* Cambridge University Press, 2000.

[90] C. H. Bennett and G. Brassard. In *Proceedings of the IEEE International Conference on Computers, Systems and Signal Processing*, page 175, Bangalore (India), 1984. IEEE (New York).

[91] N. Gisin, G. Ribordy, W. Tittel, and H. Zbinden. *Rev. Mod. Phys.*, 74(1):145, 2002.

[92] C. H. Bennett. *Phys. Rev. Lett.*, 68:3121, 1992.

[93] D. Bruss. *Phys. Rev. Lett.*, 81:3018, 1998.

[94] H. Bechmann-Pasquinucci and A. Peres. *Phys. Rev. Lett.*, 85:3313, 2000.

[95] M. Bourennane, A. Karlsson, and G. Bjorn. *Phys. Rev. A*, 64:012306, 2001.

[96] M. J. W. Hall. *Phys. Rev. Lett.*, 74:3307, 1995.

[97] A. Peres. *Quantum Theory: Concepts and Methods.* Kluwer Academic, 1997.

[98] I. Csizar and J. Korner. *IEEE Trans. Inf. Theory*, IT-24:339, 1978.

[99] C. A. Fuchs, N. Gisin, R. B. Griffiths, C.-S. Niu, and A. Peres. *Phys. Rev. A*, 56:1163, 1997.

[100] R. Brouri, A. Beveratios, J.-P. Poizat, and P. Grangier. *Opt. Lett.*, 25:1294, 2000.

[101] C. Kurtsiefer, S. Mayer, P. Zarda, and H. Weinfurter. *Phys. Rev. Lett.*, 85:290, 2000.

[102] H.P. Yuen. *Quantum Semiclassic. Opt.*, 8:939, 1997.

[103] G. Brassard, N. Lutkenhaus, T. Mor, and B. C. Sanders. *Phys. Rev. Lett.*, 85:1330, 2000.

[104] P. M. Nielsen, C. Schori, J. L. Sørensen, L. Salvail, I. Damgård, and E. S. Polzik. *J. Mod. Opt.*, 48(13):1921, 2001.

[105] G. A. Thomas, B. I. Shraiman, P. F. Glodis, and M. J. Stephen. *Nature*, 404:262, 2000.

[106] S. Cova, M. Ghioni, A. Lacaita, C. Samori, and F. Zappa. *Appl. Opt.*, 35:1956, 1996.

[107] W. T. Buttler, R. J. Hughes, S. K. Lamoreaux, G. L. Morgan, J. E. Norholt, and C. G. Peterson. *Phys. Rev. Lett.*, 84:5652, 2000.

[108] P. M. Gorman, P. R. Tapster, and J. G. Rarity. *J. Mod. Opt.*, 48:1887, 2001.

[109] G. Ribordy, J. D. Gautier, H. Zbinden, and N. Gisin. *Appl. Opt.*, 37:2272, 1998.

[110] A. Muller, H. Zbinden, and N. Gisin. *Nature*, 378:449, 1995.

[111] J. D. Franson and B. C. Jacobs. *Electron. Lett.*, 31:232, 1995.

[112] H. Zbinden, J.-D. Gautier, N. Gisin, B. Huttner, A. Muller, and W. Tittel. *Electron. Lett.*, 586:33, 1997.

[113] R. Hughes, G. Morgan, and C. Peterson. *J. Mod. Opt.*, 47:533, 2000.

[114] A. Tomita and R. Y. Chiao. *Phys. Rev. Lett.*, 57:937, 1986.

[115] G. Ribordy, J.-D. Gautier, N. Gisin, O. Guinnard, and H. Zbinden. *Electron. Lett.*, 34(22):2116, 1998.

[116] V. Buzek and M. Hillery. *Phys. Rev. A*, 54:1844, 1996.

[117] N. Gisin. *Phys. Lett. A*, 242:1, 1998.

[118] A. Lamas-Linares, C. Simon, J. C. Howell, and Dik Bouwmeester. *Science*, 296:712, 2002.

[119] H. Bechmann-Pasquinucci and N. Gisin. *Phys. Rev. A*, 59:4238, 1999.

[120] F. Grosshans and P. Grangier. *Phys. Rev. A*, 64:010301(R), 2001.

[121] F. Grosshans and P. Grangier. *Phys. Rev. Lett.*, 88(5):057902, 2002.

[122] F. Grosshans and P. Grangier. *quant-ph/0204127*, 2002.

[123] N. J. Cerf, A. Ipe, and X. Rottenberg. *Phys. Rev. Lett.*, 85:1754, 2000.

[124] N. Treps, U. Andersen, B. Buchler, P. K. Lam, A. Maître, H.-A. Bachor, and C. Fabre. *Phys. Rev. Lett.*, 88(20):203601, 2002.

[125] G. Viovannetti, S. Lloyd, and L. Maccone. *Nature*, 412:417, 2001.

[126] S. L. Braunstein and H. J. Kimble. *Phys. Rev. Lett.*, 80(4):869, 1998.

[127] J. Lee, M. S. Kim, and H. Jeong. *Phys. Rev. A*, 62:032305, 2000.

[128] G. Santarelli, Ph. Laurent, P. Lemonde, A. Clairon, A. G. Mann, S. Chang, A. N. Luiten, and C. Salomon. *Phys. Rev. Lett.*, 82(23):4619, 1999.

[129] V. Meyer, M. A. Rowe, D. Kielpinski, C. A. Sackett, W. M. Itano, C. Monroe, and D. J. Wineland. *Phys. Rev. Lett.*, 86(26):5870, 2001.

[130] J. J. Bollinger, W. M. Itano, D. J. Wineland, and D. J. Heinzen. *Phys. Rev. A*, 54:R4649, 1996.

[131] S. A. Diddams, Th. Udem, J. C. Bergquist, E. A. Curtis, R. E. Drullinger, L. Hollberg, W. M. Itano, W. D. Lee, C. W. Oates, K. R. Vogel, and D. J. Wineland. *Science*, 293:825, 2001.

[132] A. M. Almeida, E. Nogueira, and M. Belsley. *Am. J. Phys.*, 67(5):428, May 1999.

[133] G. D. Boyd and D. A. Kleinman. *J. Appl. Phys.*, 39(39):3597, 1968.